



**Politecnico
di Torino**

Politecnico di Torino

Masters degree in automotive engineering

Academic year. 2024/2025

03/2025



Development of simplified vehicle models for impact barrier

Tutor:

Prof. Eng. Alessandro Scattina

Candidati:

Bruno Gente Magnani

Abstract

This work is the continuation of the European Joint Research Centre project of developing structural FEM simplified vehicle models, to assess in a fast and economic way the impact of such vehicles with various barriers. The project is meant to ensure protection of public spaces against hostile vehicle attacks. The Politecnico di Torino's role is to use a FEM explicit solver, LS-Dyna, to benchmark a software, Euro plexus, developed in collaboration with JRC, and to propose and study new simulation scenarios and improvements of the simplified vehicle models. The model studied in this thesis is the generic N1 vehicle that collides with a rigid bollard. Different sensitivity analysis have been performed to understand what the effect of many individual parameters is, such as the vehicle initial speed or the type of frame connections.

Index

Abstract	5
Index.....	6
Introduction	14
Chapter 1: LS-Dyna – Europlexus benchmarking: New Q4 γ formulation	16
Bollard – Coarse mesh	19
Cross member – Coarse mesh	20
Frame – coarse mesh	21
Vehicle – coarse mesh.....	22
Bollard – fine mesh	23
Cross member – fine mesh	23
Frame – fine mesh	24
Vehicle – fine mesh.....	25
Conclusions	26
Chapter 2: Speed sensitivity analysis.	29
Initial velocity: 60 km/h	30
Initial velocity: 70 km/h	32
Initial velocity: 80 km/h	35
Results comparison	37
Simplified model.....	41
Conclusions	43
Chapter 3: Cross member connection.	44
Spotweld connection model	46

Spotweld resistance sensitivity analysis.....	47
Spotwelds forces	52
Spot weld models validation	56
Mesh adjustment	59
Remeshed model rigid.....	60
Spotweld resistance sensitivity analysis – remeshed model.....	64
Spotwelds forces - remeshed.....	71
Spot weld models validation	76
Shear force effect.	79
Spotwelds forces – Shear force limit.....	83
Spot weld models validation	84
Conclusions	87
Chapter 4: Impulse conservation analysis.....	89
N1 model.....	90
N2 model.....	94
Conclusions	97
Acknowledgements	101
Bibliography.....	103

List of Figures

Figure 1: Shell element formulation test model.	16
Figure 2: Coarse mesh bollard and cross member on the left, fine mesh bollard and cross member on the right.	18
Figure 3: Section on the model in the XZ middle plane. The nodal rigid constraint is displayed in bright red.....	18
Figure 4: Frame constraints effect.....	19
Figure 5: Bollard internal and kinetic energy, coarse mesh.	20
Figure 6: Cross member internal energy, coarse mesh.....	20
Figure 7: Cross member kinetic energy and x momentum, coarse mesh.	21
Figure 8: Cross member internal energy, coarse mesh.....	21
Figure 9: Cross member internal energy, coarse mesh.....	22
Figure 10: Vehicle kinetic energy, internal energy and x momentum, coarse mesh.....	23
Figure 11: Bollard internal and kinetic energy, fine mesh.	23
Figure 12: Cross member internal energy fine mesh.	24
Figure 13: Cross member kinetic energy and x momentum, fine mesh.	24
Figure 14: Frame internal energy, kinetic energy and x momentum, fine mesh.	25
Figure 15: Vehicle internal energy, external energy and x momentum, fine mesh.....	26
Figure 16: Bollard internal energy results comparison.	26
Figure 17: Bollard kinetic energy results comparison.....	27
Figure 18: Cross member results comparison.	27
Figure 19: JRC generic N1 vehicle model.	29
Figure 20: N1 generic vehicle model engine bay.....	30
Figure 21: Force exchange, 60 km/h initial velocity.....	31
Figure 22: Impact phases, 60 km/h.	32
Figure 23: Force exchange, 70 km/h initial velocity.....	33
Figure 24: Impact phase 1, 70 km/h.....	33
Figure 25: Impact phase 2, 70 km/h.....	34
Figure 26: Impact phase 3, 70 km/h.....	34
Figure 27: Impact side section view.....	35
Figure 28: Force exchange, 80 km/h initial velocity.....	36

Figure 29: Impact phases 1 and 2, 80 km/h.....	36
Figure 30: Impact phases 3 and 4, 80 km/h.....	36
Figure 31: Impact phase 5, 80 km/h.....	37
Figure 32: Speed sensitivity analysis x force comparison.....	37
Figure 33: Rear wheel vertical displacement.	38
Figure 34: Kinetic energy comparison at different initial speeds.....	38
Figure 35: Internal energy comparison at different initial speeds.....	39
Figure 36: Bollard - engine interpenetration.	40
Figure 37: Engine surface eroded elements.	40
Figure 38: Simplified impact model.....	41
Figure 39: Contact type influence on penetration.	42
Figure 40: Contact energy comparison at different initial speeds.....	43
Figure 41: Cross member connection with the frame.	45
Figure 42: N2A / N3D front cross member spot welds.....	46
Figure 43: Cross member connection change. Reference model on the left, spot weld model on the right	47
Figure 44: X -force, spotweld resistance sensitivity analysis.....	48
Figure 45: Spotweld resistance sensitivity analysis, 70 ms simulation time.....	49
Figure 46: Spotweld resistance sensitivity analysis, 100 ms simulation time.....	49
Figure 47: Spotweld resistance sensitivity analysis, 140 ms simulation time.....	50
Figure 48: Spotweld resistance sensitivity analysis, cross beam deformation comparison.	51
Figure 49: Cross member twisting in spotweld models.	51
Figure 50: Studied spot welds detail.	52
Figure 51: SWID 20 force exchange.....	53
Figure 52: SWID 17 force exchange.....	54
Figure 53: SWID 14 force exchange.....	54
Figure 54: Model 3 SWID sweep.....	55
Figure 55: Model 4 SWID sweep.....	55
Figure 56: Model 5 and 6 SWID sweep.....	56
Figure 57: Validation reference points.....	56
Figure 58: Bollard penetration.	57
Figure 59: Flatbed deceleration.....	58

Figure 60: Cabin deceleration.	58
Figure 61: front wheel deceleration.....	58
Figure 62: Rear flatbed z displacement.....	59
Figure 63: Flatbed pitch motion.	59
Figure 64: Mesh adjusted model.	60
Figure 65: X -force, remeshed rigid model.	61
Figure 66: Engine travel, remeshed rigid model, 130 ms.	61
Figure 67: Kinetic and internal energy, remeshed rigid model glstat.	62
Figure 68: Kinetic and internal energy, remeshed rigid model matsum.	62
Figure 69: eroded hourglass and kinetic energy, model 1 remesh.	63
Figure 70: Global kinetic energy, shell formulation effect.	64
Figure 71: X-force, spotweld resistance sensitivity analysis, remeshed model.	65
Figure 72: Spotweld resistance sensitivity analysis, 70 ms simulation time, remeshed model.	66
Figure 73: Spotweld resistance sensitivity analysis, 100 ms simulation time, remeshed model.	67
Figure 74: Spotweld resistance sensitivity analysis, 140 ms simulation time, remeshed model.	68
Figure 75: Spotweld resistance sensitivity analysis, cross beam deformation comparison, remeshed model.....	69
Figure 76: Cross member twisting in spotweld models, remeshed model.....	70
Figure 77: longitudinal beam bending comparison.....	70
Figure 78: Studied spot welds detail, remeshed model.....	71
Figure 79: Leading node force exchange, remeshed models 3 and 4.....	72
Figure 80: Leading node force exchange, remeshed model 5.....	72
Figure 81: Leading node force exchange, remeshed model 6.....	73
Figure 82: Half section node force exchange, remeshed models 3 and 4.	73
Figure 83: Half section node force exchange, remeshed model 5.....	74
Figure 84: Half section node force exchange, remeshed model 6.....	74
Figure 85: Trailing node force exchange, remeshed models 3 and 4.....	75
Figure 86: Trailing node force exchange, remeshed model 5.	75
Figure 87: Half section node force exchange, remeshed model 6.....	75
Figure 88: Bollard penetration, remeshed models.....	76
Figure 89: Flatbed deceleration, remeshed models.....	77
Figure 90: Cabin deceleration, remeshed models.....	77

Figure 91: front wheel deceleration, remeshed models.....	78
Figure 92: Flatbed z displacement, remeshed models.....	78
Figure 93: flatbed pitch, remeshed models.	79
Figure 94: X -force, remeshed model, shear force sensitivity analysis.....	80
Figure 95: Spotweld shear resistance sensitivity analysis, 70 ms simulation time, remeshed model ...	81
Figure 96: Spotweld shear resistance sensitivity analysis, 100 ms simulation time, remeshed model .	81
Figure 97: Spotweld shear resistance sensitivity analysis, 140 ms simulation time, remeshed model .	82
Figure 98: Cross member deformation, shear force limit contribution.	82
Figure 99: Leading node force exchange, remeshed models 7 and 8.....	83
Figure 100: half section force exchange, remeshed models 7 and 8.	83
Figure 101: Trailing node force exchange, remeshed models 7 and 8.....	84
Figure 102: Bollard penetration, shear effect.	84
Figure 103: Flatbed deceleration, shear effect.	85
Figure 104: Cabin deceleration, shear effect.....	85
Figure 105: front wheel deceleration, shear effect.	86
Figure 106 Flatbed z displacement, remeshed models.....	86
Figure 107: flatbed pitch, remeshed models.	87
Figure 108: Front flatbed vertical motion.	87
Figure 109: N1 vehicle models, different impact locations.	90
Figure 110: Force history, filtered and unfiltered curves.....	90
Figure 111: Integrated difference, centred bollard and beam centred bollard.....	91
Figure 112: Decentred bollard N1 impact, X force and momentum.	92
Figure 113: Moment transmitted from the ground to stop the vehicle movement.	92
Figure 114: N1 vehicle beam cantered bollard, interaction with the ground.	93
Figure 115: N2 generic vehicle model, centred bollard	94
Figure 116: N2 model x force exchange with the bollard.....	94
Figure 117: Force exchange in the Surface to surface and nodes to surface cards.	95
Figure 118: Beam element in contact with the bollard.....	95
Figure 119: N2 model impulse and momentum results.	96

List of tables

Table 1: LS-Dyna simulation summary	17
Table 2: Observed parameters.....	17
Table 3: Internal energy at the end of simulation.....	28
Table 4: Cross member connection simulation summary	47
Table 5: Cross member connection simulation summary, remeshed model	64
Table 6: Cross member connection simulation summary, shear and strain effect	79

Introduction

The goal of this thesis, made in collaboration with the European Research Centre JRC, is to study and improve the JRC N1 and N2 generic vehicle FEM models [1], made and tested by SVS FEM services

The final objective of this project is to share models that are used to test barriers to improve the safety of public spaces.

These models represent the essential details of common commercial vehicles such as frame, powertrain, body shells suspension systems, which are set to collide with an initial velocity against some kind of barrier. In this thesis, the barrier is always considered as a rigid cylindrical bollard.

The strategy to improve the models is to prepare and launch distinct batches of simulations, to understand the effect of specific parameters. The simulation results are critically analysed, and the performance of the model is evaluated, addressing potential issues and proposing strategies to solve them. Sensitivity analyses are useful to develop a FEM model capable of simulating realistic outcomes in a wide array of situations.

It is also important to quantify in scientific terms improvements in the models and quality of the results. To have a quantitative sense of these attributes, benchmarking between FEM solvers is performed. In this paper a benchmarking study between formulations of four-nodes shell elements in LS-Dyna and Europlexus (in short EPX) is reported

Lastly, an investigation has been done about the observation of an incongruency

The software used to manage the models is LS Prepost, which is the free LS-Dyna pre and post processor.

Computational resources were provided by HPC@POLITO, a project of Academic Computing within the Department of Control and Computer Engineering at the Politecnico di Torino (<http://www.hpc.polito.it>)

To keep consistent results with previous works, the solver used to carry the simulations was LS-Dyna R12 SMP version (double precision)

This thesis is structured as follows:

The first chapter is dedicated to the test of a new 4 nodes shell element formulation meant to improve performance under extreme deformations scenarios. This element formulation is benchmarked with two element formulations used in LS-Dyna.

The second chapter is a sensitivity analysis on the initial speed of the vehicle.

The third chapter is a sensitivity analysis on the resistance of the cross member – longitudinal beams connections. Since the current constraint does not have any failure criteria, an alternative strategy has been proposed and tested.

The fourth chapter summarizes the investigation on an observed inconsistency between the momentum curve calculated by LS-Dyna and the same curve obtained as the force history integral

Chapter 1: LS-Dyna – Europlexus benchmarking: New Q4 γ formulation

New research on FEM theory keeps improving the effectiveness of the method in calculating increasingly realistic outcomes of the numerical simulations. Recently the formulation used to describe 4 nodes shell elements in Europlexus named MITC or Q4 γ has been modified to improve the response under mixed membrane-bending load and high deformation. This chapter's goal is to compare the new Q4 γ formulation with its precedent iteration and the most common formulations used in a general – purpose Multiphysics simulation software such as LS-Dyna.

To compare the Europlexus (in short EPX) and LS-Dyna results, a simple numerical model has been set up as follows:

- The model is made up of the two longitudinal beams and the front cross member of a ladder frame, illustrated in Figure 1.
- It moves with a given initial velocity of 20 m/s towards a fixed bollard.
- Frame and bollard are made of the same steel material model.
- The simulation is carried four times changing the mesh density and the shell formulation of the cross member and bollard as listed in LS-Dyna simulation summary in Table 1.

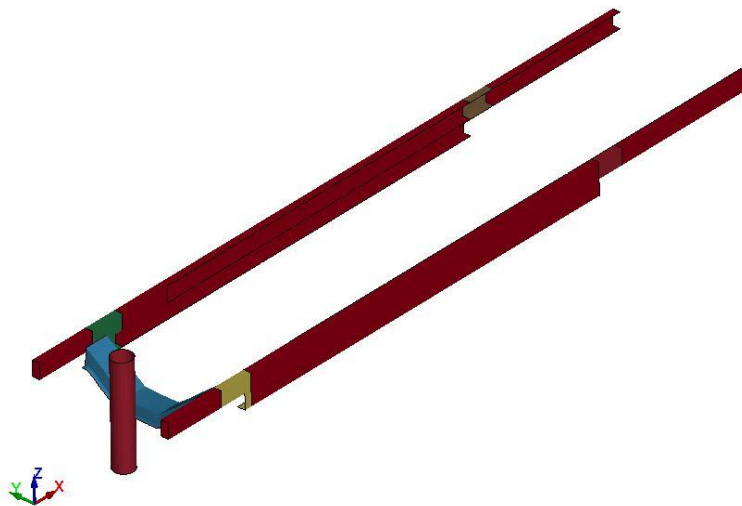


Figure 1: Shell element formulation test model.

In the following study the longitudinal beams are referred to as “frame”, the sum of the frame and the cross member is named “vehicle” and in the figures the EPX shell formulation is referred to as in the Europlexus user manual “Q4G” [2].

Simulation number	Shell formulation	Max element length
1	EL2	40 mm
2	EL16	40 mm
3	EL2	20 mm
4	EL16	20 mm

Table 1: LS-Dyna simulation summary

The same tests have been carried in EPX comparing the older and the latest 4-element shell formulations. The available data from these simulations are listed in Table 2:

\	Kinetic energy	Internal energy	X-Momentum
Bollard	✓	✓	✗
Cross member	✓	✓	✓
Longitudinal beams	✓	✓	✓
Vehicle	✓	✓	✓

Table 2: Observed parameters.

The choice of different mesh sizes allows to understand the efficacy of the formulations: according to FEM theory, the higher number of elements a model is made of, the more it will behave similarly to a real part and the more realistic the results will be (as long as the element assumptions hold. For example, shell elements thickness must always be less than the other dimensions). However, an increase of simulated elements causes an exponential increase in computational time and a trade-off must be found between computational time and reliability of the results. High quality formulations can generate the same results as worse quality formulations with fewer elements. Thus, improving the time-quality trade-off. The difference in mesh size can be observed in Figure 2.

The EL2 shell formulation is the Belytschko-Lin-Tsay Shell and in LS-Dyna is the default shell section for explicit simulations because of the computational efficiency [3]. EL16 shell formulation is a fully

integrated shell. It is more computationally expensive than EL2 [4] but is more robust and effectively deals with extensive shell deformation.

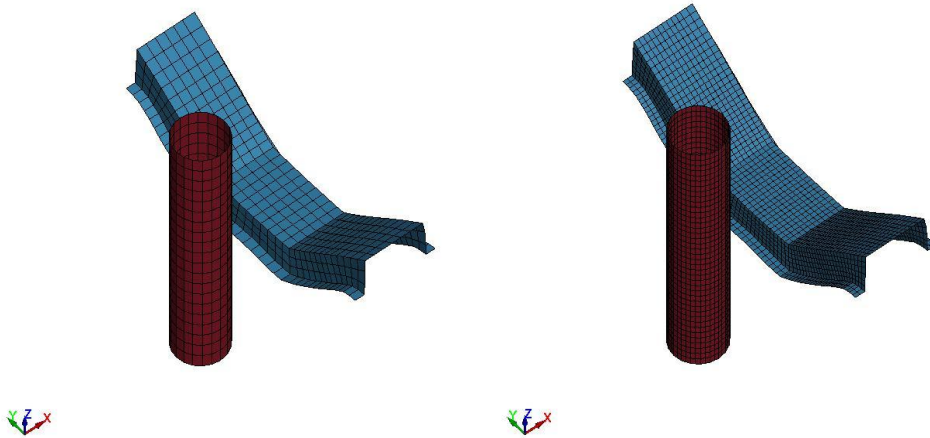


Figure 2: Coarse mesh bollard and cross member on the left, fine mesh bollard and cross member on the right.

The connection of longitudinal beams and cross element is a rigid link between given sets of nodes. Namely the edges of the cross member and the edges of the green and yellow portions of the longitudinal beam, as depicted in Figure 3. Although this configuration is not representative of a real ladder frame, it allows to concentrate the plastic deformation energy only into the cross member and the bollard. In this way the different formulation behaviour is highlighted.



Figure 3: Section on the model in the XZ middle plane. The nodal rigid constraint is displayed in bright red.

Frame constraints in the rear of the longitudinal beams cause concentration of forces in the cross member unloading the beams (Figure 4, left picture). If instead the rear is not constrained (Figure 4, right picture), the energy absorbed by the frame bending is relieved from the cross member. Given the objective of studying the performance under high deformation of the cross member, the former model is more suited for the task.

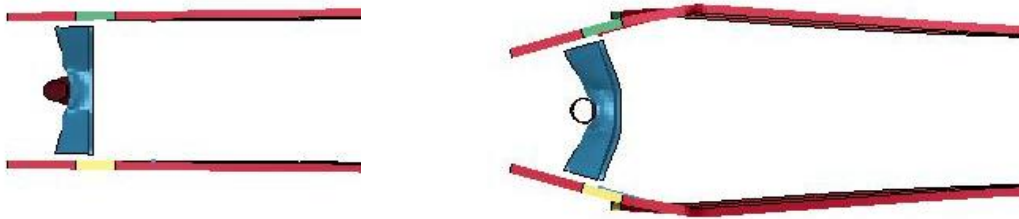


Figure 4: Frame constraints effect.

Now that the model has been illustrated, it is possible to analyse simulation results: the results for each part are observed for the coarse mesh models. The same is done for the fine mesh ones and, in conclusion, the convergence of the results is shown by comparing the main differences between the two data sets.

Bollard – Coarse mesh

In Figure 5 it is immediately apparent that the different formulations generate different solutions: LS-Dyna formulations attribute more energy transfer to the bollard than Europlexus formulations and the new Q4 γ formulation simulates the lowest energies both internal and kinetic. EL2 calculates a higher plastic deformation, while EL16 generates slightly higher kinetic energy peak. EL16 and the previous Q4 γ calculate similar results.

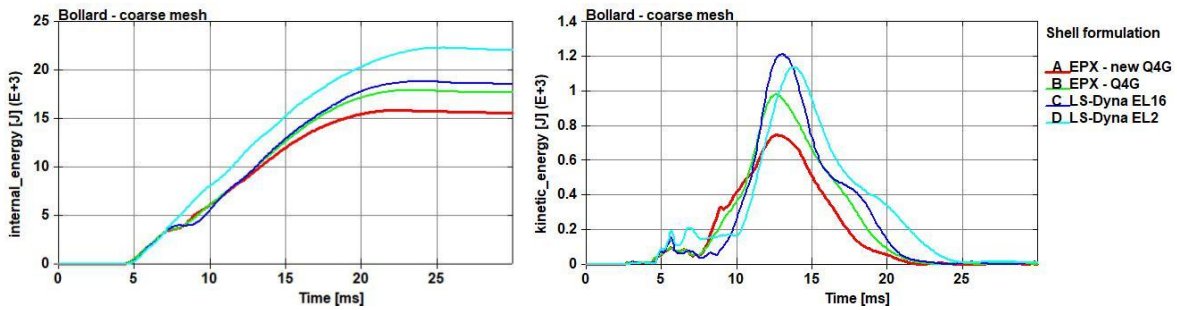


Figure 5: Bollard internal and kinetic energy, coarse mesh.

Cross member – Coarse mesh

Since the energy required to stop an object with a given mass is fixed, the internal energy profile of the cross member is the opposite of the bollard as shown in Figure 6: LS-Dyna attributes lower deformation on the cross element, with the lowest being EL2. In this case, however, it is possible to notice that the LS-Dyna algorithm deletes from the simulation the energy of elements that incur failure and this cause discontinuities in the curve. It is possible to add this contribution that LS-Dyna stores with the name “eroded energy”.

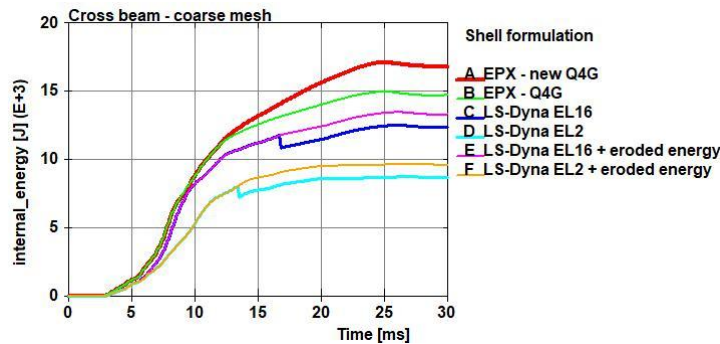


Figure 6: Cross member internal energy, coarse mesh.

For what kinetic energy and momentum are concerned (Figure 7), the results are almost identical in all formulations. The kinetic energy oscillations are slightly different between LS-Dyna and Europlexus.

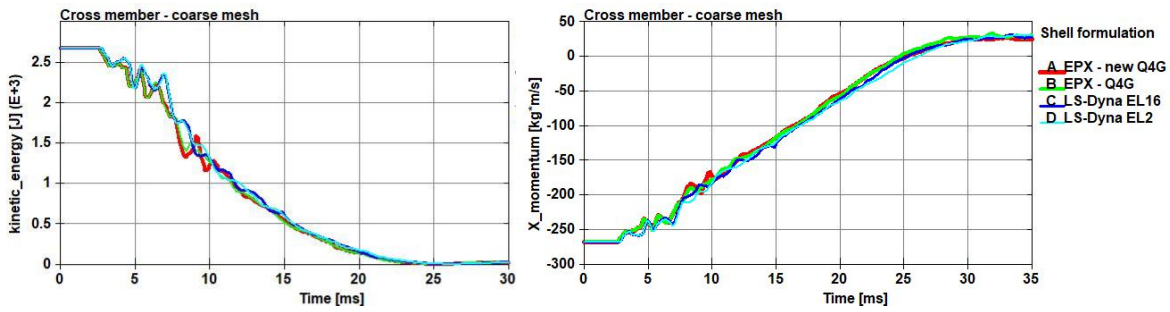


Figure 7: Cross member kinetic energy and x momentum, coarse mesh.

Frame – coarse mesh

As shown in Figure 8, the frame stores little energy since most of its length is shared with a rigid nodal body and the stress is distributed evenly along the beams. The vibration similarities between the LS-Dyna and Europlexus model of the frame can be considered proof that the boundary conditions and frame connections are the same, and the simulation setup in LS-Dyna is correct. These indicators are useful because the two programs, although similar, are not entirely compatible. For example, the contact algorithms and the link between the parts had to be re-created in the LS-Dyna environment.

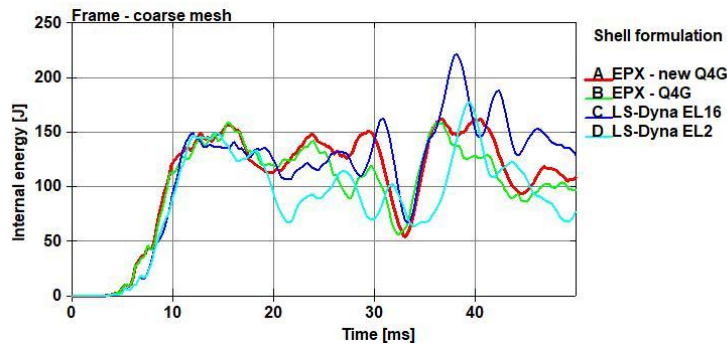


Figure 8: Cross member internal energy, coarse mesh.

As for the cross member case, the frame kinetic energy and x momentum (Figure 9) are almost superimposed in all the shell formulation. The differences in element formulations do not have enough effect on the impact dynamic to change noticeably the movement of the parts. This is true mostly because the cross member does not fail completely, but higher energy impact could show radically different

impact dynamics. However, in this experiment the results of x momentum and kinetic energy yield very similar results in all models.

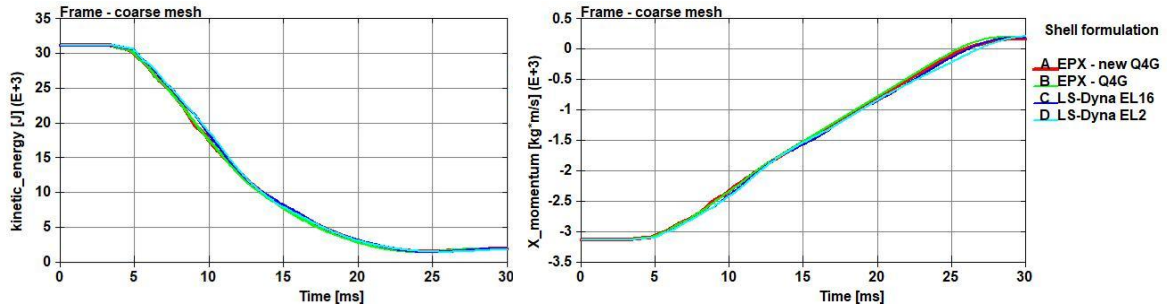


Figure 9: Cross member internal energy, coarse mesh.

Vehicle – coarse mesh

Vehicle data shown in Figure 10 are the sum of the cross member and longitudinal beams curves. The internal energy absorbed by the cross member is much higher than the energy stored in the frame and thus its effect is negligible. Vice versa, the kinetic energy is mainly attributed to the frame, being bigger and heavier, and the cross-member energy slightly offsets the curve of the frame alone.

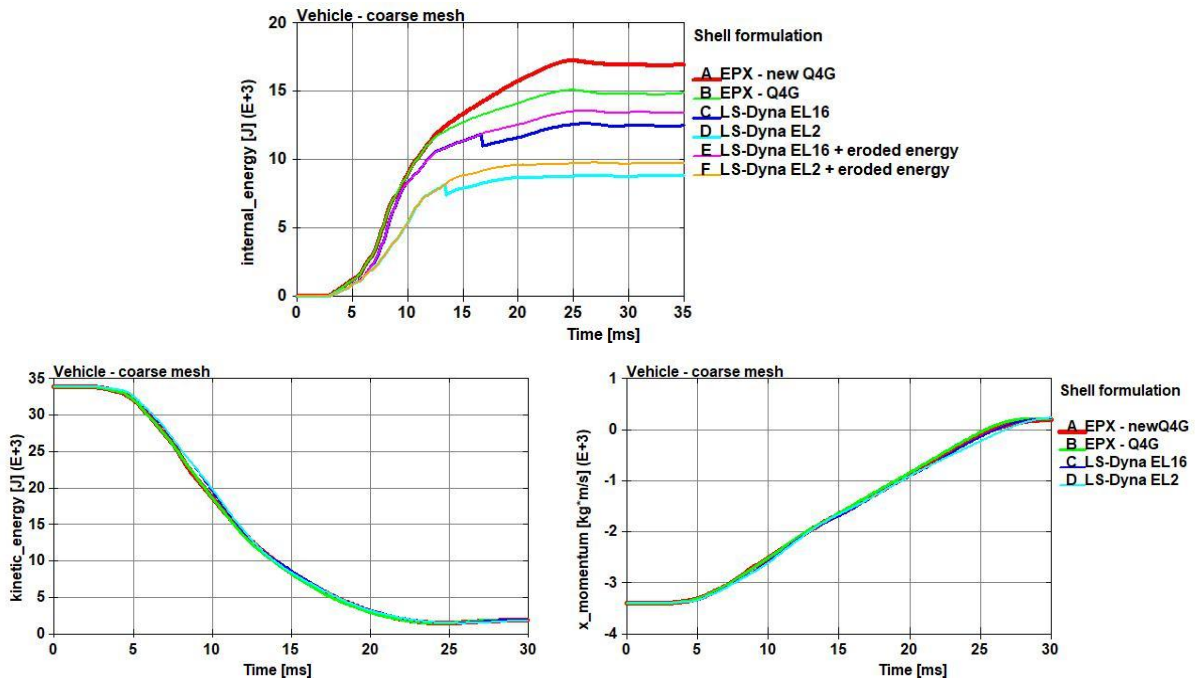


Figure 10: Vehicle kinetic energy, internal energy and x momentum, coarse mesh.

Bollard – fine mesh

As shown in Figure 11, the finer mesh simulations of EL16, Q4 γ and the new Q4 γ formulations. LS-Dyna continues to assign more internal energy to the bollard, especially EL2 that is an outlier in the energy curves. The kinetic energy main peak calculated by EL2 is lower than the other shell formulations, while the first small peak is still higher as in the coarse mesh case. All curves are grouped tighter together overall, which is a good sign of results convergence.

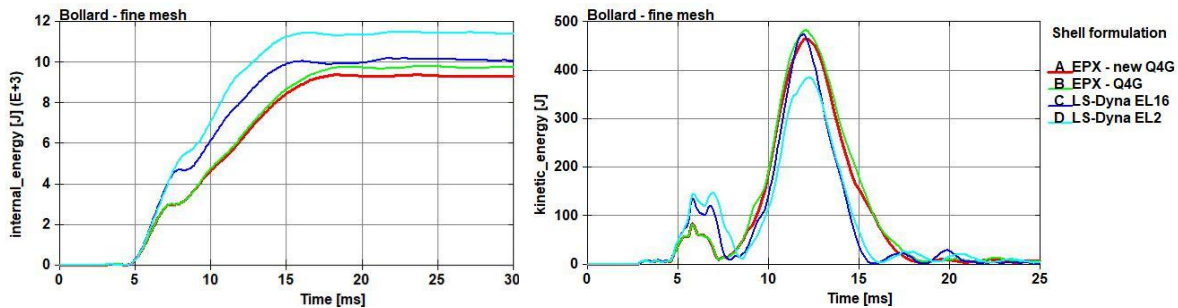


Figure 11: Bollard internal and kinetic energy, fine mesh.

Cross member – fine mesh

The finer mesh simulations display an overall increase of the energy absorbed by the cross member in Figure 12. Europlexus formulations are extremely consistent with each other, while LS-Dyna formulations continue to attribute less energy to the transverse beam. More elements fail in this simulation as it is expected.

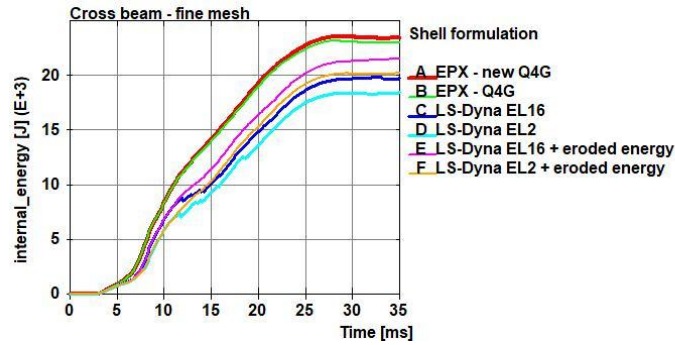


Figure 12: Cross member internal energy fine mesh.

Similarly to the coarse mesh case, the curves in Figure 13, are mostly consistent, with slight difference in the curve between solvers. It is possible to notice that the new Q4 γ formulation shows a residual oscillation of the cross member in the x momentum curve.

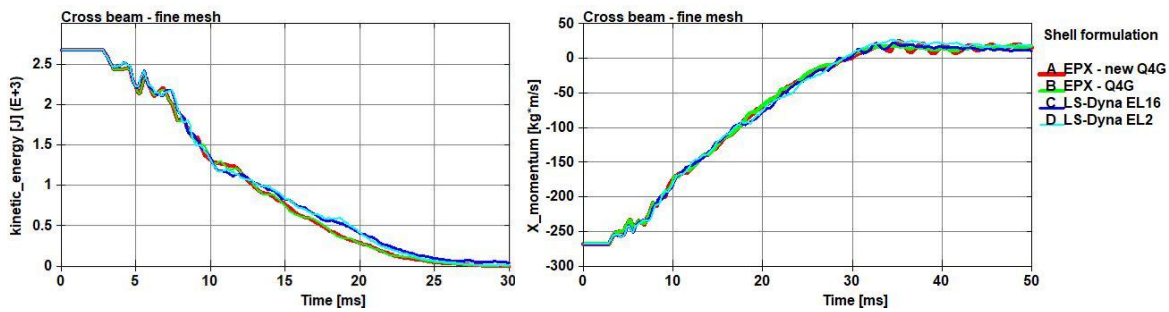


Figure 13: Cross member kinetic energy and x momentum, fine mesh.

Frame – fine mesh.

Referring to Figure 14: similarly to the coarse mesh case, the longitudinal beams vibration stores relatively little internal energy, but with the finer mesh the results are more coherent between each other. EL2 is the less precise formulation but generate comparable results with the rest of the curves. Kinetic energy and momentum follow the behaviour previously discussed.

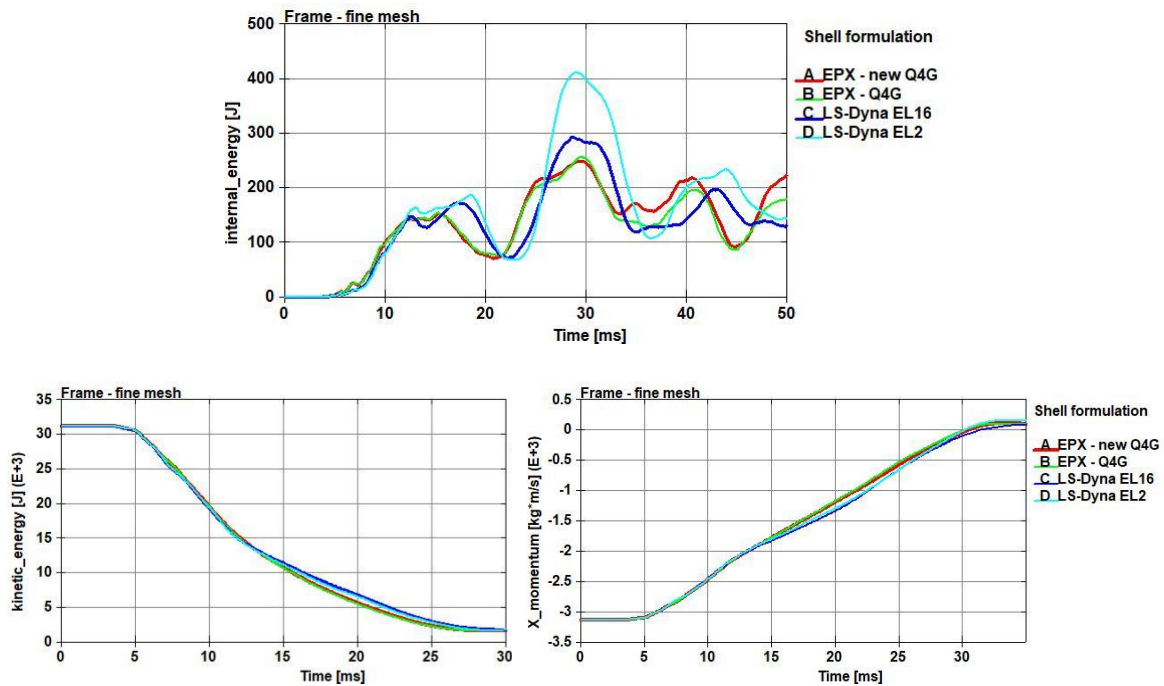
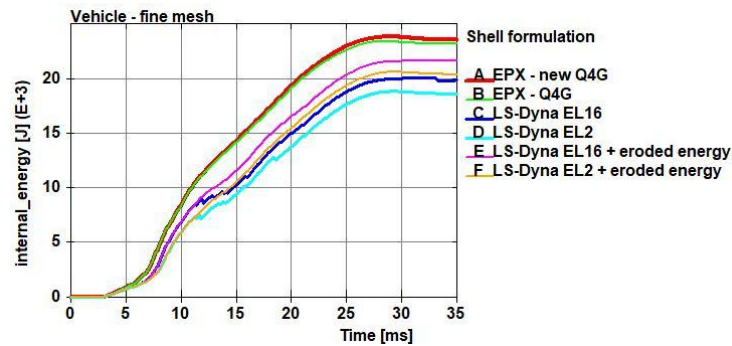


Figure 14: Frame internal energy, kinetic energy and x momentum, fine mesh.

Vehicle – fine mesh

At vehicle level, there is very high correlation between formulations in both kinetic energy and x momentum curves, as depicted in Figure 15.

The similarity in the results of the kinetic energy and momentum curves show that all shell formulations are effective in describing the impact phenomenon. However, by directly comparing the differences between the coarse and fine meshed models results of the cross member and the bollard, the differences in performance can be critically evaluated.



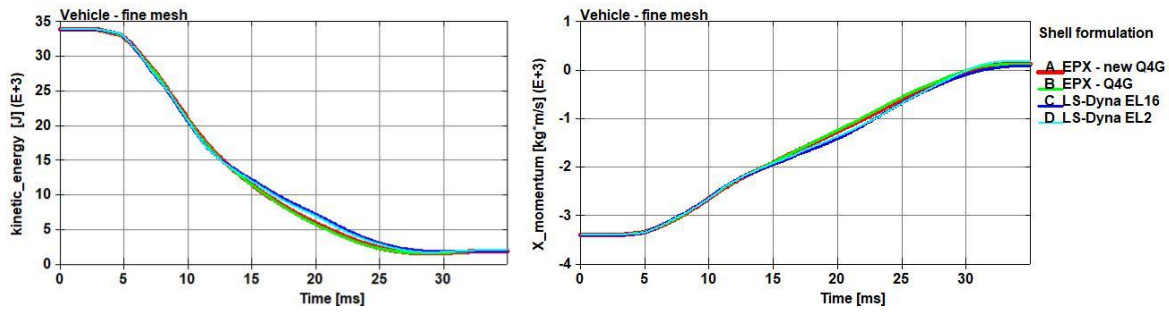


Figure 15: Vehicle internal energy, external energy and x momentum, fine mesh.

Conclusions

To scientifically compare the shell formulations, it is necessary to use objective data, and looking at the internal energy curves it is possible to use the final value of the energy absorbed as metric to draw some conclusions. With reference to the bollard internal energy in Figure 16, It is possible to see that increasing the number of elements, all curves are shifted to lower values and the final energy absorbed is closer among all the formulations. The tighter grouping Confirms that the simulations, increasing the element number, tend to converge to some value. Moreover, the fact that they converge to a lower value then the initial one suggests that the lowest among the curves is the closer to the convergence value and hence the more robust result.

However, it is important to specify that this element has been realized specifically to be used in situations where extensive deformation is expected.

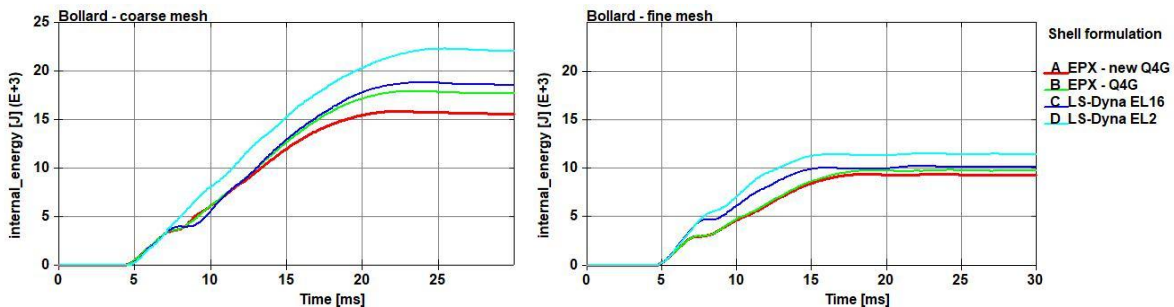


Figure 16: Bollard internal energy results comparison.

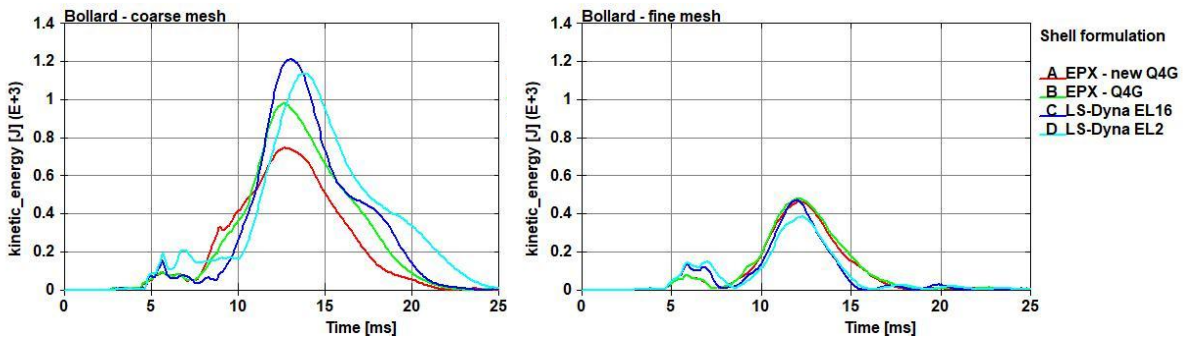


Figure 17: Bollard kinetic energy results comparison.

The same trend is observable in Figure 18 applied to the cross member internal energy, but in this case the energy increase with the mesh density.

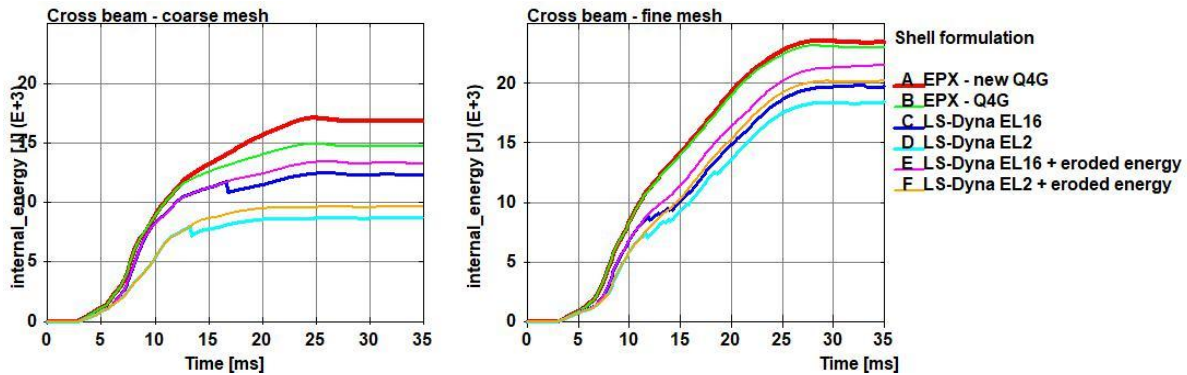


Figure 18: Cross member results comparison.

Additionally, it can be measured how much the shell formulations change the final energy value between the two mesh size simulations. In Table 3: Internal energy at the end of simulation. the final internal energy value of all shell formulations for both the bollard and the cross member are summarized. It is possible to see that the EL2 has the largest difference, while EL16 and the precedent Q4 γ formulation display similar Δ energy absorption and the new Q4 γ formulation is the most consistent. This can be interpreted as the new Q4 γ formulation to be closer to convergence or, in other words, it shows faster convergence with respect to the other formulations. This means that this formulation can provide reliable results with less computational effort. In conclusion, the new formulation has demonstrated to be very effective in this test and successfully outperformed both its previous iteration and the reference formulations in LS-Dyna.

Formulation	Bollard			Cross member		
	Coarse mesh	Fine mesh	Δ (fine - coarse)	Coarse mesh	Fine mesh	Δ (fine - coarse)
new Q4G	15,6	9,3	-6,4	16,9	23,6	6,7
Q4G	17,7	9,7	-8,0	14,7	23,2	8,5
EL16	18,6	10,0	-8,6	13,3	21,6	8,3
EL2	22,1	11,3	-10,8	9,7	20,3	10,6

All values are expressed in kJ

Table 3: Internal energy at the end of simulation.

Chapter 2: Speed sensitivity analysis.

The scope of this type of models is to study the effect of dangerous and costly vehicle crash in a fast, cheap and safe way by working in a digital environment instead of crashing physical vehicles. The N1 generic vehicle model has been validated by comparing the motion of pre-determined nodes with the corresponding nodes on a real vehicle [5]. Once the model is deemed realistic, it can be interesting to re-create the same experiment but with higher values of initial speed.

The virtual model is designed to respect some criteria [6] such as:

- Represent a specific category of vehicle (N1 in this case)
- Be brand – independent including common features of vehicles in the category and excluding brand – specific features.
- Be simple and computationally efficient.
- Having adjustable parameters.

Among the adjustable parameters it is possible to set the initial speed of the vehicle. The following analysis is carried out simulating the frontal impact with a bollard with different initial velocities: 48 km/h is the reference case, then 60 km/h, 70 km/h and 80 km/h.

Further details on the model structure are discussed on previous thesis works [5] [7].

Crash test - JRC N1

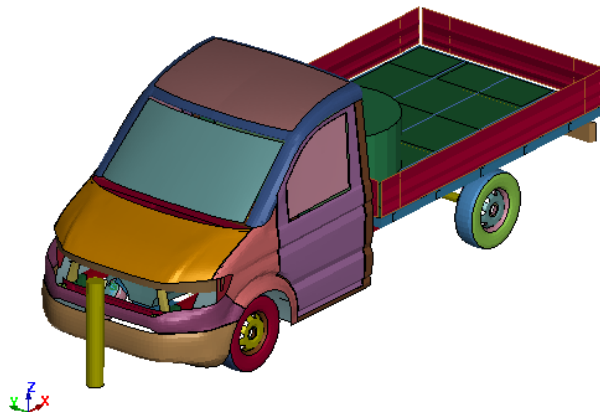


Figure 19: JRC generic N1 vehicle model.

It is useful to understand the model composition before the analysis is carried. Figure 20 illustrates the main parts involved in the impact with the bollard: The engine (1) is rigid, and the engine surface (2) is

added to absorb part of the impact and reduce the force peak generated by the contact with the bollard. The engine is fixed to the cross member (4) with four beam elements, two for each side, which simulate the engine mounts (3). The longitudinal beams (5) are linked at the front with crush zones (6) that are disposable parts of the frame to protect it from low energy impacts. The front crush zones are rigidly connected to the frame front bumper (7). The front fascia (8) and the bumper (9) are linked to the other parts through spot welds. The front partition, also known as firewall (10) separates the cabin from the engine bay. The cabin floor (11) completes the picture. It engages in the impact because the engine is pushed towards the cabin and impacts the cabin surfaces.

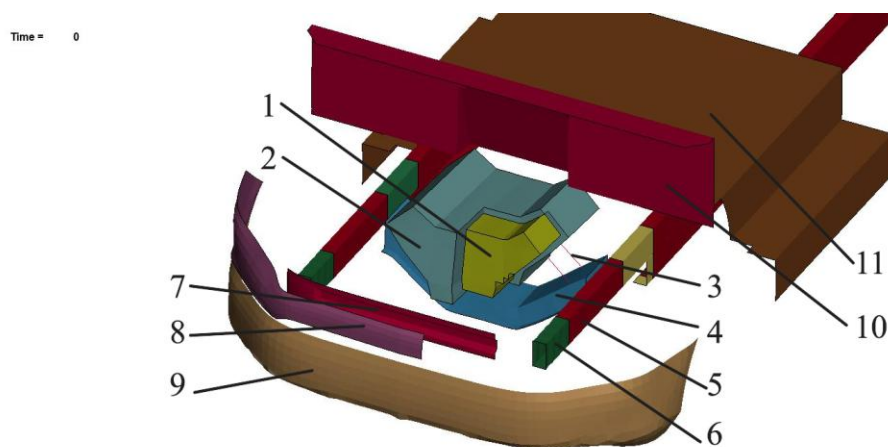


Figure 20: NI generic vehicle model engine bay.

At first the model behaviour at different initial velocities is observed in each simulation, then the force exchange with the bollard and the internal energy distribution between distinct parts is compared. In the end, the differences between the simulations are summarized.

Initial velocity: 60 km/h

Figure 21 shows the evolution of the impact from the bollard point of view, meaning that the forces (positive in the x direction) are the forces the bollard applies to the vehicle to stop it. Differently from chapter 1, the bollard material is rigid. Hence, no information about energy stored is available. The force history is available in the rforc database, which contains the contact forces of all defined contact surfaces. The main force exchange surface is clearly the vehicle – bollard interaction surface, but a non-

Chapter 2: Speed sensitivity analysis

negligible component of the force exchange comes from the tires – ground contact surface, especially in the simulations with offset bollard. This aspect, however, will be treated more in detail in Chapter 4.

The impact has three distinct phases:

- the first is the initial slight raise in the force that lasts from 10 to 35 milliseconds. In this phase the front fascia, the bumper and the front frame bumper impact the bollard, they cause little to no resistance to the vehicle movement. However, due to the rigid link between the frame front bumper and the frame crush zone, the latter is involved in the impact before the main force peak (Figure 22, top left).
- The second is the main force peak that is caused by the engine impact with the bollard from 35 to 50 ms. During this impact, the engine motion is completely stopped and the engine mounts, attached to the cross beam under engine, are deformed and torn off the engine surface. The cross member impacts the bollard and is deformed (Figure 22 top right).
- The third peak at 60 ms simulation time is due to the contact between the engine and the cabin floor. The following force variations are caused by the floor collapsing in waves. The longitudinal beams, drawn by the cross elements, are bent against each other and the front end continues to absorb some energy (Figure 22, bottom.)

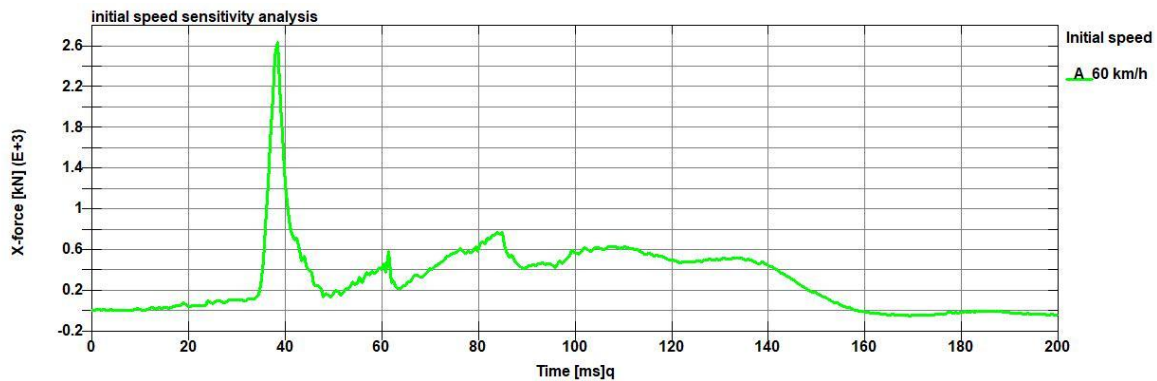


Figure 21: Force exchange, 60 km/h initial velocity.

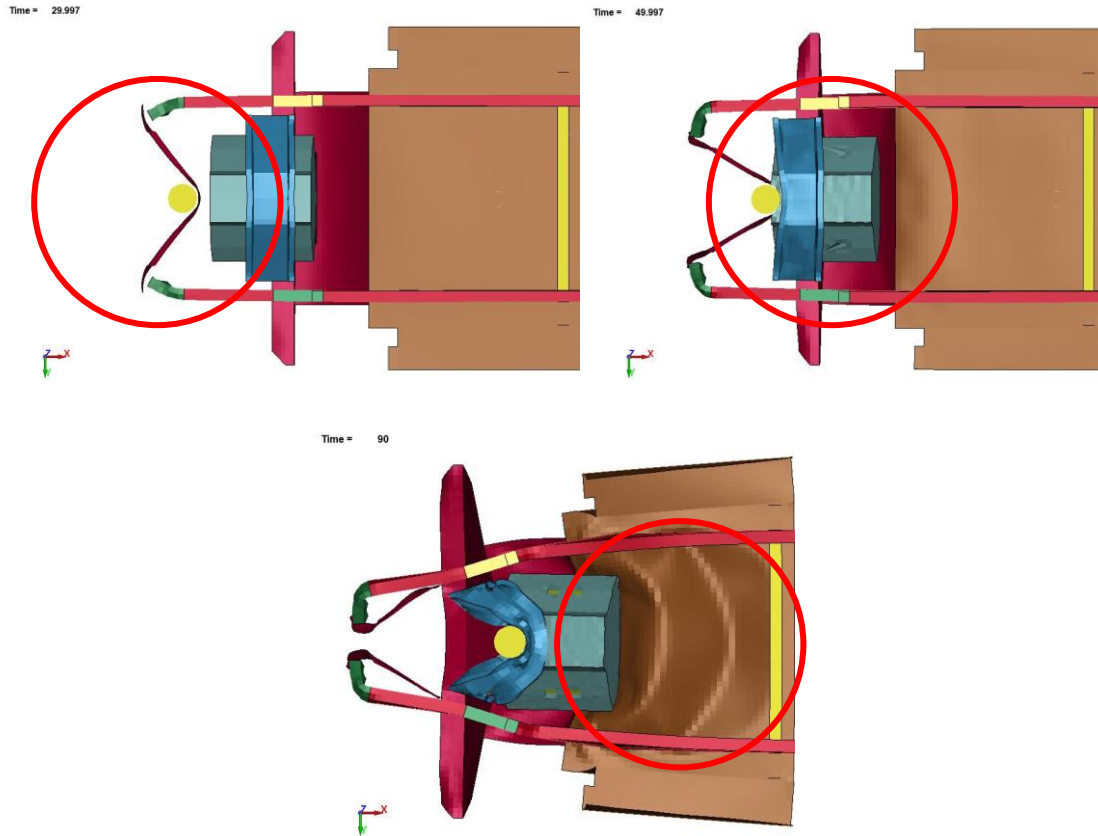


Figure 22: Impact phases, 60 km/h.

Initial velocity: 70 km/h

Figure 23 shows the x force history of the bollard with an initial vehicle velocity of 70 km/h. Although the initial kinetic energy of the moving vehicle is higher, the impact duration is similar to the previous case. The maximum force peak is slightly higher than the previous case.

- All phases are anticipated due to the higher initial velocity, the first phase starts at 10 ms and ends at 30 ms, without changes in the energy absorption. This is expected because the effect of the strain rate on the material is not yet implemented in the model, and the front parts fail absorbing always the same amount of energy regardless of the initial speed (Figure 26).
- The second phase starts at 35 ms and ends at 50 ms. The main peak is short, and the engine rebounds on the bollard and impacts the firewall and the floor of the cabin. The cross member transmits the load to the longitudinal beams that start to bend. (Figure 25).

Chapter 2: Speed sensitivity analysis

- The engine pushes against the floor in the third phase, but higher energy must be dissipated with respect to the previous case. The compressive forces on the powertrain cause the driveshaft to break. The engine slides under the cabin floor causing severe deformation (Figure 26). The kinetic energy stored in the cargo and flatbed cause the rear end of the longitudinal beams to bend upwards (Figure 27).

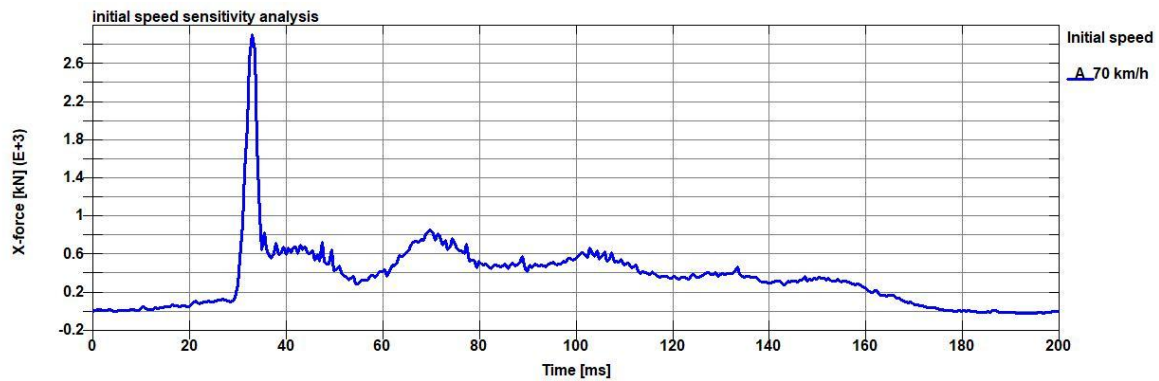


Figure 23: Force exchange, 70 km/h initial velocity.

Time = 19.999

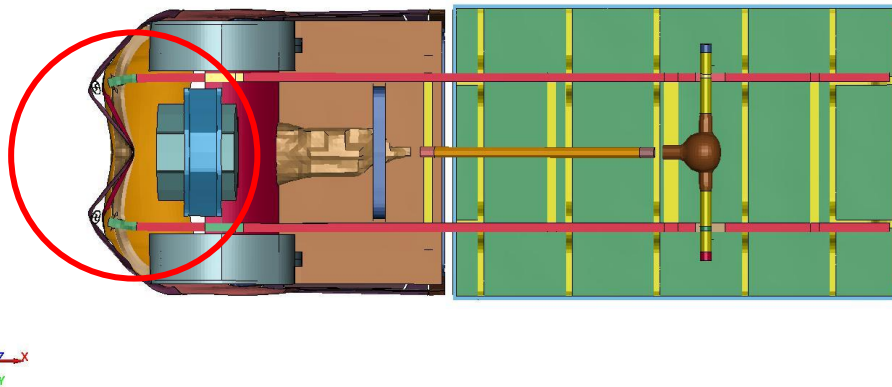


Figure 24: Impact phase 1, 70 km/h.

Time = 49.998

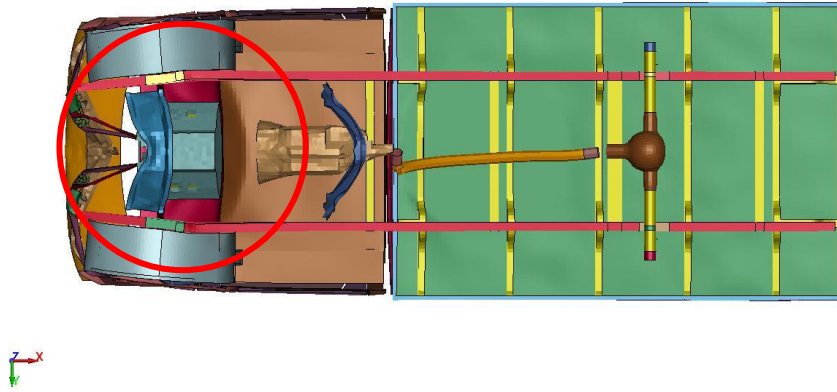


Figure 25: Impact phase 2, 70 km/h.

Time = 120

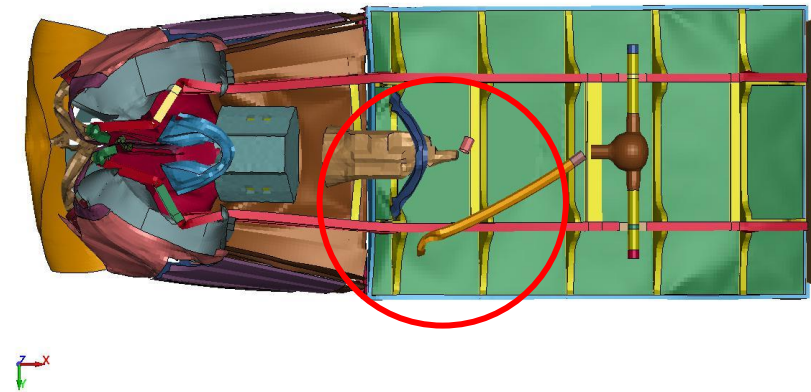


Figure 26: Impact phase 3, 70 km/h.

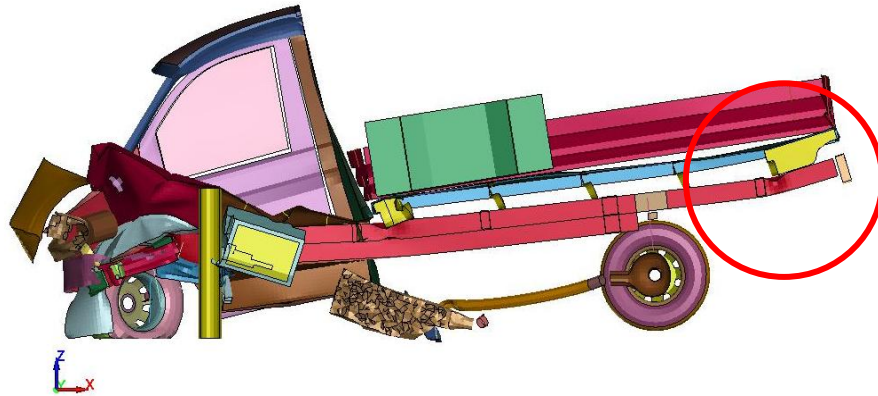


Figure 27: Impact side section view.

Initial velocity: 80 km/h

The last simulation of this section has the highest initial velocity and thus the highest kinetic energy to dissipate. The force exchange is generally higher with respect to the previous simulations as it is shown in Figure 28. The impact evolution is slightly different from the previous simulations.

- The first impact phase follows the same trend discussed before; it reaches its maximum value at 25 ms before the engine impacts the bollard (Figure 29, left).
- The second peak is noticeably higher with respect to lower initial speed models and involves the engine block alone with severe compenetrating of the engine into the bollard. Many elements of the engine surface fail, exposing the rigid engine portion. The engine mounts strain to failure their attachment points to the engine surface (Figure 29, right).
- An additional phase can be observed. At 30 ms the cross member hit the bollard, and the force starts to rise after the main peak. The frame starts deforming and the force is reduced while the engine interacts with the cabin floor (Figure 30, left).
- At 70 ms the floor strains and catches the engine, stopping its relative movement and increasing the force exchanged with the bollard. The cross, beam, cabin floor and frame continue to deform significantly during this phase. The driveshaft is detached from the gearbox (Figure 30, right).
- At 100 ms the floor is strained to the failure limit and the engine rear corners penetrate the cabin (Figure 31).

Chapter 2: Speed sensitivity analysis

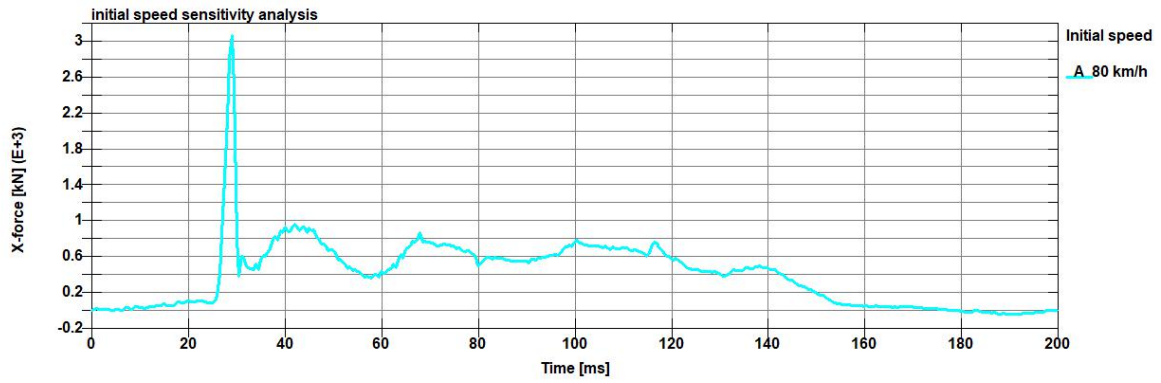


Figure 28: Force exchange, 80 km/h initial velocity.

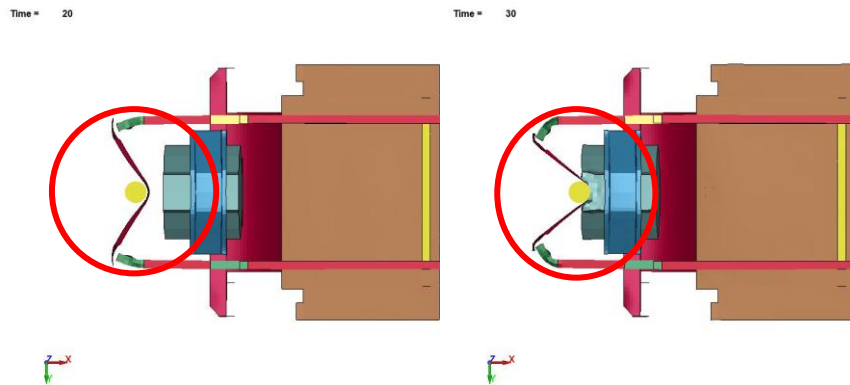


Figure 29: Impact phases 1 and 2, 80 km/h.

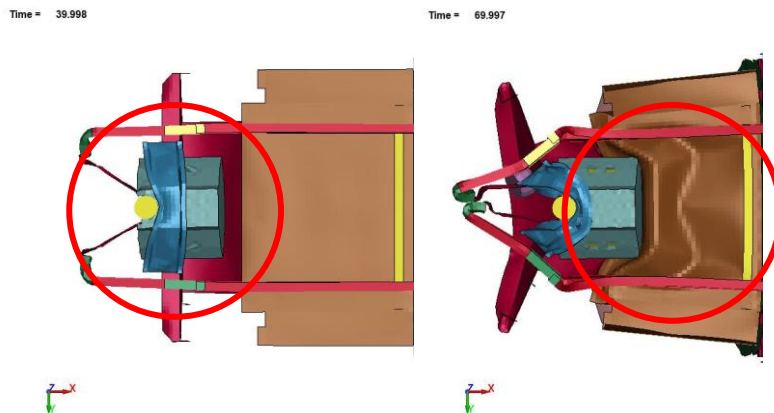


Figure 30: Impact phases 3 and 4, 80 km/h.



Figure 31: Impact phase 5, 80 km/h.

Results comparison

Figure 32 shows the previous force graphs compared with the reference simulation with an initial speed of 48 km/h. It is possible to see that the reference simulation has few distinct peaks as opposed to the increased speed ones. This is because at lower initial speed, the engine has time to rebound and impact the bollard multiple times, while in the previously discussed simulation this behaviour is much less visible. Instead, after the first engine contact with the bollard, the force history is shaped by the interaction with the cross member and cabin floor. It is interesting to notice how the impact duration is almost identical in all the simulations.

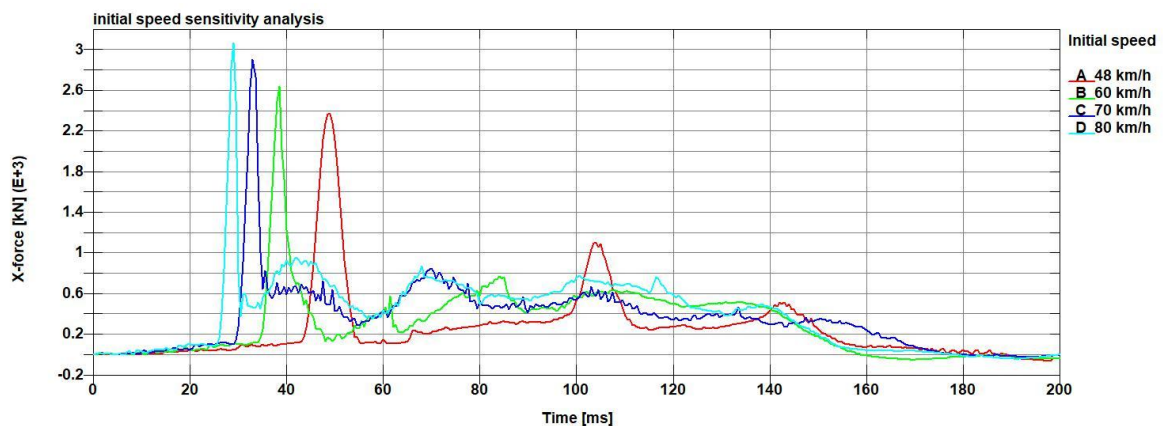


Figure 32: Speed sensitivity analysis x force comparison.

Chapter 2: Speed sensitivity analysis

The z-displacement diagram in Figure 33 refers to a node at the centre of the rear left wheel. The higher the initial velocity is, the more the vehicle pitch after the bollard impact. The increment is not linear because it depends on the deformation of many different parts.

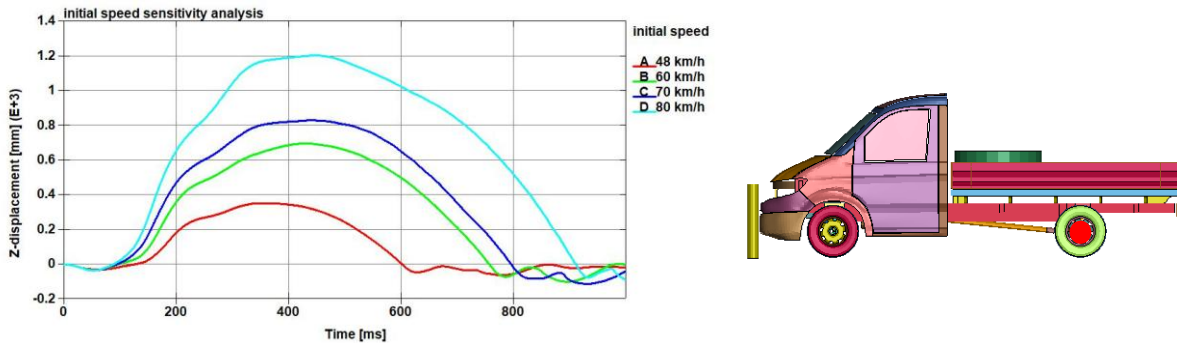


Figure 33: Rear wheel vertical displacement.

It is possible to see in Figure 34 that even after the impact with the static barrier, there is some residual kinetic energy in all the simulations. This phenomenon is accentuated in higher initial speed simulations. This is not representative of a physical phenomenon, but the residual kinetic energy is stored in deleted and severely hourglass parts.

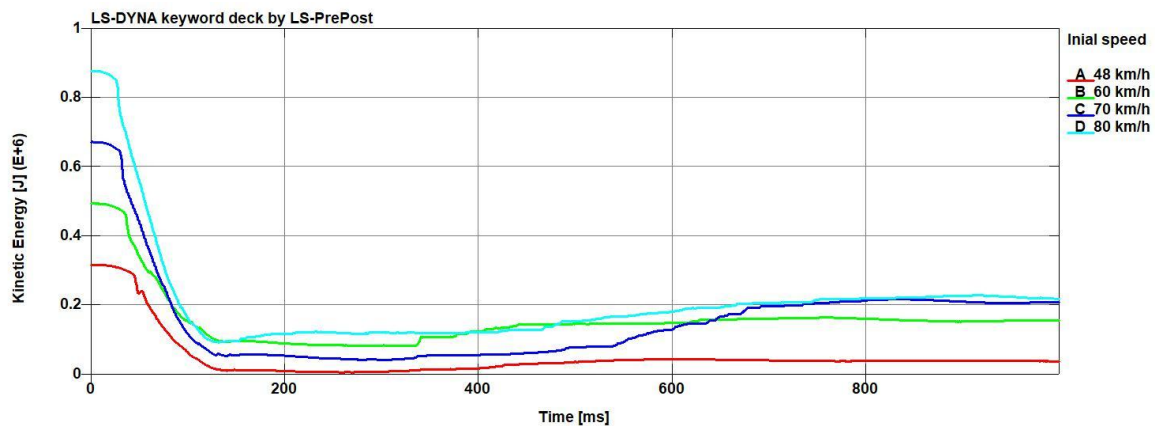


Figure 34: Kinetic energy comparison at different initial speeds.

It is possible to affirm that the main parts involved in the impact are the longitudinal beams, the cross member under engine, engine surface and the cabin floor. These parts absorb much of the energy of the impact in all the simulations in this experiment, as it is shown in Figure 35. As previously stated, the complex interactions between the various parts change in every simulation in a non-predictable way.

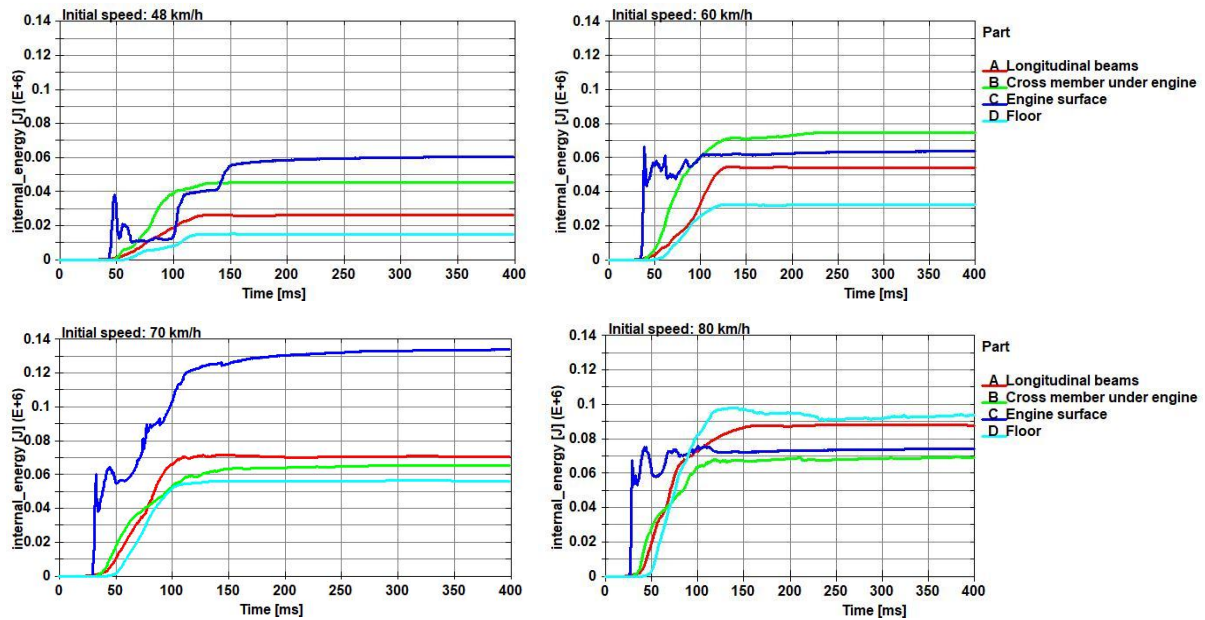


Figure 35: Internal energy comparison at different initial speeds.

Lastly, it is important to notice how the engine interpenetrates deeply with the bollard in the 60 and 80 km/h simulations as shown in Figure 36. The cause of this significant penetration could be attributed to the failure of the elements of the engine surface that are eroded during the impact and create an error in the contact surface detection algorithm. A simple experiment has been set up to understand the cause of this interaction and will be described in detail.

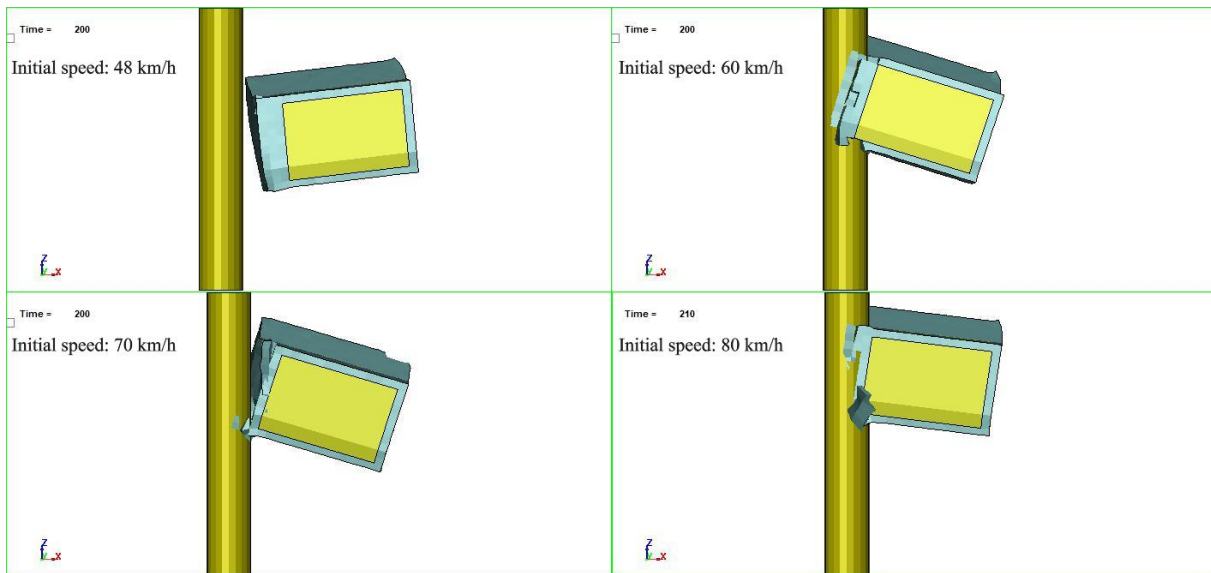


Figure 36: Bollard - engine interpenetration.

Figure 37 illustrates the elements in contact with the bollard which are eroded, highlighted in brown. Eroded elements alter the force exchange surface. The contact algorithm used in the model is an AUTOMATIC_type contact. It is highly effective in dealing with crash simulations. However, it does not update the contact surface in case of deleted elements as in the case of ERODED_type algorithms.

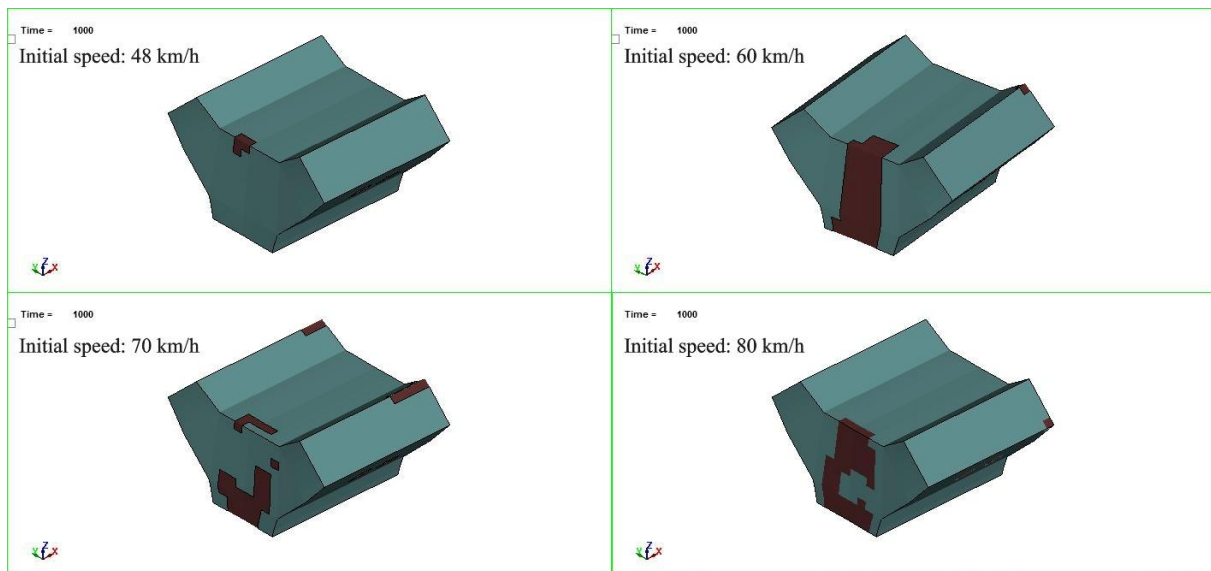


Figure 37: Engine surface eroded elements.

Simplified model

The simplified model shown in Figure 38 has been set up to test the contact algorithm type effect on the engine penetration. The bollard (1) has been modelled in the same way it is in the N1 generic vehicle model: It is made of rigid steel, with EL16 shell formulation. The rigid part or core of the engine (2) has been simplified as a solid rigid metal parallelepiped. It is made of steel with lower density to simulate the empty volumes of the engine block, just as in the reference N1 model and it is moving at 60 km/h towards the bollard. The engine surface (3) has been also modelled as in the N1 generic vehicle with same section and material properties. The goal of the engine surface is to create a soft surface to prevent direct rigid-on-rigid part impact and prevent unrealistic force peaks. However, the elasto-plastic material (M024) is set to fail at 1 mm plastic strain, and the failure of these elements could hinder the contact algorithm efficacy if not taken into consideration. The frame front bumper (4) has been modelled as a simple strip of metal shell elements with the y direction extremities are fixed in space.

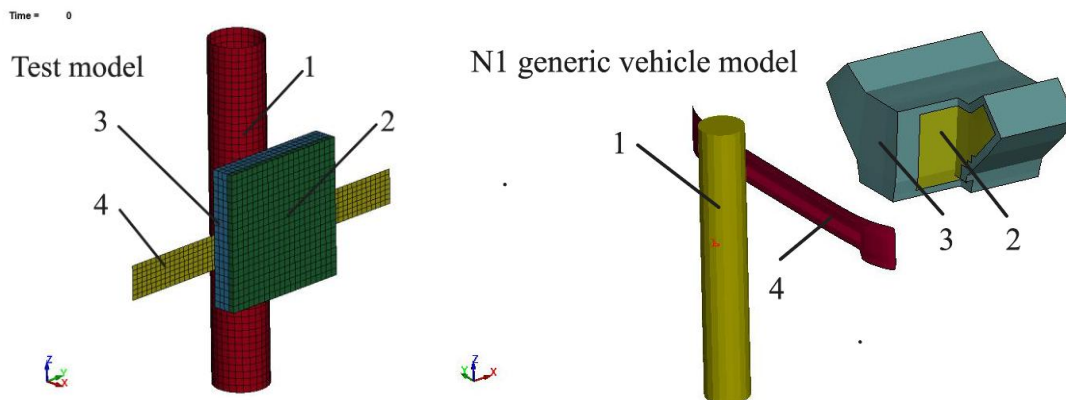


Figure 38: Simplified impact model.

Two versions of this test models have been set up: one uses the same contact parameters of the N1 generic vehicle model, while the other switches the “vehicle x bollard” contact formulation from AUTOMATIC to ERODING, while keeping the same settings unchanged.

As it is possible to see in Figure 39, at the same time the two simulations display radically different outcomes: The ERODING simulation correctly calculates the rebound of the engine simplified model away from the bollard while the AUTOMATIC simulation replicates the results of the N1 generic vehicle model with the engine stuck inside the bollard. The frame front bumper is also included among

the entangled parts and compenetrated the engine block. In the lower part of Figure 39 can be seen that some elements in contact with the bollard incur failure.

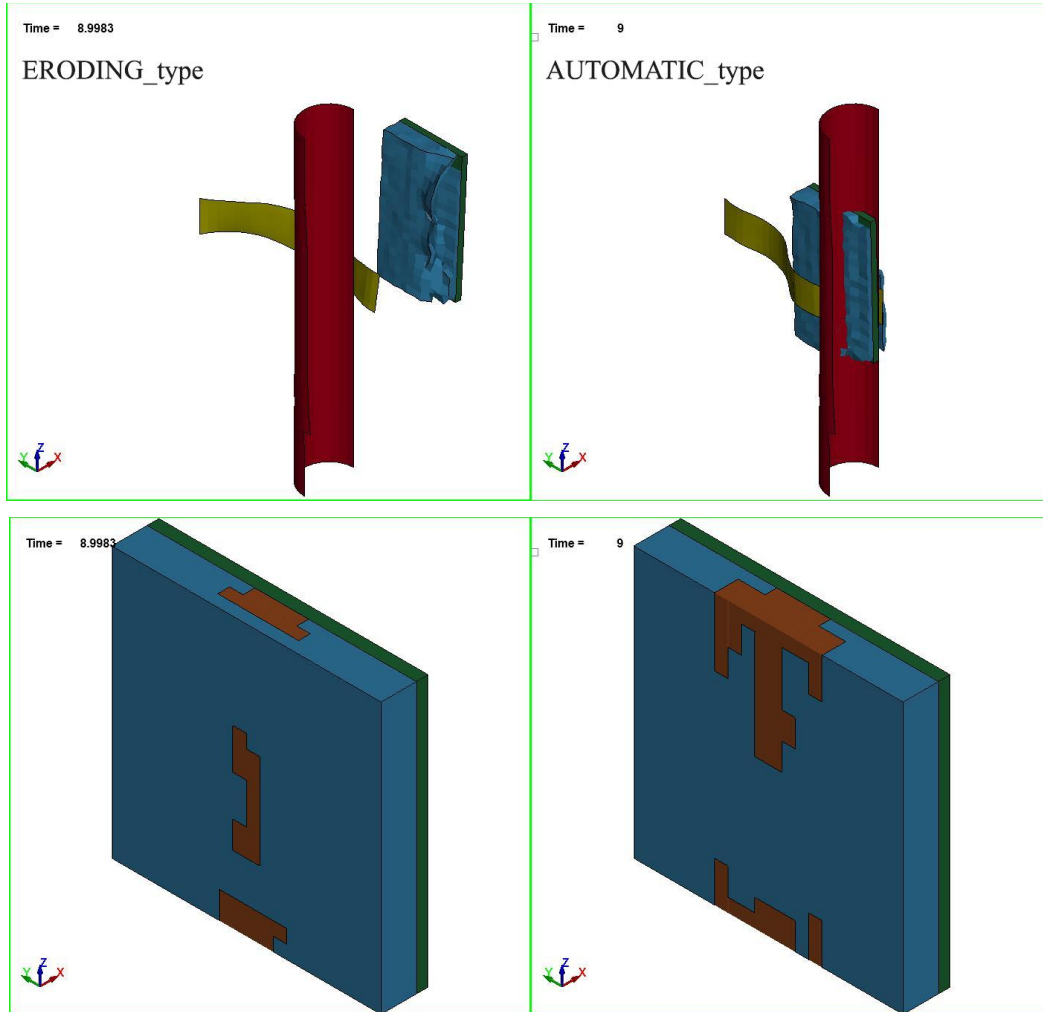


Figure 39: Contact type influence on penetration.

Comparing Figure 39 with Figure 37 it is possible to see the similarities in the eroded elements pattern, and it is also possible to correlate the number of eroded elements with the penetration of the engine into the bollard. Namely, the 70 km/h simulation displays the least number of eroded elements, and the bollard-engine excessive penetration is reduced, as it is displayed in Figure 40.

Moreover, the excessive penetration of the engine generates negative peaks in the contact force, which are usually due to unwanted initial penetrations. The contact energy is generated from the friction

between sliding surfaces and must be positive [9]. The negative sliding energy is correlated to the amount of engine-bollard penetration.

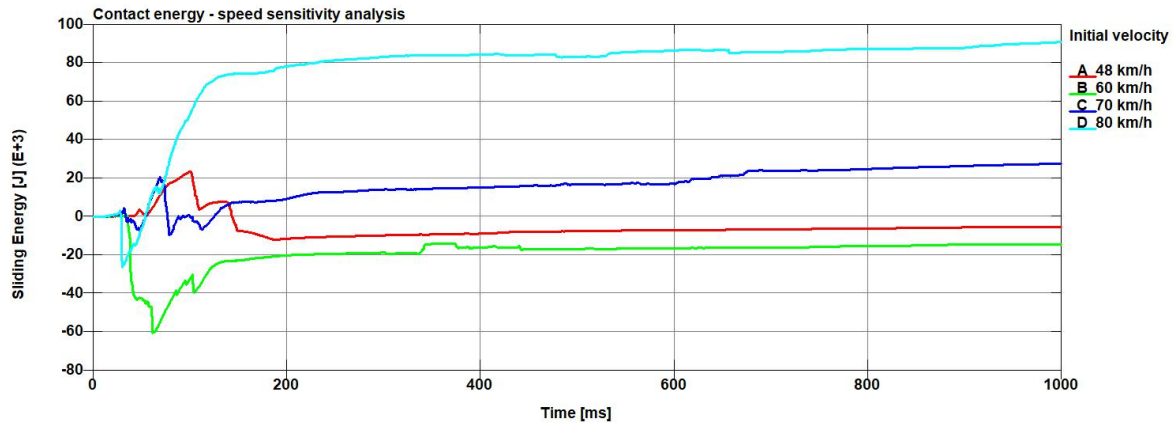


Figure 40: Contact energy comparison at different initial speeds.

Conclusions

The initial speed plays a fundamental role in the impact evolution: the amount of energy to be dissipated changes drastically between the simulations, and the bulk of this energy is absorbed by a small set of parts. After a certain threshold, the engine, frame and cross member are not sufficient to stop the vehicle motion, and the cabin floor becomes the main energy dissipator as the engine penetrates the cabin.

The duration of the impact event is almost the same regardless the initial speed in this study. However, this result may be misleading because the engine gets stuck in the bollard in an unrealistic way.

The model has issues in dealing with higher energetic impact with respect to the validated simulation. Simply switching the contact algorithm type from automatic to eroding, however, is not sufficient to solve the issue. Further studies and tests could be carried to improve the model stability.

It is possible to see in Figure 34 that even after the impact with the static barrier, there is some residual kinetic energy in all the simulations. This phenomenon is accentuated in higher initial speed simulations. This is not representative of a physical phenomenon, but the residual kinetic energy is stored in deleted and severely hourglass parts, as will be better illustrated in the next chapter.

Chapter 3: Cross member connection.

From the previous simulations is observed that the cross member undergoes heavy strain and is completely warped around the bollard. This can be considered as not realistic; the cross member should fail before undergoing this large deformation. Some solutions to this problem could be to improve the material properties of the cross member, introducing the strain rate effect or different failure criteria. The solution that will be discussed in the next pages is to change the connection of the cross member from a rigid connection to a connection type with failure criteria.

As opposed to Chapter 1, in which the frame's simple model parts are connected through constrained nodal rigid bodies (CNRB), the connections of the JRC model frame beams are made with constrained node sets. Figure 41 shows the longitudinal beams (1) that are elasto-plastic parts and are alternated by rigid portions (2) which function is to provide a strong connection point of the suspensions to the frame. The non-suspended parts (tires, wheel ribs) are connected to the rigid portions of the frame via discrete spring and damper elements. It is not possible to connect a CNRB to a rigid part in LS-Dyna. Hence, the rigid link with the cross member under engine (3) is simulated by assigning the nodes at the y direction edges of the cross member (8) as belonging to the closest rigid portions of the longitudinal beams. In this way, the motion and forces applied to the cross member are immediately transmitted to the longitudinal beams as if the cross member mesh was fused with those parts. This type of link, however, does not allow for connection failure. The cross member under gearbox (4) is linked to the frame by means of CNRBs (10) The front crush zones (5) are the foremost part of the longitudinal beams, and it is connected through other CNRBs to the front bumper absorbing elements (6) and to the front frame bumper (7). The longitudinal beams have different cross section areas and geometries at along the longitudinal direction (9).

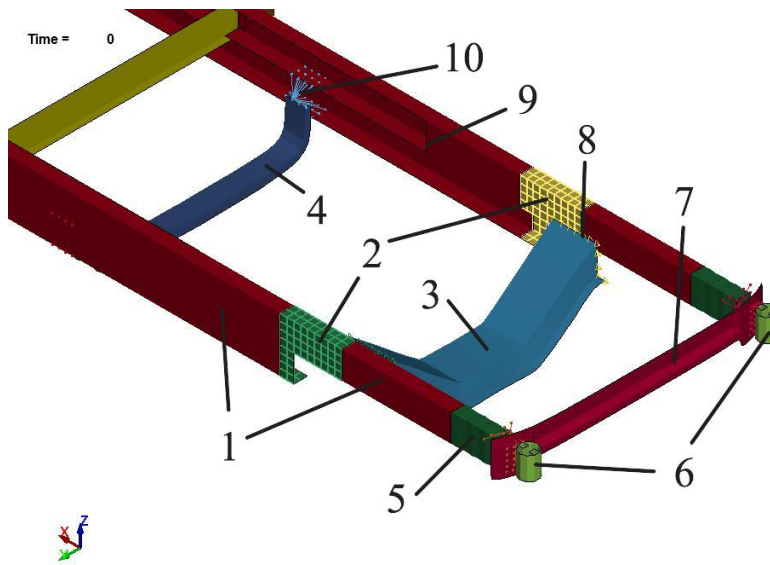


Figure 41: Cross member connection with the frame.

The new connection type considered to solve this issue are spot welds constraints. This type of elements consists in rigid beams that link node pairs, and follow failing criteria based on the normal and tangential force applied to the constrained nodes, the thermal expansion and plastic strain of the connection. In a real frame, flanges of the cross member would be welded or bolted to the longitudinal beams, but in this model the mesh density is too low to allow the same number of spot welds that could be used in a real vehicle. Hence, the force limits of the spot welds must be increased with respect to real spot welds to compensate the lack of junction points.

The failure criteria parameters are described in the LS Dyna keyword user manual [8]. The parameters that have been studied in this work are the normal and shear force limit, SN and SS respectively.

The failure criteria of spot welds are:

$$\left(\frac{|f_n|}{S_n}\right)^N + \left(\frac{|f_s|}{S_s}\right)^M \geq 1$$

Where f_n and f_s are the nodal normal and shear force, respectively. N and M value is set by default at 1. This equation applies only for tensile loads, compressive loads are transmitted with no constraints on the spot weld. A similar solution has been implemented already in the N2A / N3D Generic vehicle model as displayed in Figure 42.

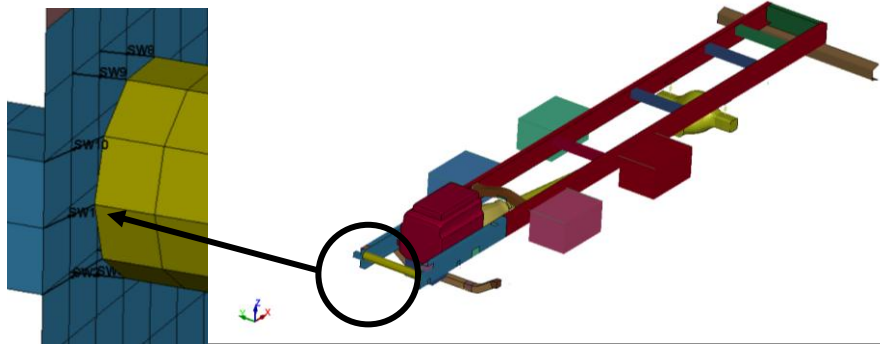


Figure 42: N2A / N3D front cross member spot welds.

As previously stated, spotwelds are rigid beams and thus they cannot be linked to the rigid portions of the frame. This means that either the spotwelds connect the cross member to nodes farther than the ones belonging to the rigid portion, or the longitudinal beams mesh is slightly modified to accommodate the spotwelds. Both cases will be treated in the next pages.

At first, a series of simulations with different force limits will be studied without any modification on the frame mesh. Then, a similar approach will be used for a modified model with smaller rigid portions of the longitudinal beams. Lastly, the effect of shear force is observed by sweeping individually those parameters.

Spotweld connection model

Figure 43 illustrates how utilizing spotwelds (black beams in the image) without mesh adjustments, the created beams are leaning rearwards. This will cause the force distribution to be mainly normal. Hence, in this first segment the normal force will be the most influential parameter at play. Table 4 summarizes the first set of simulation in this study. The highest force values are chosen to be the same as the spotwelds in the N2/N3 model. The values for models 2 and 3 are obtained by reducing the normal force and consequently the shear force so that the SN/SS ratio is kept at 0.7. Values for models 5 and 6 keep lowering the normal force but changing the SN/SS ratio to 0.5. These last two values are more in line with experimental spot weld failure forces at high strain rate [10]. The values of model 5 are doubled to compensate the lack of conjunction points.

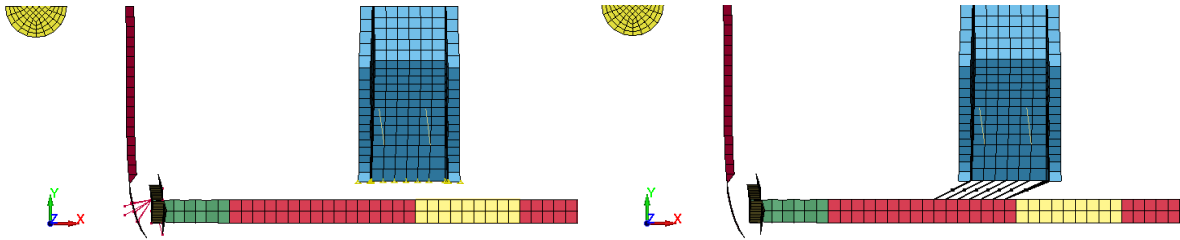


Figure 43: Cross member connection change. Reference model on the left, spot weld model on the right

Model number	Normal limit force	Shear limit force
1	Rigid connection	
2	100 kN	70 kN
3	80 kN	56 kN
4	70 kN	50 kN
5	50 kN	25 kN
6	20 kN	10 kN

Table 4: Cross member connection simulation summary

Spotweld resistance sensitivity analysis

The force history shown in Figure 44 reveals that the different simulation results fall under three main categories: non-failing spot welds, partially failing spot welds and failing spotweld simulations. All of which are noticeably different from the reference rigid model. Models 2 and 3 have the exact same force history, meaning that these models are completely equivalent, notwithstanding the different force limits. This happens because the force applied to all the spotwelds was never enough to cause a spot weld failure in neither model. A slightly different path is observed in the force history of model 4, which diverges from the two previously discussed. Model 4 follows the exact same evolution of models 2 and 3 up to 130 milliseconds into the simulation, then the curve diverges slightly. The explanation to this it that some spot welds incur failure, but not enough to change drastically the simulation evolution. The last two curves instead are noticeably different from the previous ones because eventually all the spot welds incur failure. In the case of model 5, the complete cross member detachment happens after the second force peak, which is to be attributed to a second engine impact with the bollard. Lastly model number 6 show a second small force peak well after the other models. The cross member, and thus the engine, are completely detached from the frame after the first main peak. The engine falls to the ground and the second peak is due to the bollard impacting the cabin floor directly. It can be also noted that the

Chapter 3: Cross member connection.

first peak in all spotwelds model simulations is lower than the rigid model one. The reduced peak causes a limited engine rebound, and thus the second engine impact happens earlier and in more intense with respect to the rigid connection model.

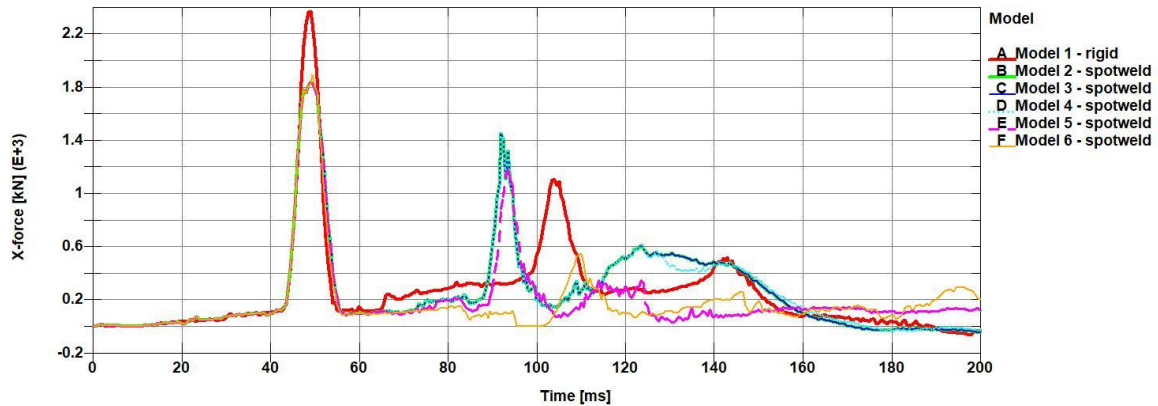


Figure 44: X-force, spotweld resistance sensitivity analysis.

In Figure 45 snapshots of the simulation at 70 milliseconds time are represented. The previously mentioned differences in behaviour can be observed in detail. Models 2 and 3 has less rebound than model 1 after the main impact, models 2 to 5 are still following the same path since no spot weld failed, while model 6 has already lost all connections between frame and cross member.

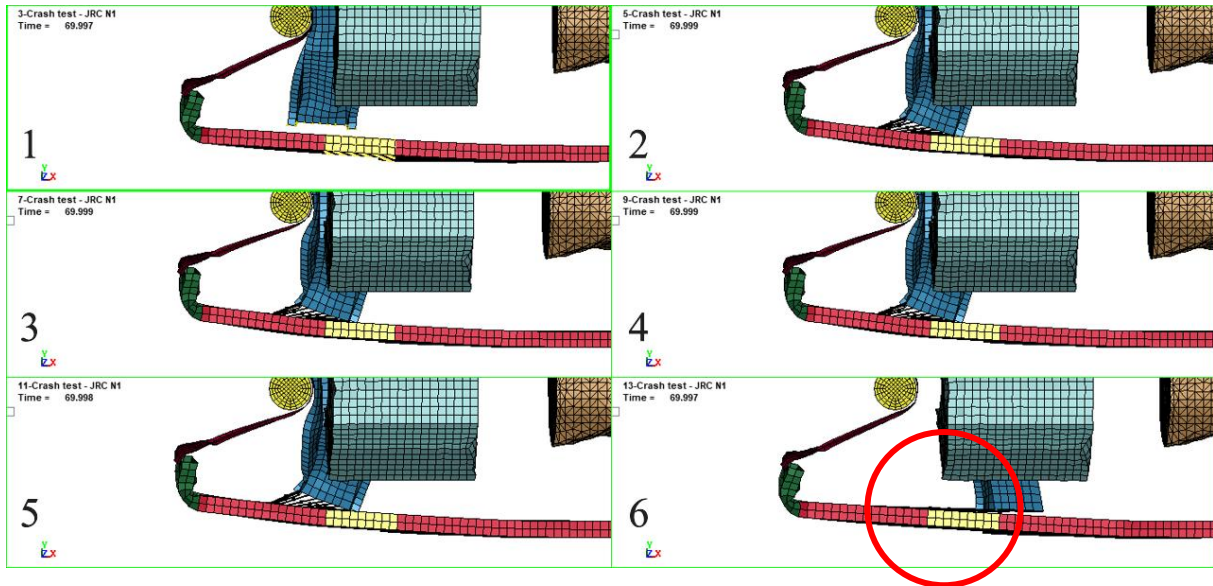


Figure 45: Spotweld resistance sensitivity analysis, 70 ms simulation time.

Figure 46 shows the next decisive step of the simulations at 100 ms, after the second engine impact all spot welds of model 5 fail. The failed beams are not deleted from the simulations and thus are still represented in the pictures. However, the constraints do no longer apply forces between the node pairs.

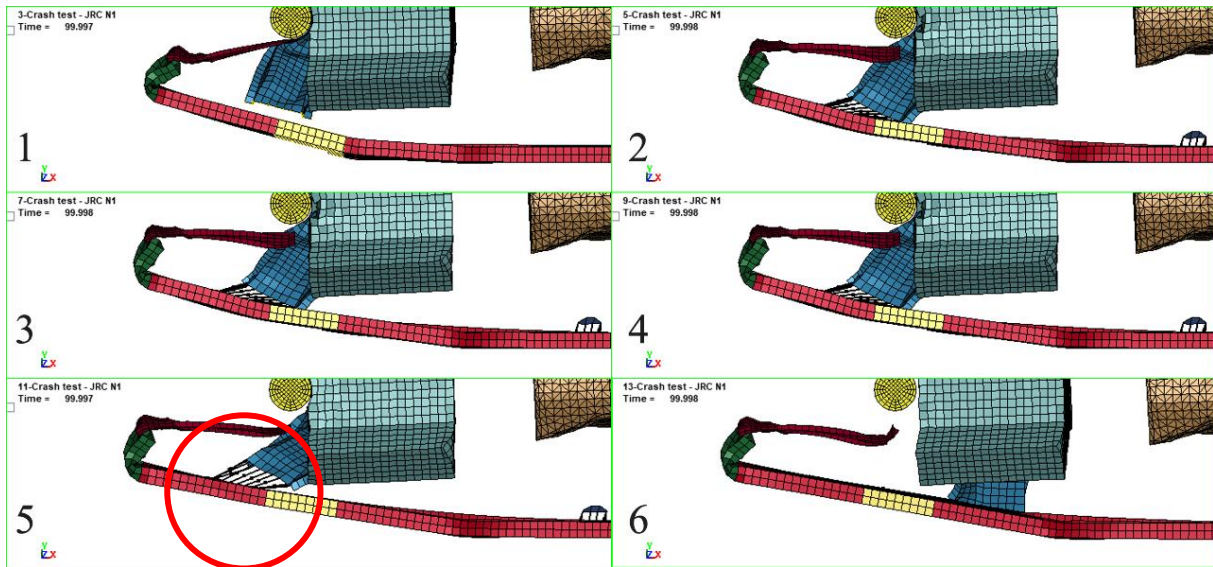


Figure 46: Spotweld resistance sensitivity analysis, 100 ms simulation time.

Chapter 3: Cross member connection.

The next interesting moment to be observed is at 140 milliseconds, when model 4 diverges from models 2 and 3. In this case, the failure of a spot weld causes a force concentration on the adjacent one. In turn, the increased shear stress on the element of the cross member causes one of them to fail, as it is possible to see in Figure 47, in the picture 4. It is also possible to notice that in all spotwelds simulations except from model 6, the welded portion of the cross member under gearbox is torn off the rest of the beam before the spot welds fail. Other considerations can be made about the shape of the longitudinal beam bending. Model 1 has a main bend just after the rigid portion of the beam, which happens because the force in that case is applied directly to the rigid part that cannot bend. Thus, the strain is concentrated at its border. A second bend is observed in all models in the same point and is due to a stress concentration caused by a shape change in the beam, that can be observed in Figure 41. Spotweld models display bending in front of the rigid portion. This bend is less pronounced than the others because it is caused by almost normal load due to the angled spot welds. Moreover, that section of the beam has less cross-section area than the other plastic portions.

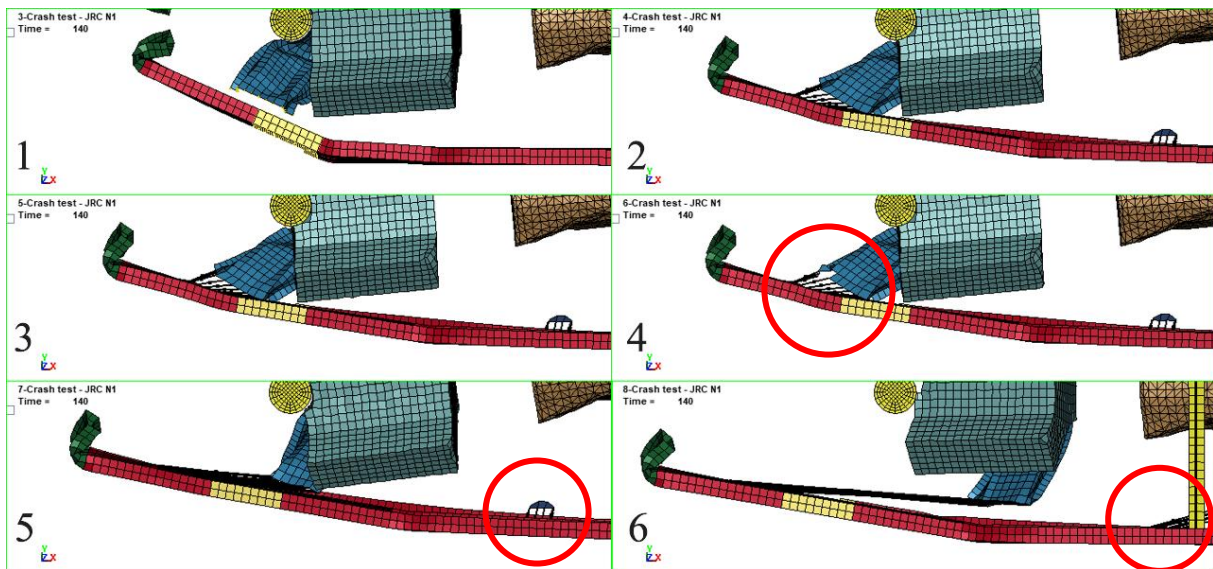


Figure 47: Spotweld resistance sensitivity analysis, 140 ms simulation time.

In Figure 48 it is possible to see that only models 5 and 6 display limited cross member deformation. However, those are the cases in which the cross member is completely detached from the frame.

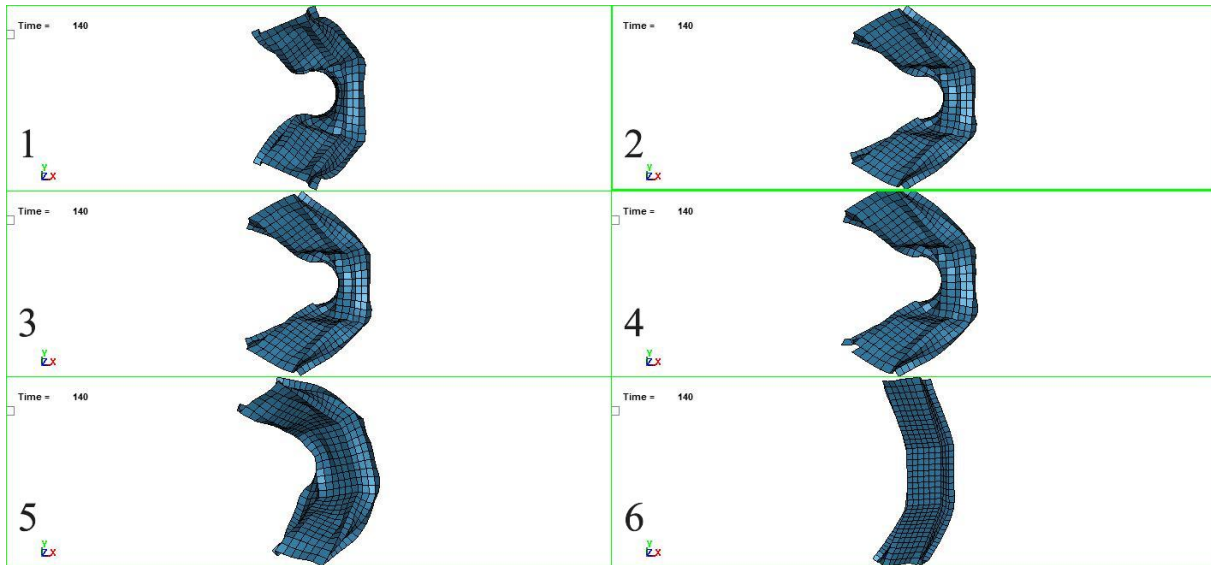


Figure 48: Spotweld resistance sensitivity analysis, cross beam deformation comparison.

An interesting difference between the rigid model and the spotwelds models is the difference in the shape of the cross member at the edges where the link is applied: in the former model, the constrained nodes also belong to the rigid frame portion. Thus, their movement is more limited than the spotweld models, where the cross member edges are able to twist to relieve some of the stress. On the other end, being the spot welds linked to a slender portion of the longitudinal beam as displayed in Figure 49, the movement of the welded nodes is accentuated.

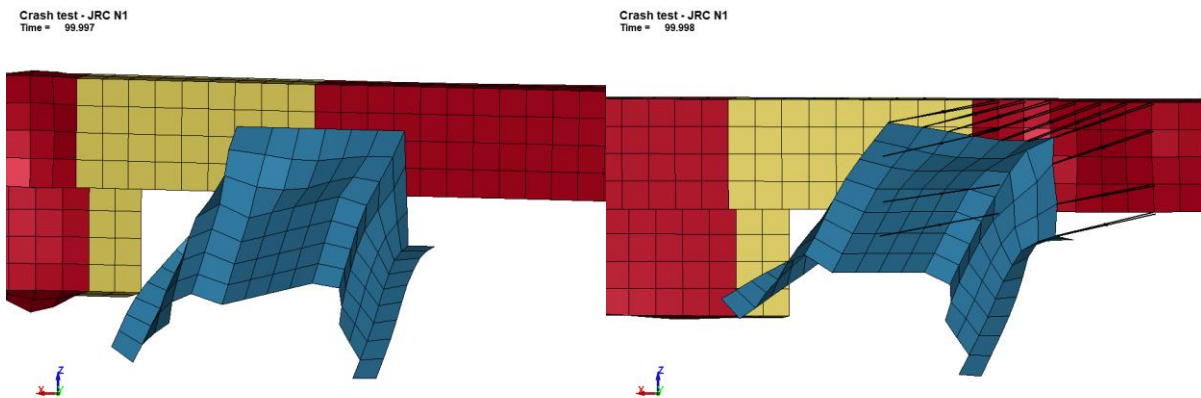


Figure 49: Cross member twisting in spotweld models.

Spotwelds forces

To better understand what happens at the individual spotweld scale, the next section of this study will focus for each model on a given set of nodes illustrated in Figure 50. In the following discussion, individual spot welds will be identified with the corresponding ID (SWID). The engine bolts transmit to the cross beam mainly forces in the x direction, and the main loads seen by the frame are the x and y direction forces the latter of which generates a moment around the z axes. The choice of the spot welds is made to observe the effect of those loads. SWID 20 is the weld closest to the bollard on the top edge of the cross beam, SWID 17 is at the centre of the cross member in the x direction and SWID 14 is the further from the bollard on the same edge of the cross member.

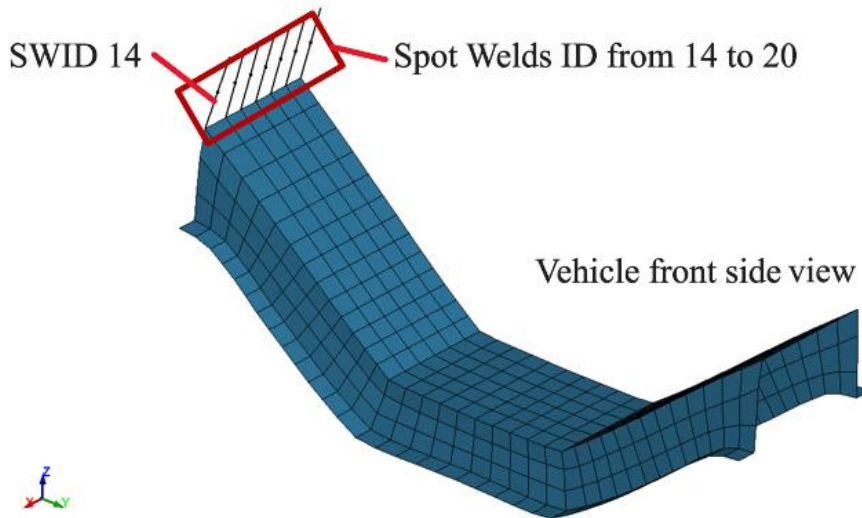


Figure 50: Studied spot welds detail.

As previously mentioned, models 2 and 3 generate identical results and only model 3 is represented in the following discussion. Moreover, the shear force contribution on the failure limit in these simulations is negligible except for model 6. Looking at the leading spot weld of the top edge of the cross member, Figure 51 clearly shows the difference between the simulations. All models follow the same path until the most loaded spotweld fails. More precisely, in model 3 the result can be considered as reference, while in model 4, the fact that some welds incur failure changes the load profile of the curve. The spot weld failure leads to a mesh adjustment that causes SWID 20 to be rapidly unloaded without failure. Model 5 instead initially behaves as models 3 and 4, but during the impact incurs failure and the force

exchanged drops to zero instantly. The same is observed in model 6 which fails almost instantly. In the Model 6 case, failure is reached well before 20 kN of normal force limit because of the shear force contribution. In all simulations, it reaches values of about 8 kN, which is close to the 10 kN threshold.

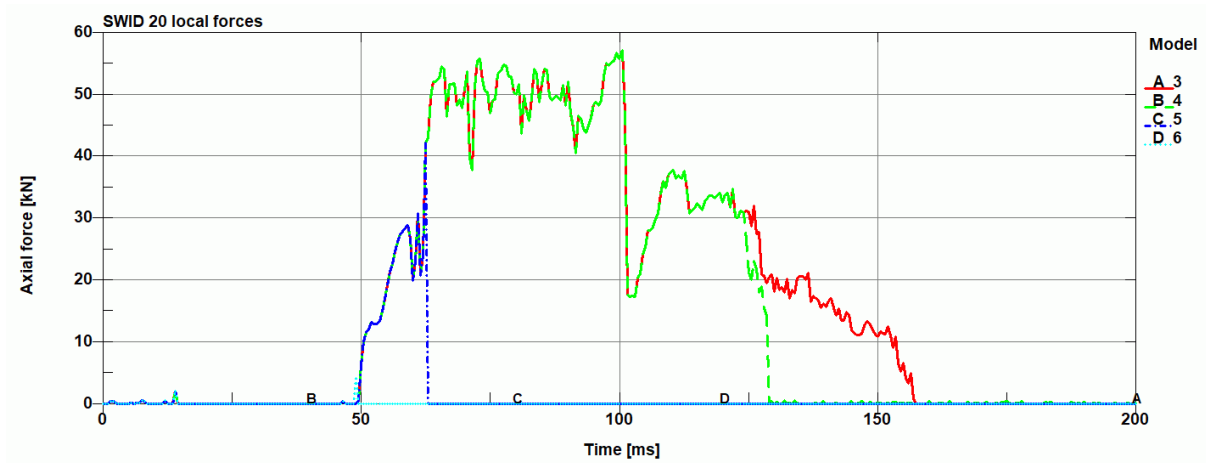


Figure 51: SWID 20 force exchange.

Observing the weld at the centre of the set (Figure 52) it is possible to see interesting differences with respect to the leading node. In model 3 SWID 17 is loaded only in some time intervals and stay loaded during the part of the simulation after the main impact. In model 4 it is possible to see a very short and intense force peak that causes the spot weld to fail. The force peak is due to failure of adjacent nodes that concentrate the force on SWID 17, causing it to fail. The same happens for model 5 and 6 but earlier in the respective simulations.

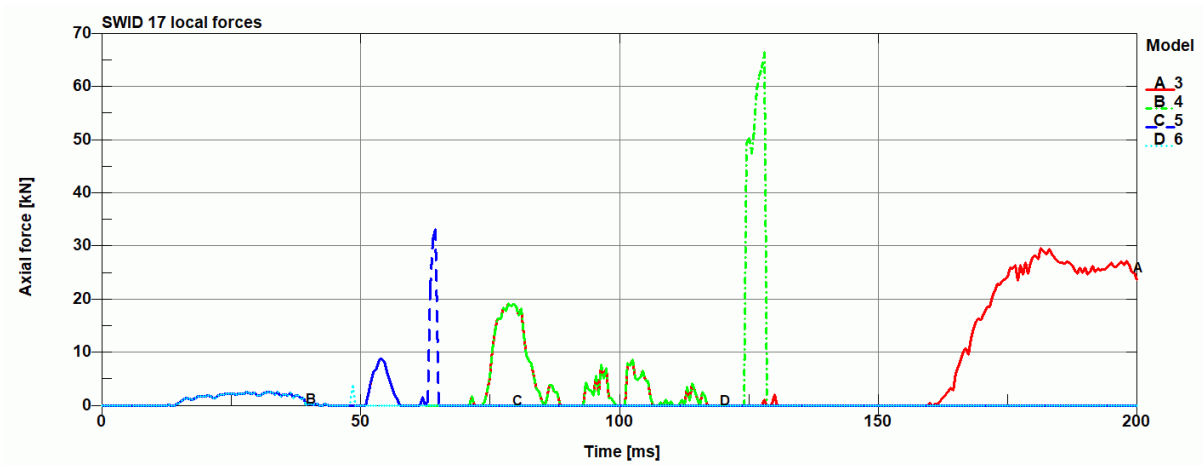


Figure 52: SWID 17 force exchange.

The force exchange after 150 ms is due to the motion of the rear of the car which is raised during the impact while pushing on the bollard. The force exchange continues while the rear falls back down. The fact that the front nodes are displaced during the first impact causes the rear welds to be loaded in their place during later events. Figure 53 shows this phenomenon comparing models 3 and 4: in the latter case the force transmitted from the trailing weld is increased because the spot welds in the front and centre of the top edge failed. The force measured before the first engine impact at 40 ms are due to the bending of the longitudinal beams caused by the front frame bumper.

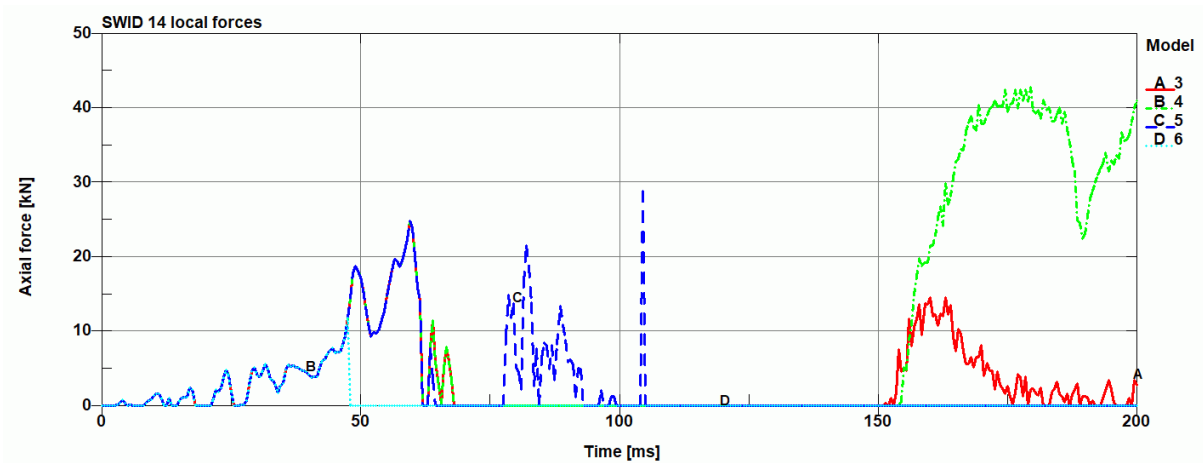


Figure 53: SWID 14 force exchange.

Chapter 3: Cross member connection.

To better understand the sequence of node failure during each simulation, the next step is to observe for individual vehicle model how the different spot welds share the force. Figure 54 illustrates for model 3 how SWID 20 is initially the most loaded node, but the shape change of the beam causes it to unload significantly without failure and the next weld, SWID 19 gets loaded consequently. It is possible to see how the middle and rear welds work mainly in the late stage of the simulation.

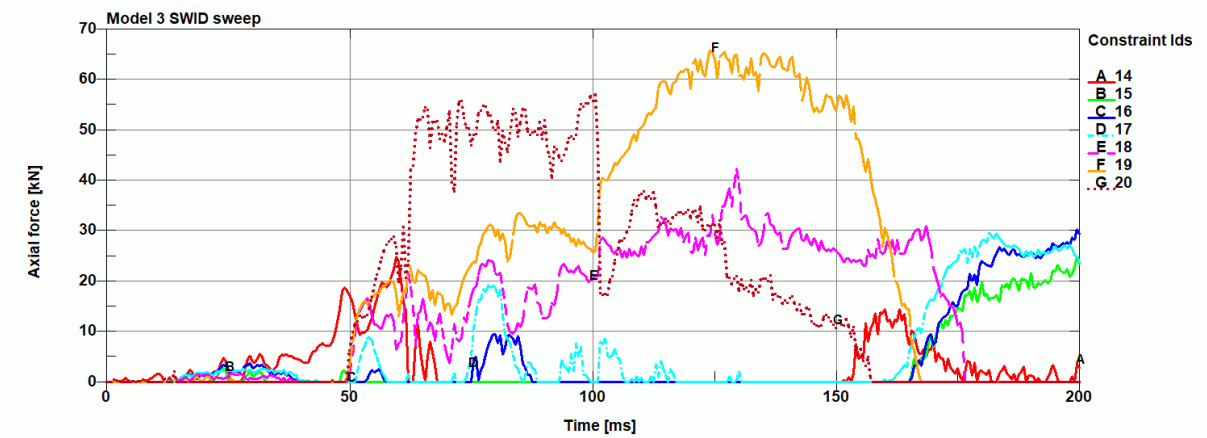


Figure 54: Model 3 SWID sweep.

The same diagram for model 4 is displayed in Figure 55 and it reveals that SWID 20 follows a very similar path to model 3 until 125 ms, when the subsequent nodes 19, 17 and 16 all fail in rapid succession. Nodes 15 and 14 must bear all the load. SWID 20 and 18 are rapidly unloaded although they do not incur failure.

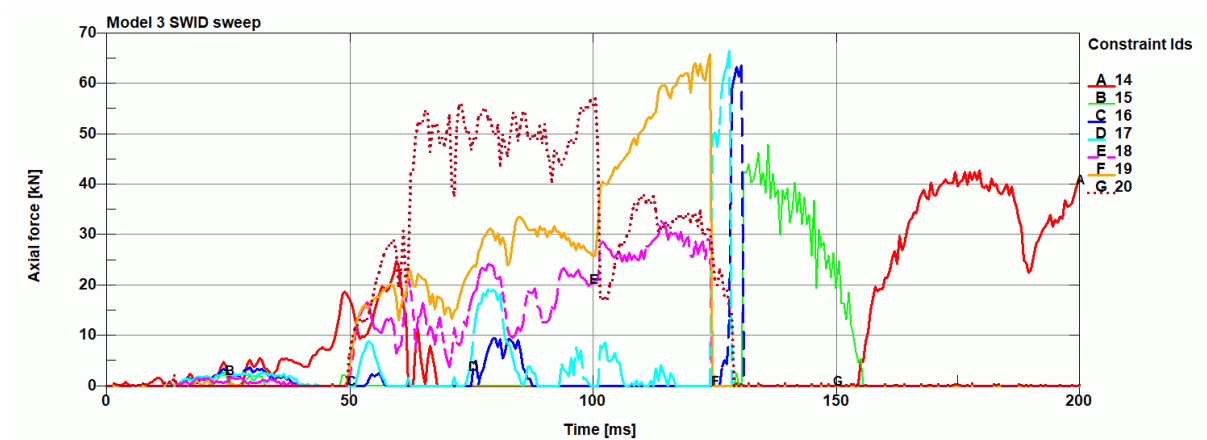


Figure 55: Model 4 SWID sweep.

Models 5 and 6 show the rapid failure of all the spotweld, in line with what previously discussed.

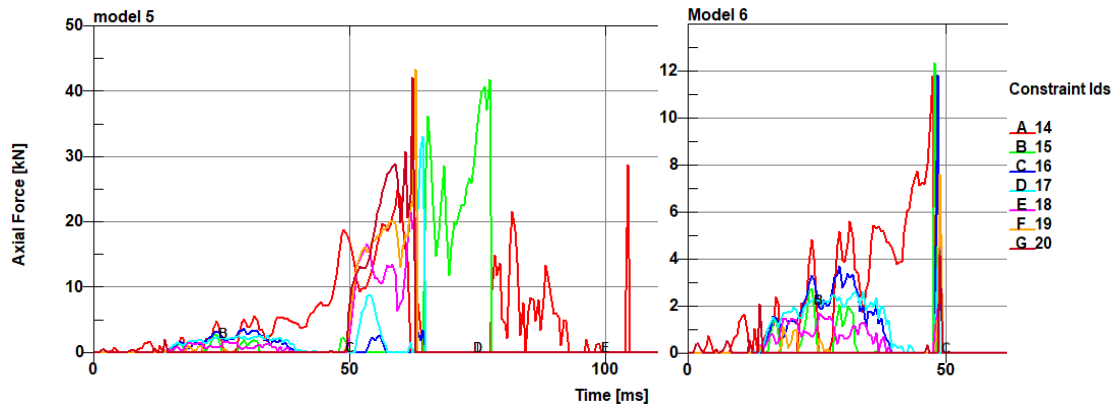


Figure 56: Model 5 and 6 SWID sweep.

Spot weld models validation

To understand if the modification to the cross beam connection is viable and could be applied to the generic model it is possible to replicate the validation process already done [7] comparing the motion of reference points of the vehicle body of all 6 the virtual models with experimental data obtained from a crash test video. The reference points are shown in Figure 57.

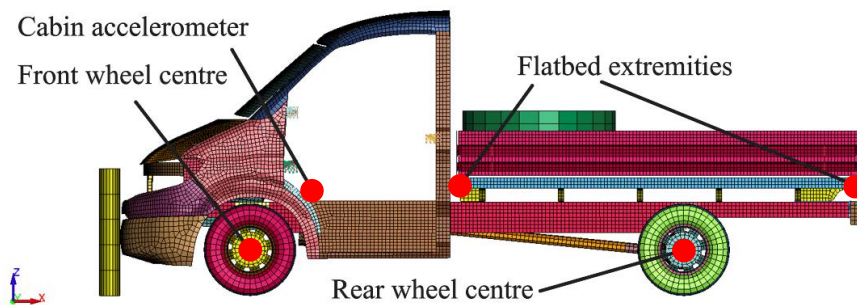


Figure 57: Validation reference points.

The first parameter that can be compared with the experimental results is the penetration of the bollard into the vehicle, it is measured as the x displacement of the front end of the flatbed. In Figure 58 it is immediately clear that none of the spot weld models follows a trajectory as close to the experimental vehicle as the rigid connection model. Simulations 2, and 4 are closer than models 5 and 6 to the

experimental curve, but the penetration in the engine bay of the bollard is still higher with respect to the reference model. Models 5 and 6 have much higher penetration of the bollard due to the complete failure of the cross member connection.

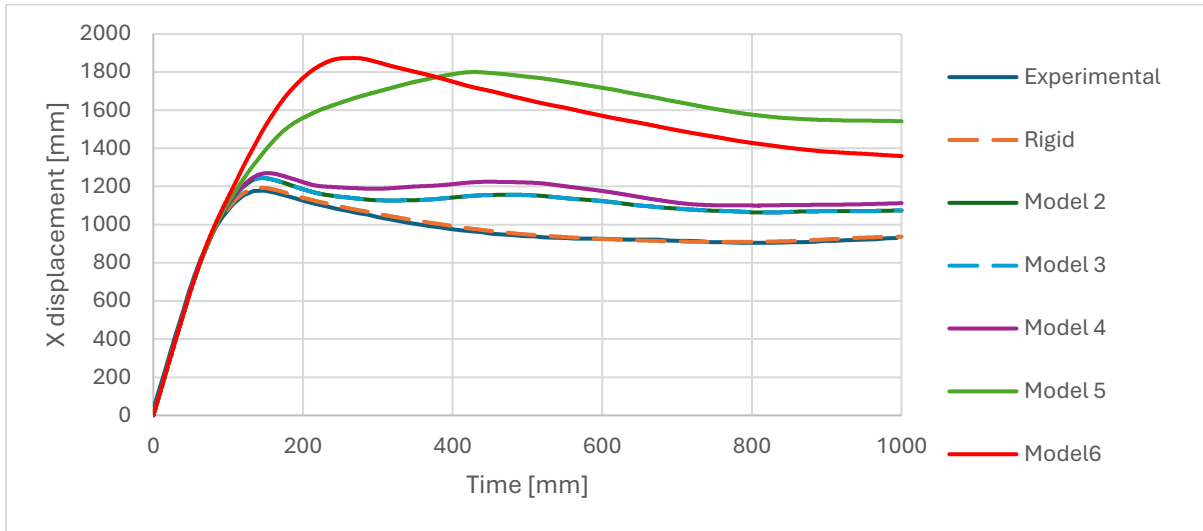
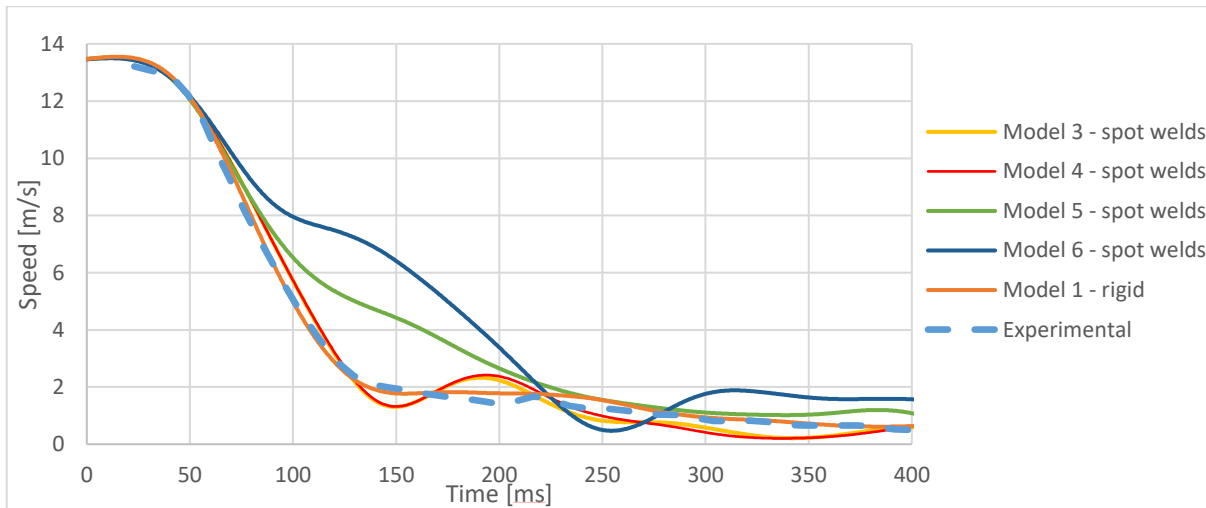


Figure 58: Bollard penetration.

The deceleration of the vehicle shown in Figure 59 is defined as the instantaneous velocity of the front of the vehicle flatbed in the XZ plane. The simulation output curve has considerable noise. Hence, the curve has been filtered with a SAE 60 filter to make it clearer. Models 2, 3 and 4 follow closely the experimental values, while models 5 and 6 have much slower decelerations. Model 1 is the closest to the experimental results in this case also.



Chapter 3: Cross member connection.

Figure 59: Flatbed deceleration.

The same behaviour can be observed in Figure 60 and Figure 61 where the XZ plane speed is measured also inside the cabin and at the centre of the front wheel respectively.

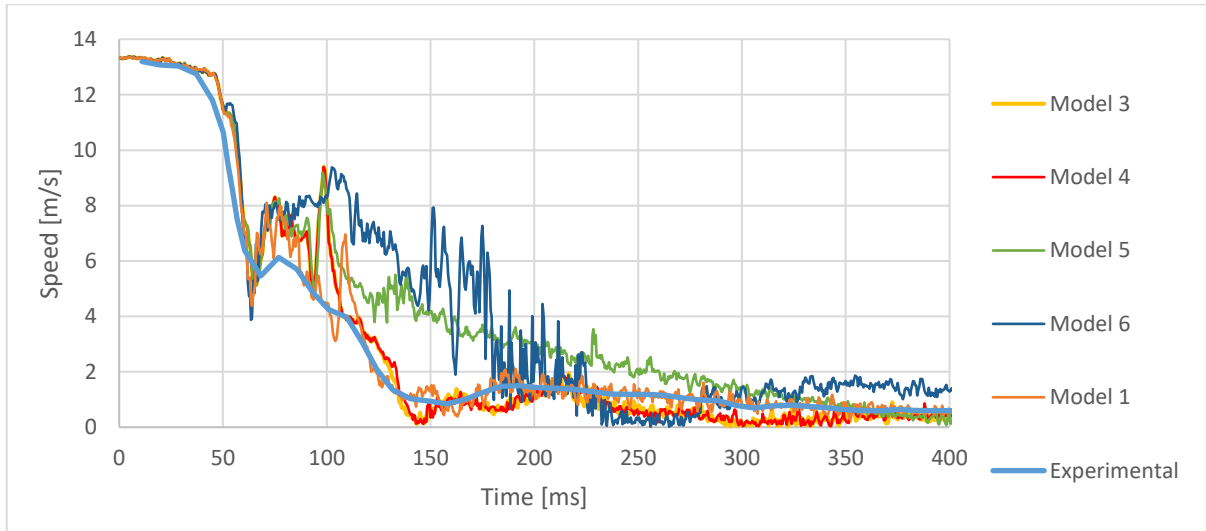


Figure 60: Cabin deceleration.

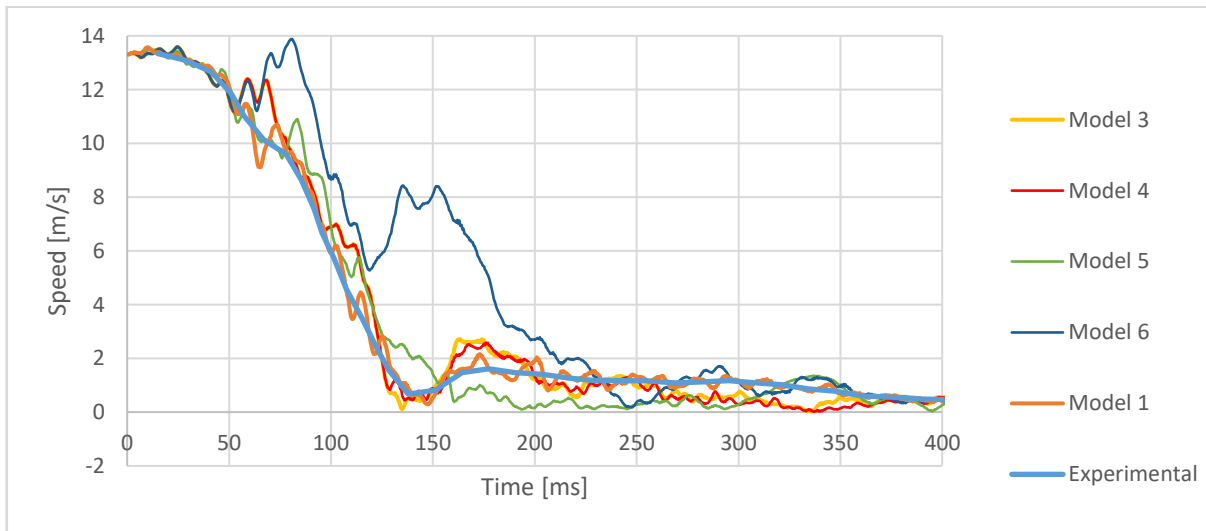


Figure 61: front wheel deceleration.

The vertical motion of the flatbed is also influenced by the connection between the cross member and the longitudinal beams. Models 2 to 4 reach higher z displacement of the rear end of the flatbed. Models 5 and 6 instead show the opposite trend. Model 5 reaches half the height of the experimental test. This happens because the detached powertrain and the bollard push the vehicle body vertically without

constraining the forward movement. Instead, in the model 6 case the bollard pierces the cabin floor, and this causes the forward motion of the vehicle to be impaired and thus the inertia of the rear of the vehicle causes it to reach higher z displacement. The same observations can be drawn looking at the pitch of the flatbed in Figure 63

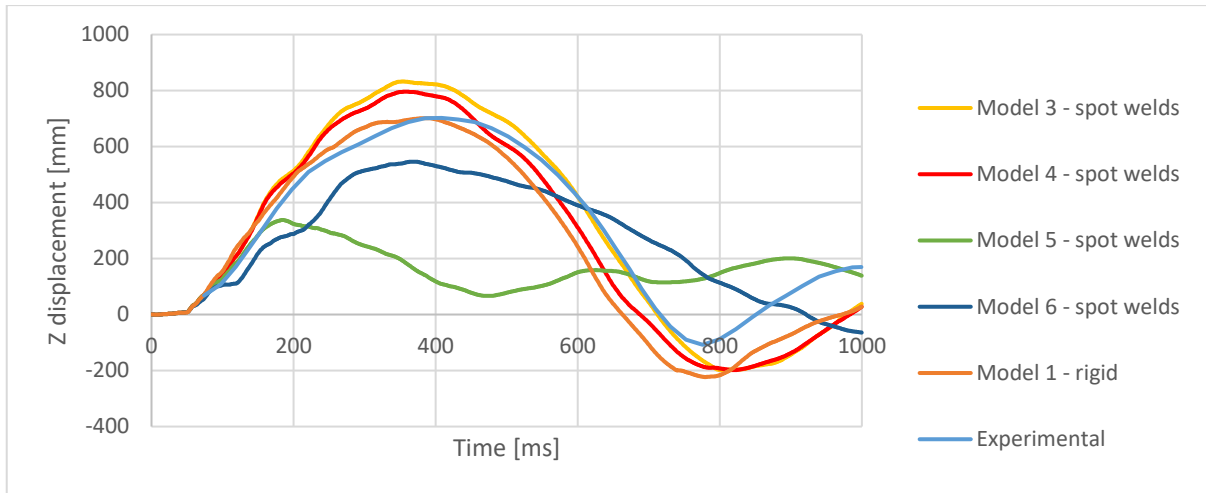


Figure 62: Rear flatbed z displacement.

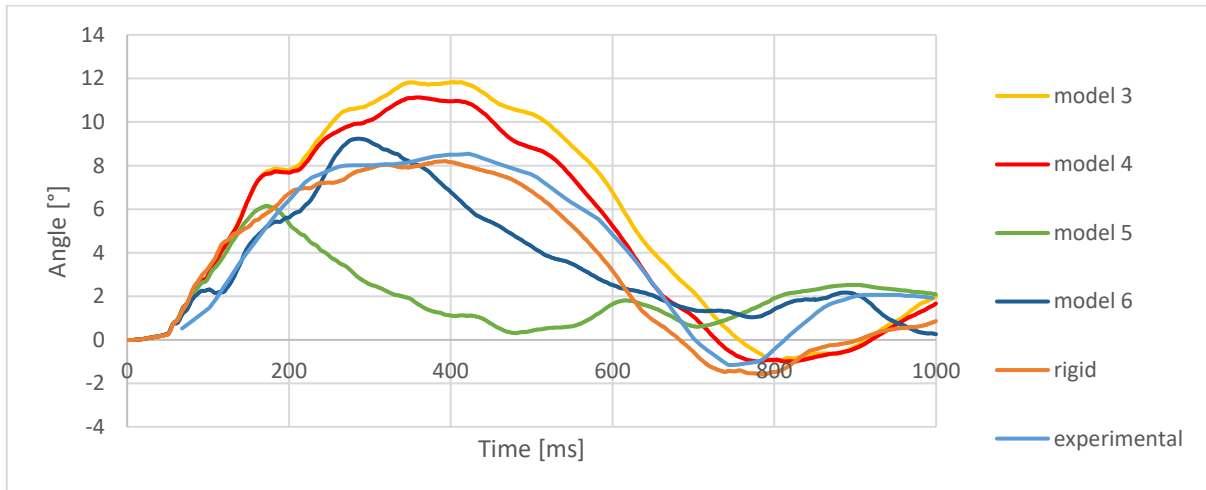


Figure 63: Flatbed pitch motion.

Mesh adjustment

As anticipated in the introduction of this chapter, a separate set of models with similar force limit parameters and an adjusted mesh that can accommodate straight spot weld links has been developed.

Moreover, a model with the modified mesh and the rigid constraint of the cross member has been created to understand the effect of the mesh difference and the spot welds individually.

The mesh adjustment is shown in Figure 58: Bollard it consists in re-assigning some rigid elements that were part of the rigid longitudinal beam portion, to the elasto-plastic portion of the beam. In this way the only effect on the whole longitudinal beam is to reduce the length of the rigid portion. In Figure 64 the top left image corresponds to the reference model: the JRC N1 generic vehicle, the top right image shows the remeshed model with the constrained external nodes of the cross member. The bottom right image shows the spotwelds applied to a non-remeshed frame and the bottom right image displays the spotwelds implemented in a remeshed frame.

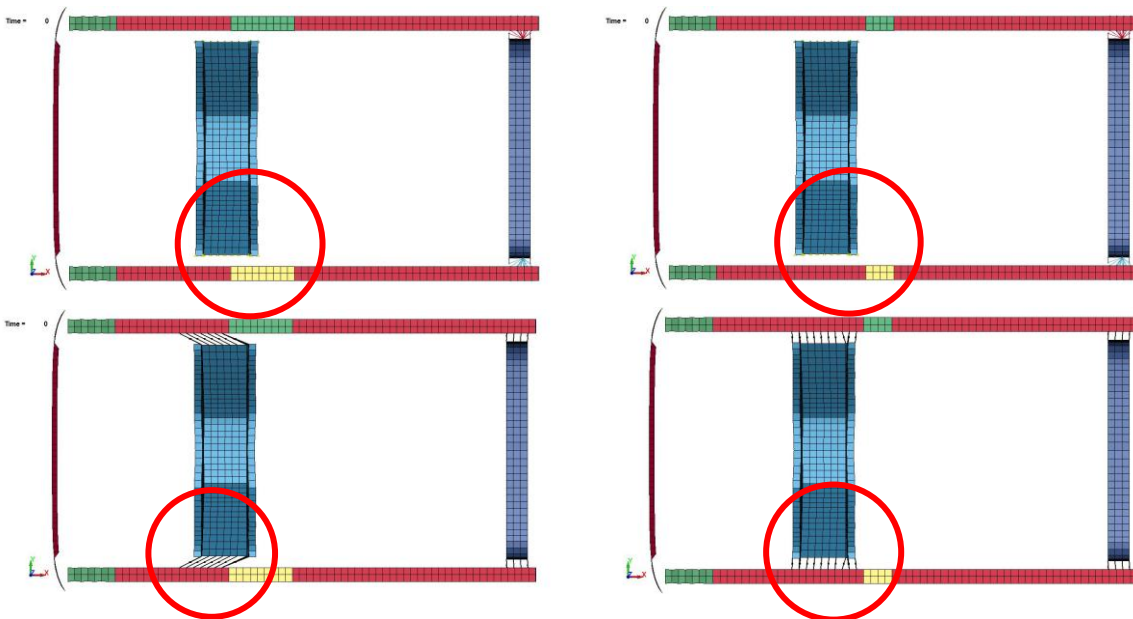


Figure 64: Mesh adjusted model.

Remeshed model rigid

Before the spot weld study is replicated for the new mesh, it is useful to observe how the new mesh will affect the simulation while keeping the same connection strategy of the constrained external nodes. In other words, it will be highlighted the effect of the size of the rigid portion of the longitudinal beams.

Figure 65 shows that it is sufficient to alter the mesh as previously discussed to have a significant impact on the simulation results: the remeshed model reach a lower peak force value in the main impact event,

Chapter 3: Cross member connection.

thus the engine is pushed back less than in the reference model case. This causes the second impact to occur earlier. The force differences between the second and third peak of the reference model are due to the different motion of the engine, that in the reference case slides beneath the floor. In the remeshed model, instead, it gets stuck between the cabin floor and the bollard, providing an early and more prolonged third peak as can be observed in Figure 66.

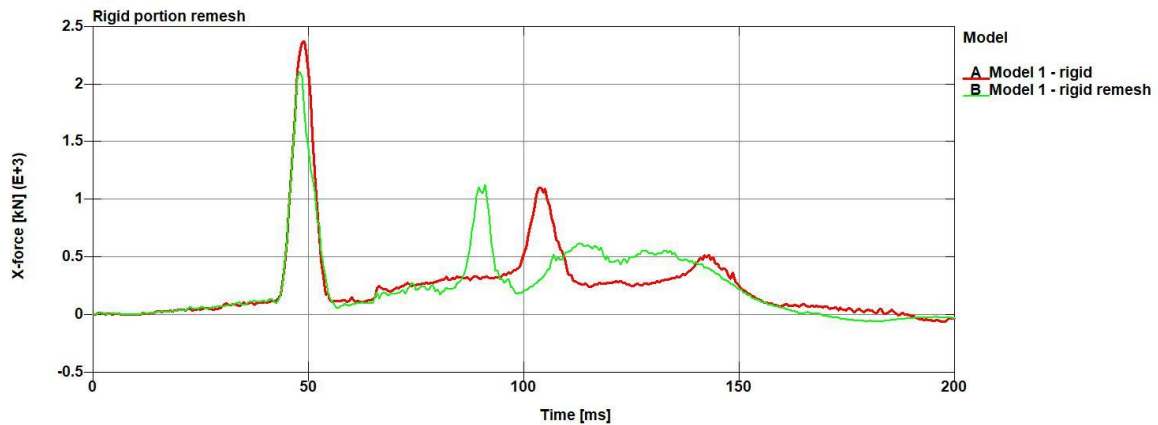


Figure 65: X-force, remeshed rigid model.

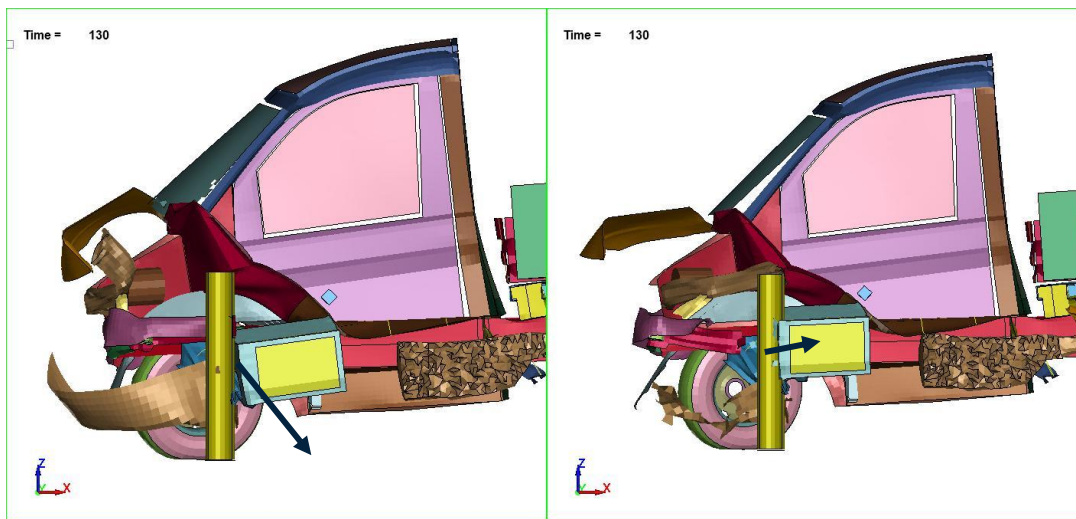


Figure 66: Engine travel, remeshed rigid model, 130 ms.

Chapter 3: Cross member connection.

Both the interpenetration of the engine in the bollard and the kinetic energy shape in Figure 67 reveal that also these models show engine surface element deletion and high hourglass. An interesting comparison can be made between the energy history from the global point of view and the individual parts point of view. Matsum database in LS Dyna contains the energy history of the individual parts, and all those contributions are added, the plot shape appears remarkably different from the global energy curve. Although some minor differences are due to the difference in the strategy the two algorithms use to perform the calculations, the crucial difference in this case is made by the eroded energy: matsum database does not keep track of it while the global database does. The kinetic energy in the global database is higher because eroded elements are deleted while moving at high velocity. Instead, in the matsum curves the differences between the reference and remeshed models are almost negligible.

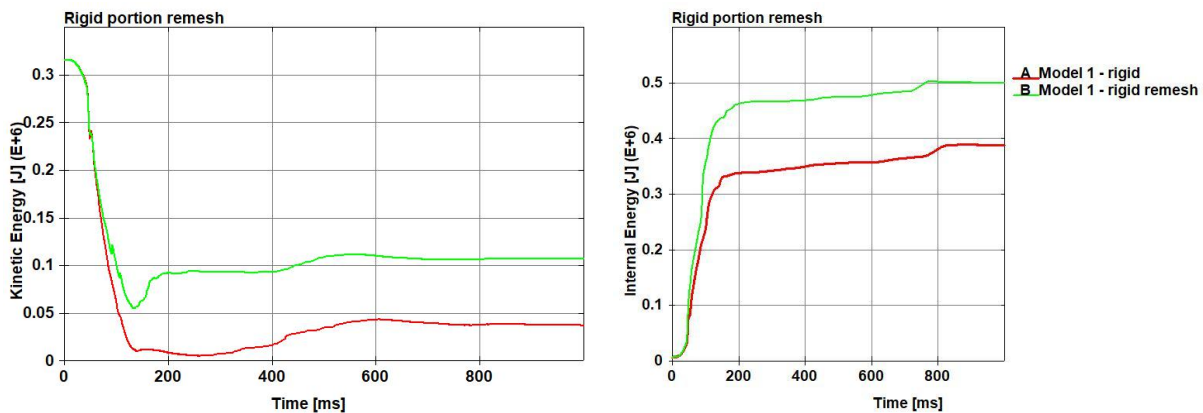


Figure 67: Kinetic and internal energy, remeshed rigid model glstat.

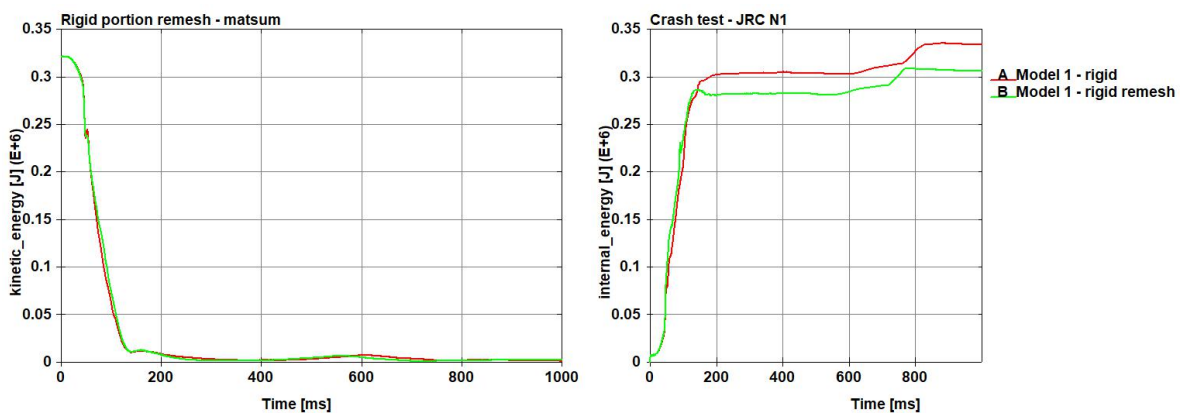


Figure 68: Kinetic and internal energy, remeshed rigid model matsum.

The issue of the late high value of kinetic energy can be explained uncoupling the eroded energy contribution from the total energy in glstat database. As previously stated, the eroded energy is the energy stored in elements that are removed from the simulation consequently to the reach of a failure criterion. Figure 69 shows the total kinetic energy, the eroded kinetic energy and the eroded hourglass energy for model 1 remesh. It is possible to notice that the kinetic energy at simulation end is almost entirely eroded energy. This means that in the actual model this energy is not present and is correlated with the quantity of eroded elements and the time of failure. Another interesting aspect is that the shape of the eroded kinetic and eroded hourglass energy is, for the most part, symmetric. This suggests that the deleted elements are heavily hourglass. Since glstat database uses nodal velocities to compute the kinetic energy, the hourglass motion of the nodes increases artificially the kinetic energy.

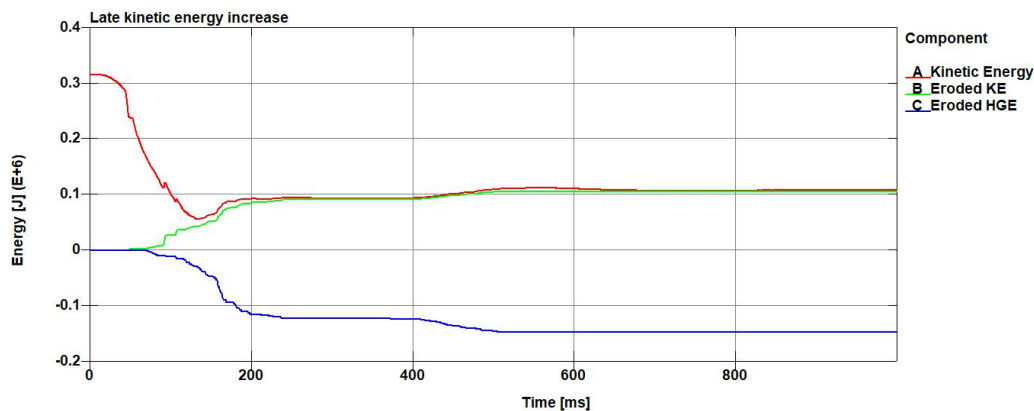


Figure 69: eroded hourglass and kinetic energy, model 1 remesh.

This problem can be mitigated substituting the most hourglass parts with fully integrated elements. However, as can be seen in Figure 70, this does not solve completely the issue of the eroded kinetic energy, but it is noticeably reduced. The model 1 remesh EL16 is obtaining substituting the shell section of the most hourglass parts from EL2 to EI16. Those parts are the tires and the wheel rims, the front bumper and front fascia. Substituting all EL2 formulation with EL16 the hourglass is completely adverted, but the simulation would be slowed. The computational burden to solve fully integrated elements is 2.5 times the EL2 one.

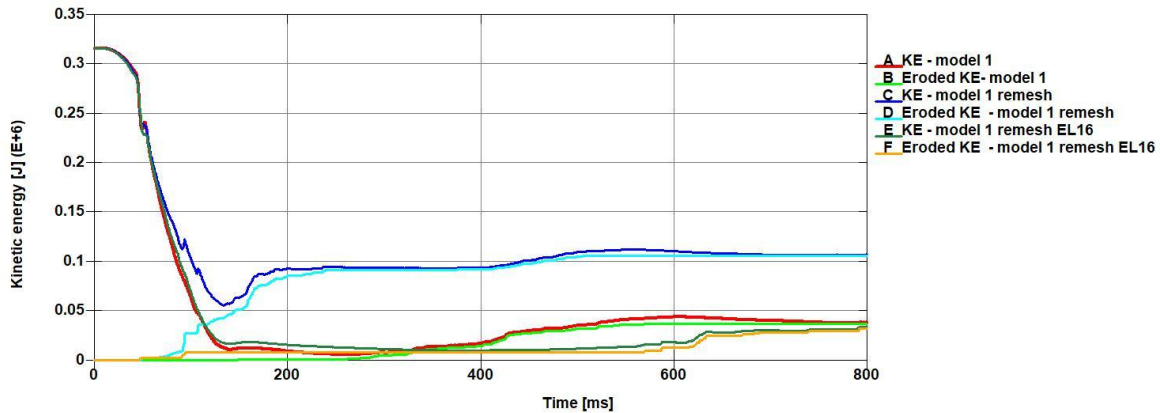


Figure 70: Global kinetic energy, shell formulation effect.

Spotweld resistance sensitivity analysis – remeshed model

The next section will be covering the same analysis as for the spot weld resistance sensitivity analysis. As opposed to before, knowing that neither model 2 nor model 3 incurred in spot weld failure, Model 2 has been replaced in the following study with the remeshed rigid portion model with the external node set constraint, and it will be referred as Model 2.

Model number	Normal limit force	Shear limit force
1	Rigid connection	
2	Rigid connection	
3	80 kN	56 kN
4	70 kN	50 kN
5	50 kN	25 kN
6	20 kN	10 kN

Table 5: Cross member connection simulation summary, remeshed model

Referring to Figure 71, as observed before, the spot welds simulations can be grouped in different cases according to how many spot welds incur failure: Models 3 and 4 both had no spot weld failures and as predicted, they follow the same force history path. Model 5 had some spot weld failures while Model 6 spot welds failed in the first engine impact as for the previous case. There is a substantial difference in the force history of model 2: The first impact has less area underneath the curve, which corresponds to the energy transmitted by the contact force. This in turn causes the engine to spring back less and thus

anticipate the second and third impacts. The peak value in all cases is less than Model 1, as in the previous case, but in Model 2 the shape of the curve is shifted in the earlier time direction as opposed to later as in the case of the spot welds models. The different path could be attributed to the different number of nodes that are loaded simultaneously: when the rigid connection is in place, the nodes at the extremities of the cross member are considered as belonging to the rigid portion, and it shares the mesh with the rest of the beam, which keeps pressing forward due to its inertia. Instead, in the spot weld models, the force is transmitted only through the coupled spotweld nodes, and their displacement gradually loads the surrounding mesh. Hence, the small lag manifests. Models 3, 4 and 5 follow the same path up to the second impact, when model 5 spot welds start failing. Model 6 instead has no more working welds right after the first engine impact.

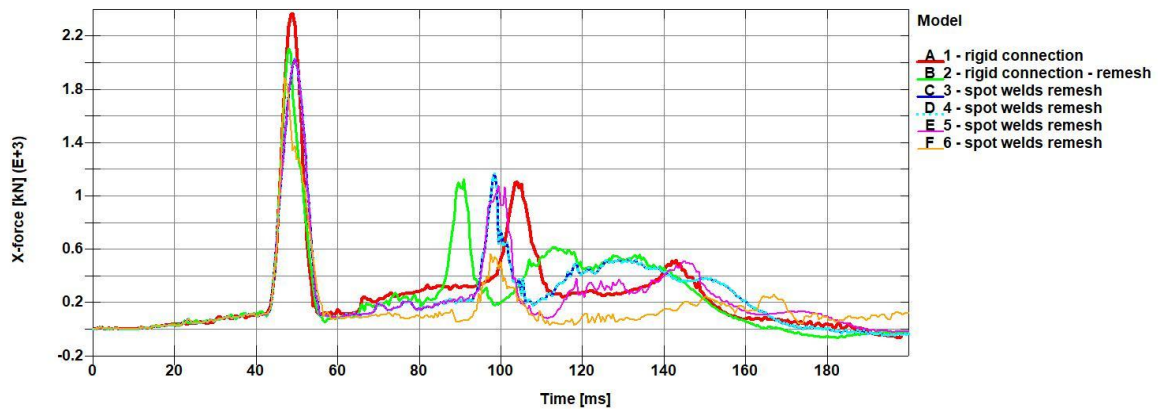


Figure 71: X-force, spotweld resistance sensitivity analysis, remeshed model.

Figure 72 shows the response of the various models to the first engine impact. At this stage, there is much less difference between the rigid connection and the spot welds, except for the case of model 6, which has lost all its longitudinal – transversal beams connections. For what the cross member under gearbox is concerned, the spot welds never fail. The cross member under engine is slenderer than the

Chapter 3: Cross member connection.

cross member under engine, and thus the elements that hold the cross member in place fail before their connection with the frame.

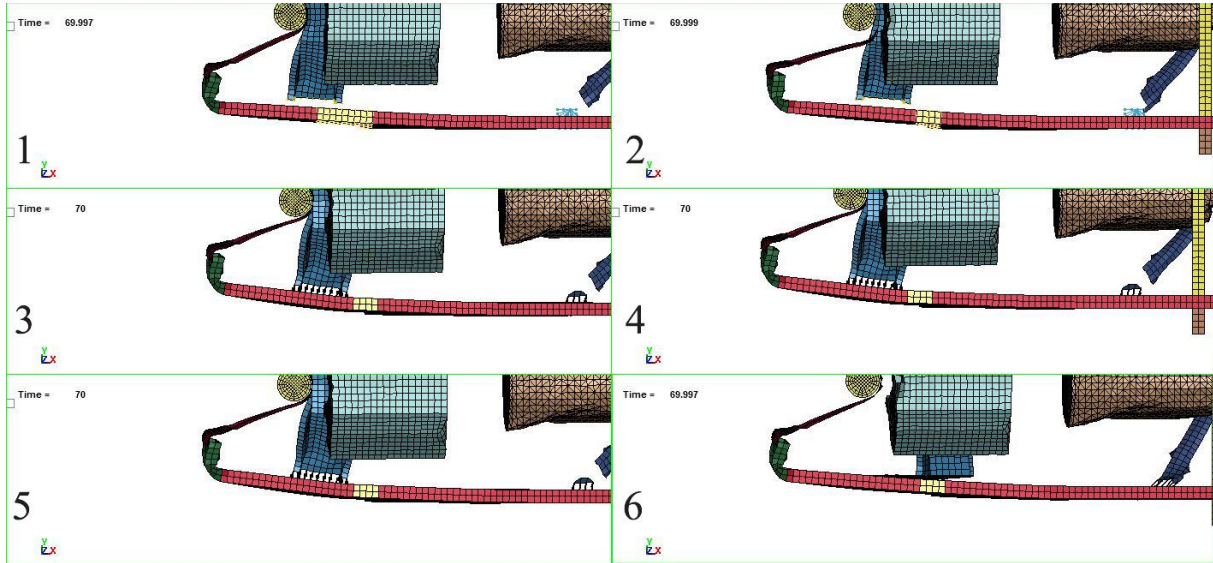


Figure 72: Spotweld resistance sensitivity analysis, 70 ms simulation time, remeshed model.

At the second impact instant represented in Figure 73 the differences in longitudinal beam bending start to emerge. The rigid connection models start bending at the back of the rigid portion, the longitudinal beams bend slightly also at the geometry change location, with limited magnitude in model 2. In all models except for model 1, the frame front bumper is cut by the engine and bollard impact surface. The engine and gearbox in model 6 are completely detached and fall to the ground.

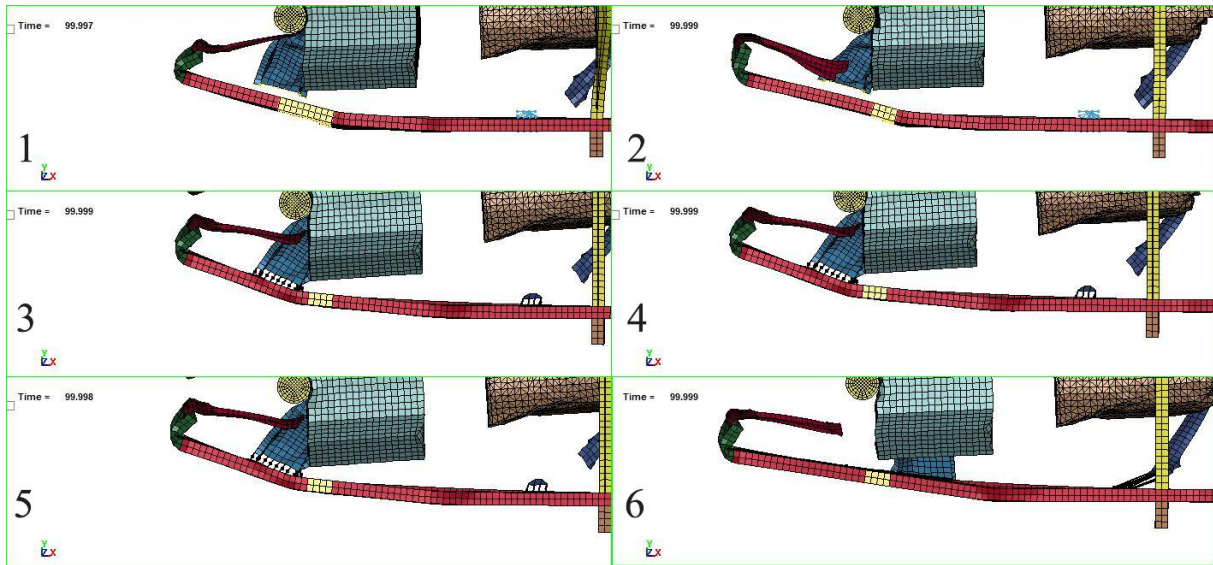


Figure 73: Spotweld resistance sensitivity analysis, 100 ms simulation time, remeshed model.

In Figure 74 it is shown the simulation status at 140 milliseconds. There it is possible to notice that the frame front bumper rupture time changes how the crush zone is deformed: in model 1, it is completely bent on itself, while in model 2 the crush zone points towards the inner engine bay with both sides pointing at each other. In this case, the front parts of the beams enter in contact and create a force in the y direction that bends the longitudinal beam with a positive z torque in the case of the left side of the vehicle which is shown. In models 3 to 6 this effect is limited because the bending of the front crush zone is in between these two cases, causing limited positive z direction torque. Model 5 is attached to the longitudinal beams by only one spot weld, causing an increased displacement of the cross member under gearbox that rotates around the z axis. Model 6 having no more working spotwelds advances much more in the bollard direction, since it is the cabin floor that must provide the energy to stop the vehicle instead of the frame.

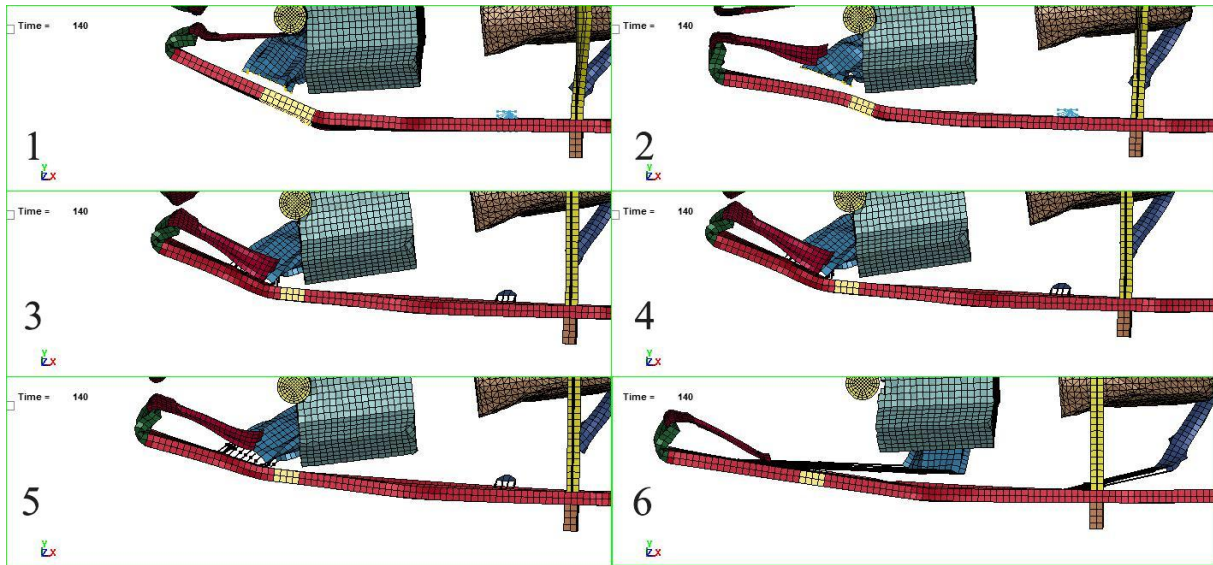


Figure 74: Spotweld resistance sensitivity analysis, 140 ms simulation time, remeshed model.

Figure 75 displays the deformation of the cross beam after the relevant impact events. Minor differences can be observed between models 1 to 5, although at model 5 is barely connected to the frame at this stage. However, it is possible to see that the main difference between the rigid connection and the spotwelds lies in the fact that in the former case, the edges of the cross member cannot deform, and thus the energy absorbed by the part is all concentrated in the impact region at the centre of the beam. Instead, in the spot weld connection case, the coupled nodes at the edge of the frame and the cross member have some more relative displacement allowed that in turn deforms the edges of the cross beam. However, the overall deformation of the beam is extensive, and it is warped around the bollard in all of the cases except to model 6, which undergoes very limited deformation before the connections are broken and it is free to move.

Figure

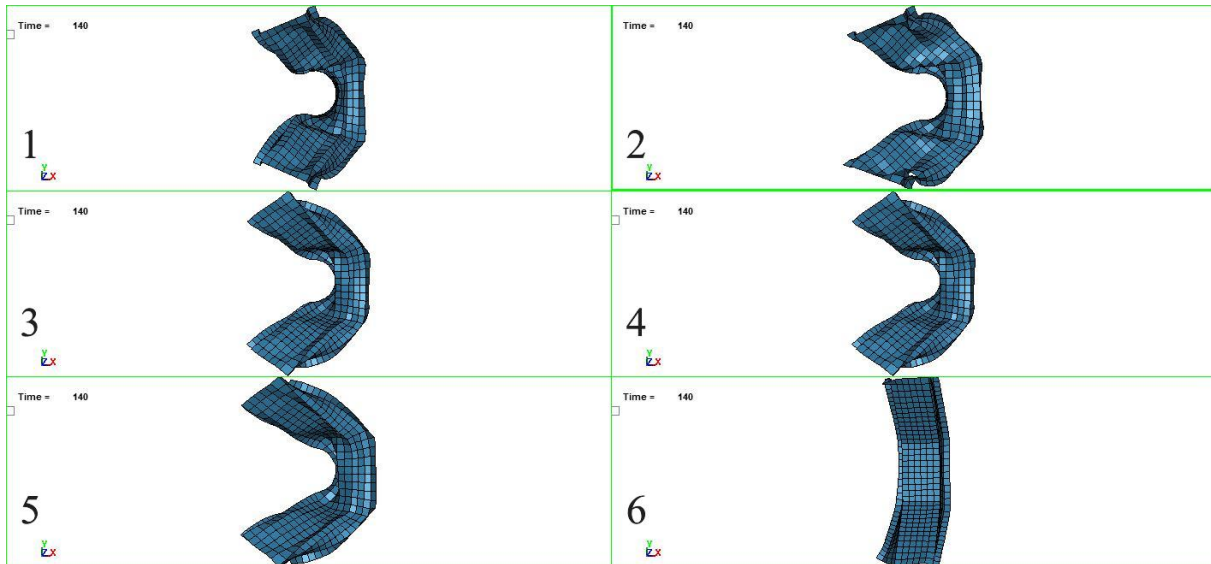


Figure 75: Spotweld resistance sensitivity analysis, cross beam deformation comparison, remeshed model.

As in the reference mesh of the N1 generic vehicle model, rigid connection models maintain the cross member aligned with the rigid frame portion, while the spot welds models exchange forces between elasto-plastic materials, so that there is relative displacement between the paired nodes. In Figure 76 it is also possible to see how the different connections bend different sections of the longitudinal beams: the rigid model (left image) applies torque on the yellow rigid portion. While the front part is relatively free to move, on the other side the frame blocks the free rotation and thus is bent. The spotweld model instead (right image) applies the forces directly onto the thinner anterior section of the beam, bending it inwards and downwards. This type of link is more compliant than the rigid one, hence higher bollard penetration is measured in the validation diagrams.

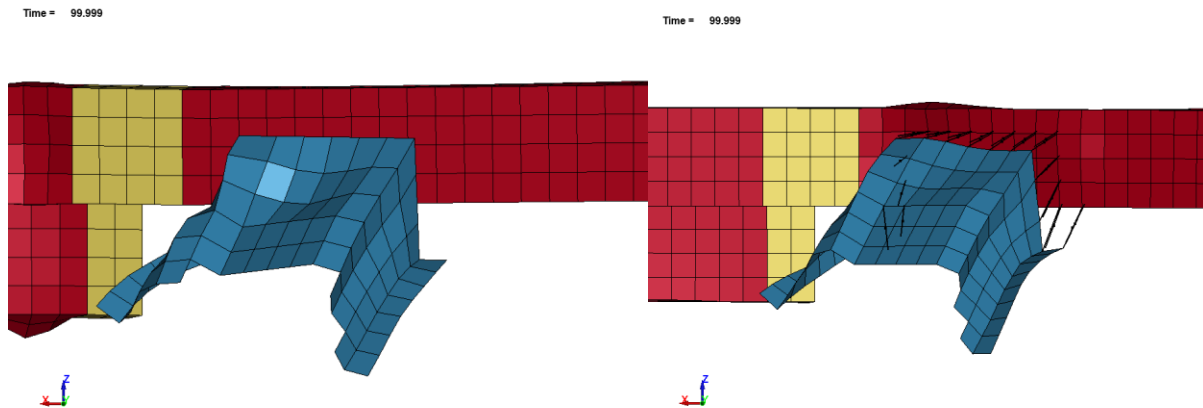


Figure 76: Cross member twisting in spotweld models, remeshed model.

Figure 77 shows the different mechanisms of longitudinal beam bending. The main forces are applied to the longitudinal beam either on the rigid part (green) or to the longitudinal beam (red). The front absorbing elements collide, and their compression is what causes the curvature in model 1 – remeshed and in less measure in model 4 – remeshed. The inclined directions of the spotwelds in model 4 cause the force to be applied almost axially to the longitudinal beams. Thus, the major failure point is the change of geometry illustrated in Figure 41. The bending in front of the rigid section is limited.

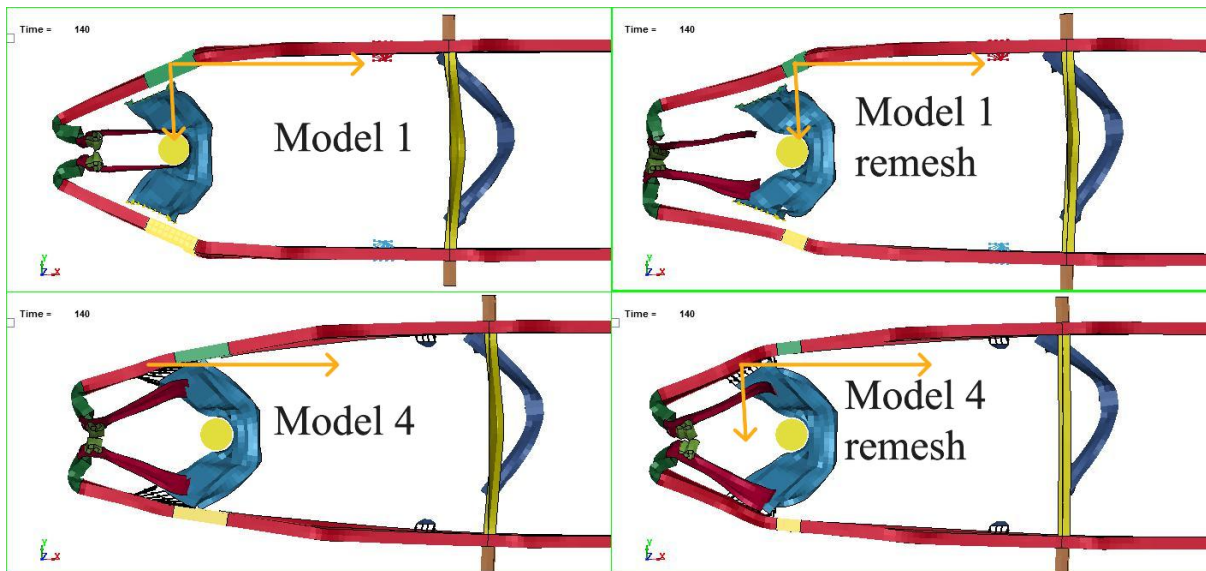


Figure 77: longitudinal beam bending comparison.

Spotwelds forces - remeshed

Similarly to what has been done previously, an in-depth observation of the force exchange at the spot weld level has been made and will be discussed in the following pages. For the adjusted mesh model, the Spot Weld ID of the foremost couple node of the top lateral edge of the cross beam is 25. SWID 22 is at the centre of the edge and SWID 19 is at the rear corner. As mentioned before, in this case the tangential component of the force is no longer negligible and will be considered in the next diagrams.

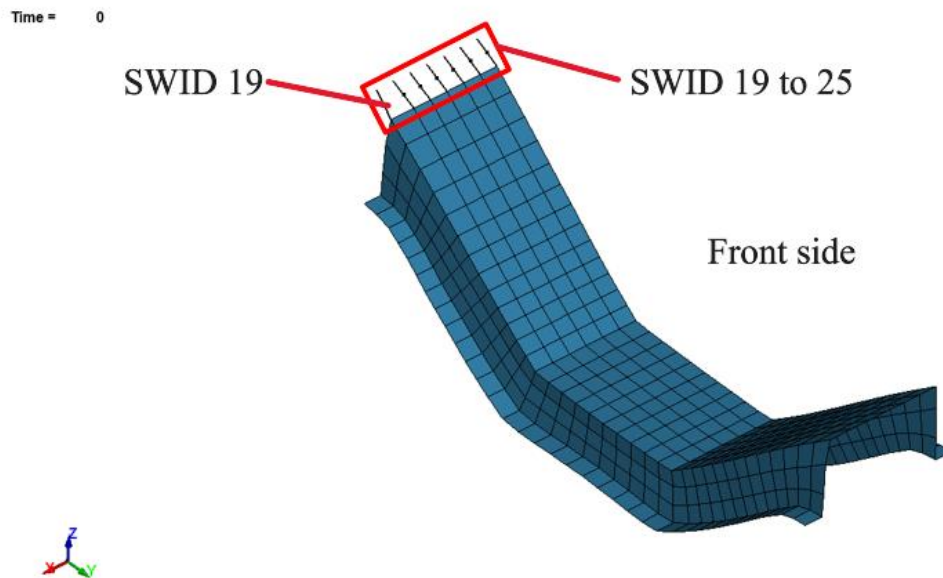


Figure 78: Studied spot welds detail, remeshed model.

The next graphs illustrate the force history in the three observed cases: non – failing (models 3 and 4, Figure 79), partial failing (model 5, Figure 80) and failing (model 6, Figure 81) spot weld constraints. Looking at the non – failing diagram, the normal force transmitted by the node is highest in the second impact. This happens because in the first impact the force is distributed between the nodes at the front vertical face of the cross member, but the impact deforms the cross beam, causing it to be more axially loaded in the second impact, while the other anterior nodes are unloaded. The shear force is almost constant in all the impact event. It is possible to see that after 150 ms the force exerted on the spot weld is reversed: the tangential component goes to zero and then raise again in magnitude, while the normal component goes to zero as well. This happens because the spotwelds register and control only normal tensile forces. Shear forces instead are evaluated in modulus. Models 5 and 6 follow the expected behaviour and follow the same history of the non – failing simulations until they fail at some point

Chapter 3: Cross member connection.

during the impact and stop transmitting any force. It is also possible to notice that there is a lag between the force exchange of the bollard with the engine and the force exchange between the cross member and the frame. That happens because of the compliance of the engine surface, the engine mounts and the cross member. The engine is rigid, hence the speed of sound (and thus the speed of force propagation) in it is theoretically infinite. As in the previous case, the shear force is the same in all the simulations but being it much higher it has much impact on the failure limit, since to fail, it is not necessary that either of the normal or shear load reach the force limit. In the model 5 case, the brake point is reached when the axial force increases in the second engine impact, while in the case of model 6, the connection is broken as soon as the shear force increases because of the first engine impact.

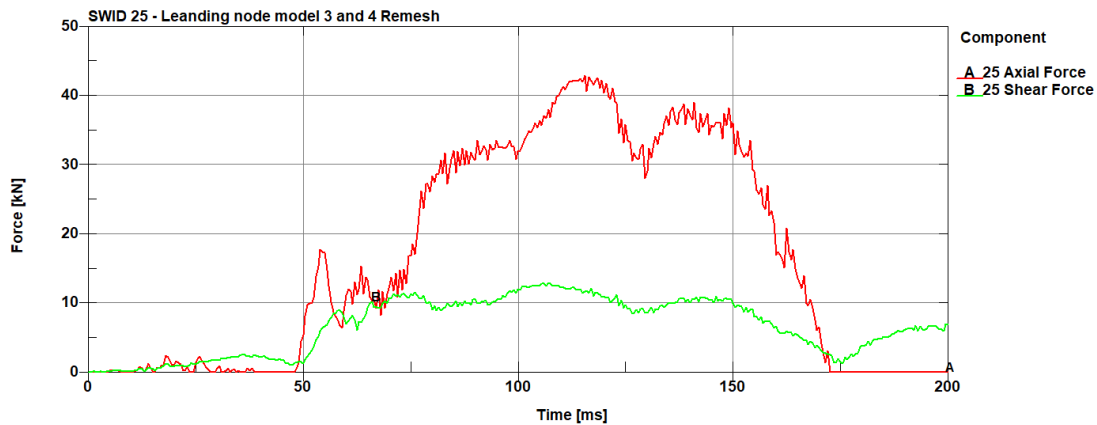


Figure 79: Leading node force exchange, remeshed models 3 and 4.

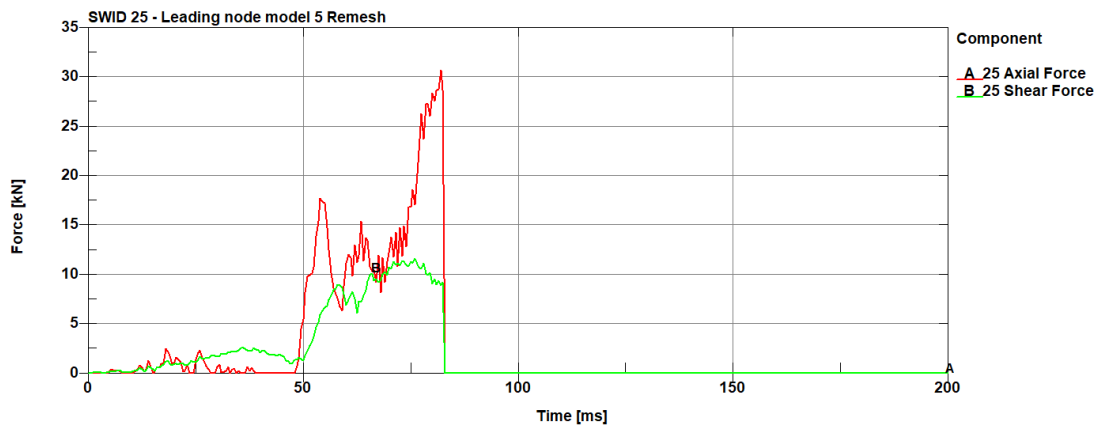


Figure 80: Leading node force exchange, remeshed model 5.

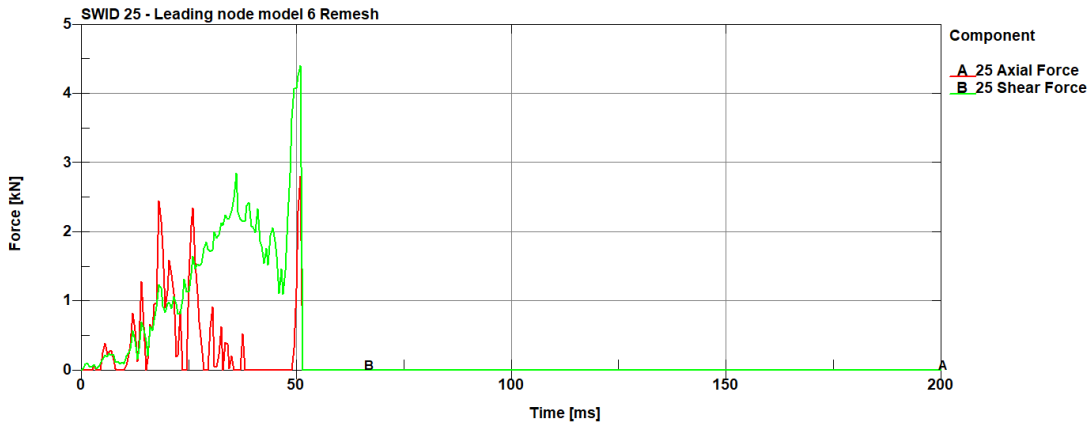


Figure 81: Leading node force exchange, remeshed model 6.

In reference to Figure 82, the central spot weld works mainly in shear, with about the same peak value of the leading node. The tensile normal force is null for most of the impact. It raises in the second part of the simulation when the flatbed moves vertically, and the vehicle leans on the bollard. In Figure 83 it is shown the case in which the previous welds have failed, and a peak of axial force is applied to the weld, which also fails. The trailing weld illustrated in Figure 84 experiences no axial tensile force at all, it failed immediately due to the shear force.

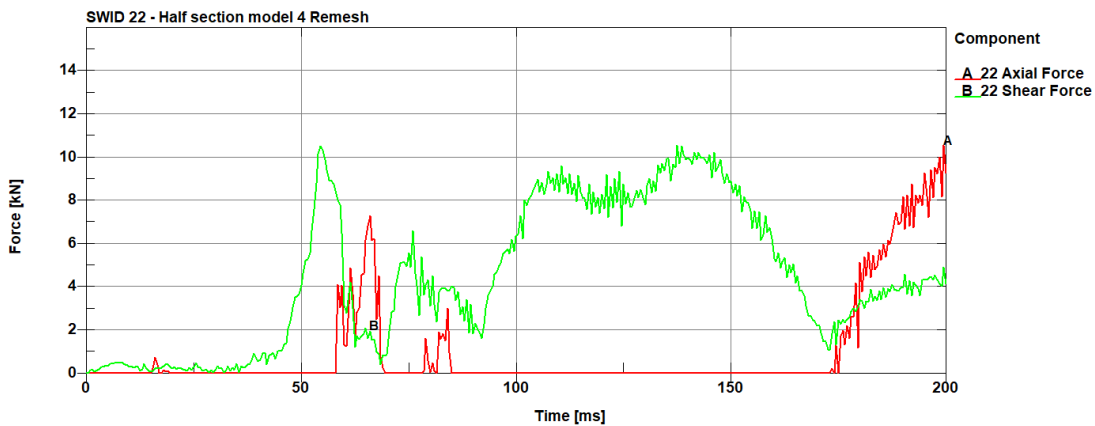


Figure 82: Half section node force exchange, remeshed models 3 and 4.

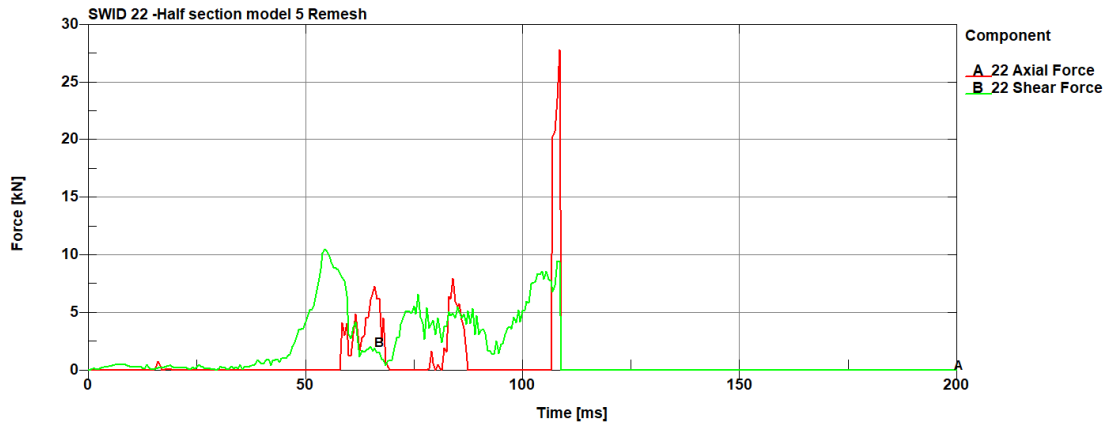


Figure 83: Half section node force exchange, remeshed model 5.

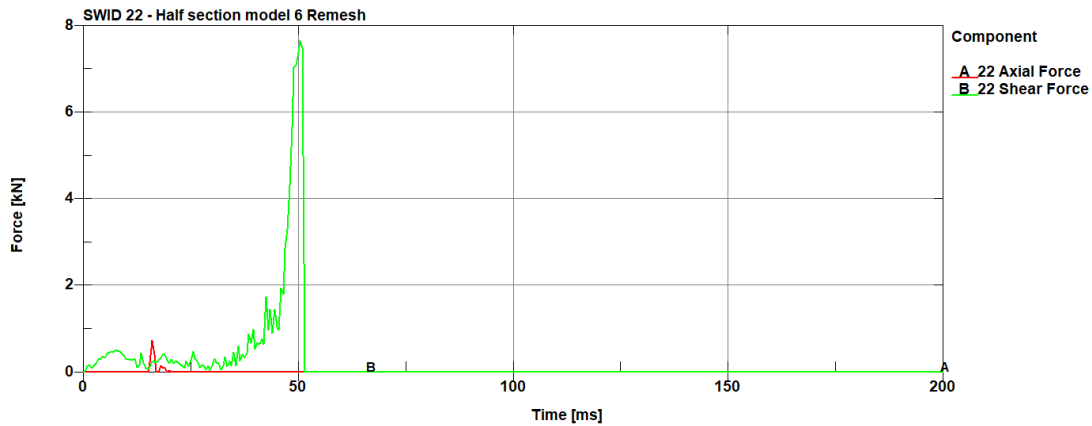


Figure 84: Half section node force exchange, remeshed model 6.

To conclude this section, we can see in Figure 85 a behaviour like SWID 22, but with much higher normal forces. The tensile load is exchanged from the central and rear nodes during the first impact, to the frontal nodes in the second impact. The load bearing is alternated between moments of tension in the front and tension in the rear of the cross member side section. Figure 86, that shows the trailing weld of model 5, confirms that during the second impact the rear of the cross member welds are in compression until the previous welds fail and thus SWID 19 must bear the engine – bollard impact forces. Also in this case, the connection fails caused by a combination of shear and normal loads. At last, Figure 87 shown as expected the weld failing immediately upon impact.

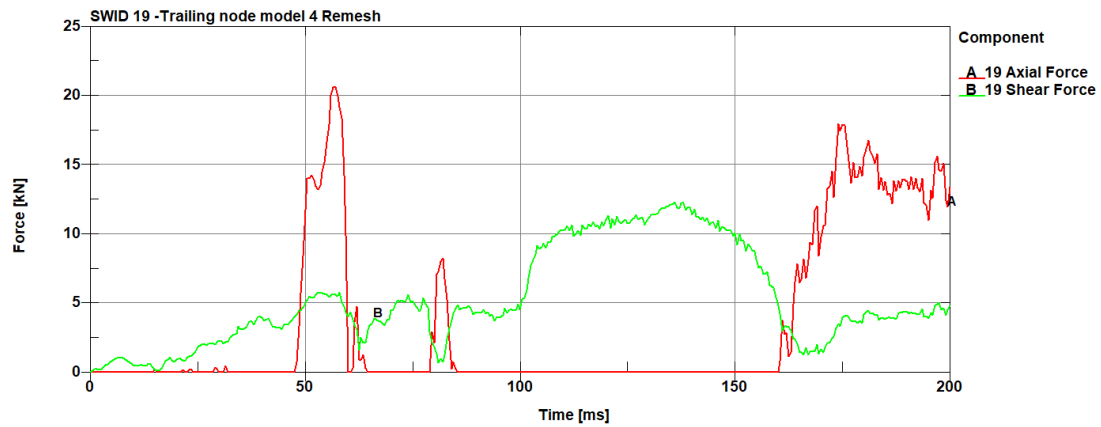


Figure 85: Trailing node force exchange, remeshed models 3 and 4.

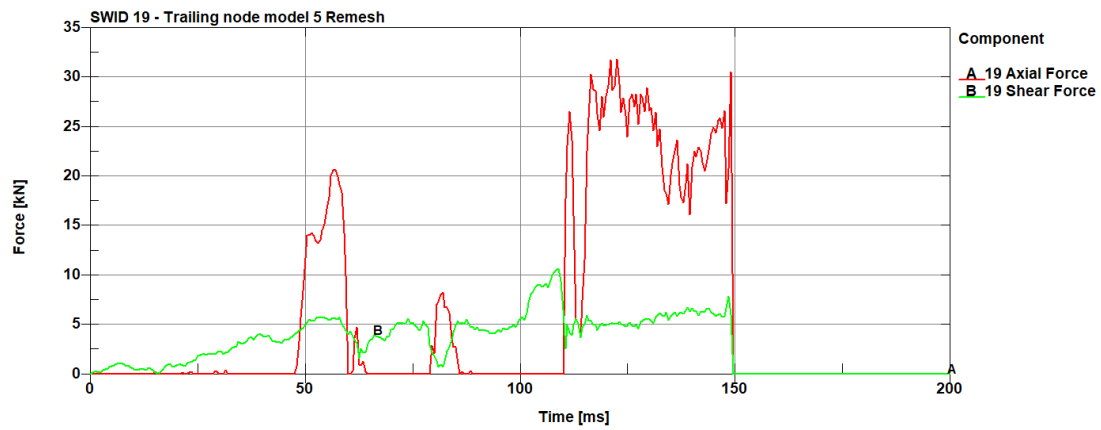


Figure 86: Trailing node force exchange, remeshed model 5.

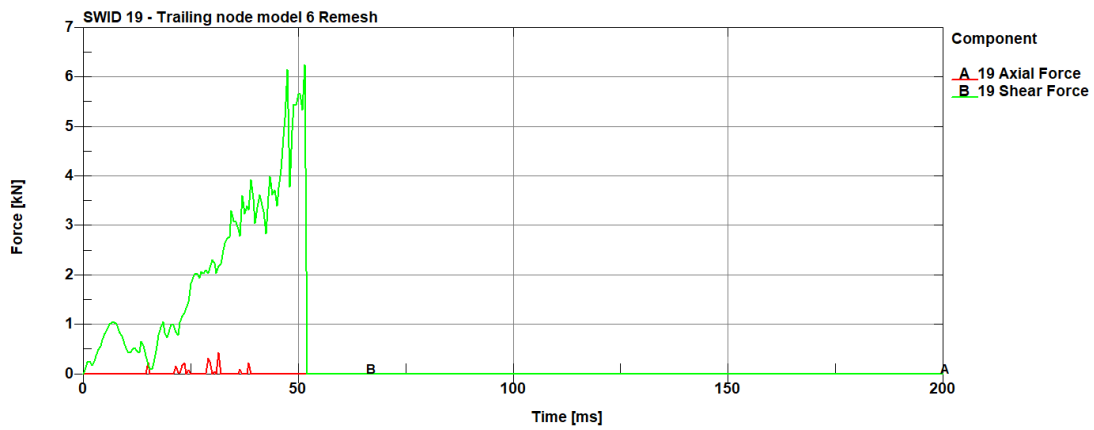


Figure 87: Half section node force exchange, remeshed model 6.

Spot weld models validation

Validation results are aligned with the findings of the previous section: in all cases the stiffness of the reference model is the most similar to the experimental results, while in all other models the bollard penetration (Figure 88) is overestimated as an effect of what previously discussed. The results of models 1 remeshed, 2 and 4 are comparable to models 2, 3 and 4 for the original mesh. Model 5 instead in the remeshed vehicle does not incur total detachment as per the reference meshing case. The deceleration of the flatbed of the examined models (Figure 89) is consistent with what is experimentally observed, except for model 6.

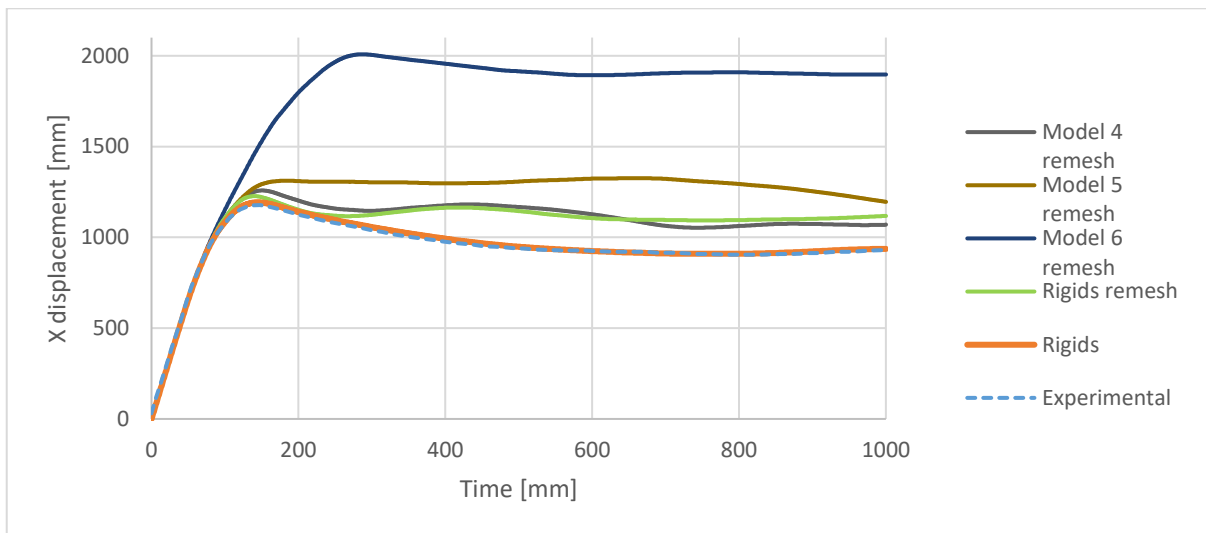


Figure 88: Bollard penetration, remeshed models.

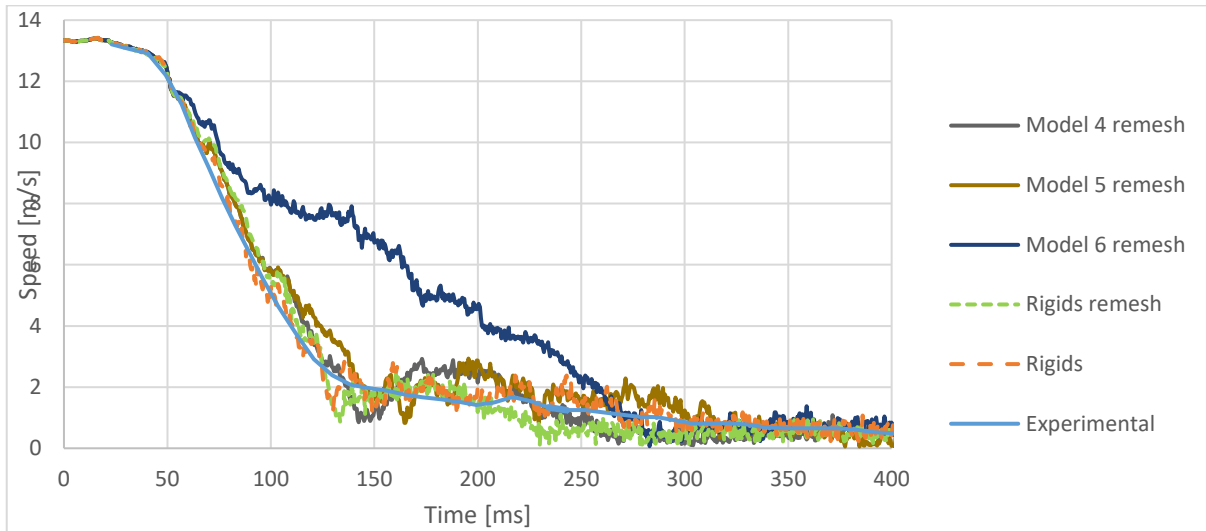


Figure 89: Flatbed deceleration, remeshed models.

The deceleration of the front vehicle reference points (Figure 90 and Figure 91) confirms that the spot weld solution follows adequately the experimental results. It can be noticed that the experimental curve is the more decelerating of all during the main impact events. Model 6 (as well as Models 5 and 6 for the original beam mesh) are outliers having lost the connectivity with two cross members and thus decelerate using the cabin floor in a much less efficient way.

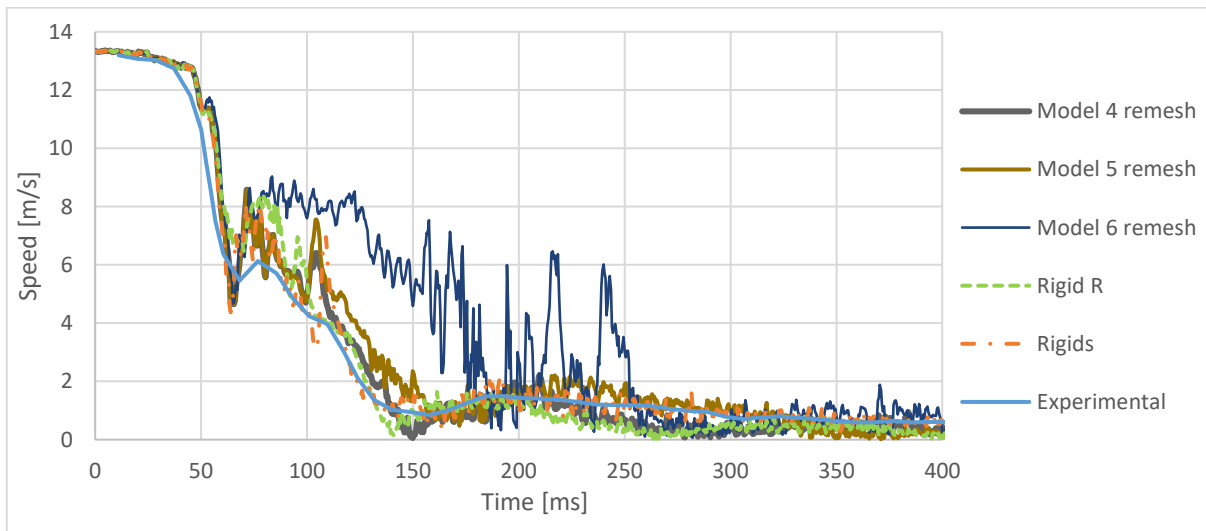


Figure 90: Cabin deceleration, remeshed models.

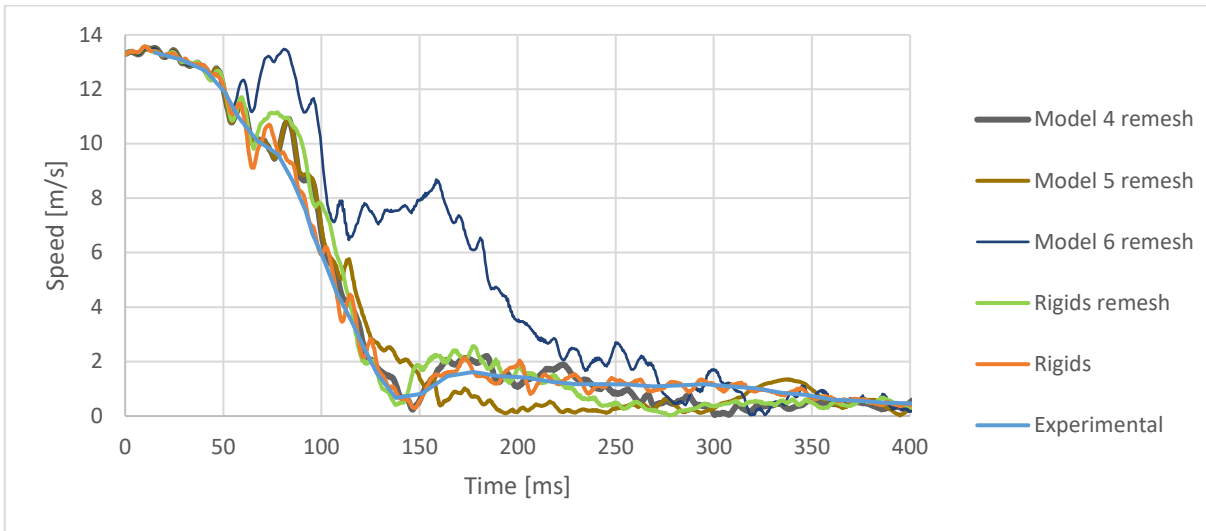


Figure 91: front wheel deceleration, remeshed models.

The analysis of the vertical motion of the flatbed (Figure 92) shows high consistency in the results, with model 4 reaching the highest point. It is interesting to notice how the two rigid models reach the same height of the experimental model but the suspension travel (the negative portion of the plot between 600 and 1000 milliseconds) is higher.

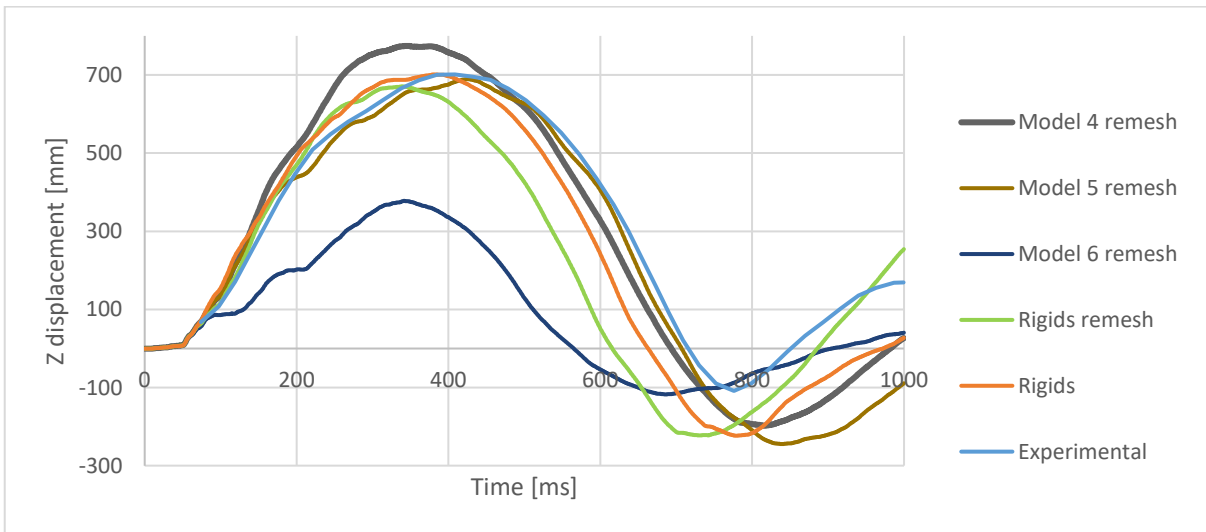


Figure 92: Flatbed z displacement, remeshed models.

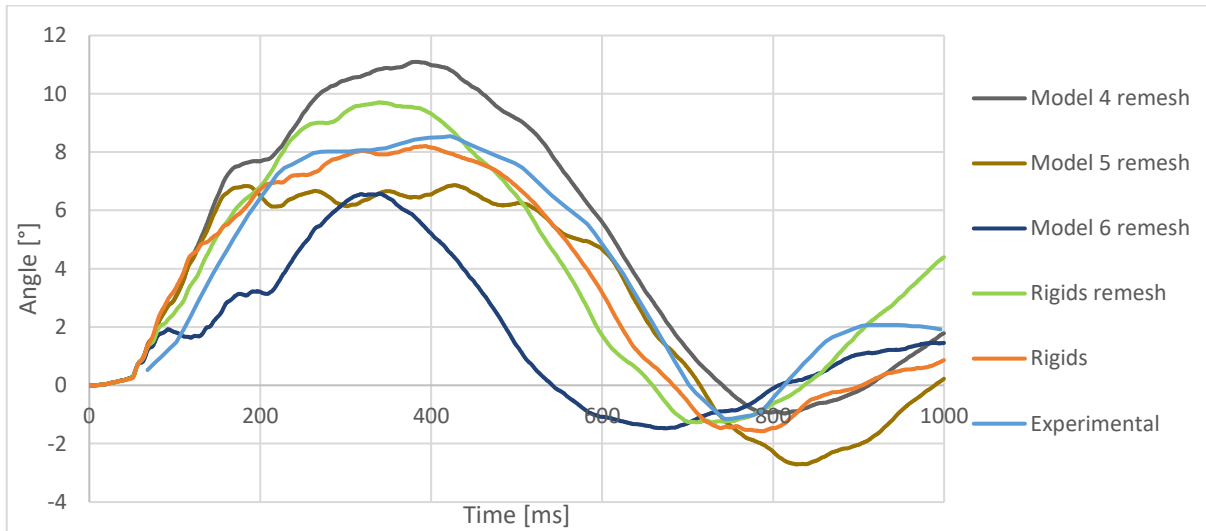


Figure 93: flatbed pitch, remeshed models.

Shear force effect.

To understand completely the parameters involved in the spot weld constraint, the effect of the other involved parameters can be now observed. As reference to what has been stated in the previous section, the shear force is somewhat constant in value with a peak of 10 kN. This information can be used to find lower values of SS that can cause failure. Table 6 summarizes the simulations performed in this section.

Model number	Normal limit force	Shear limit force
1	Rigid connection	
2	70 kN	50 kN
7	70 kN	20 kN
8	70 kN	15 kN

Table 6: Cross member connection simulation summary, shear and strain effect

The simulated x force history of the reduced shear force limit model, in Figure 94, has the same footprint of the remeshed spot welds models. In these cases, the response is slightly more compliant (with a less intense first force peak) than the reference model 1, but it is, however, very close. Both models incur spot welds failures during the second force peak. Interestingly, even If the functioning spot welds at the

simulation end is very limited with only two working spotwelds in model 8, The response is very similar to the non-failing spotwelds models.

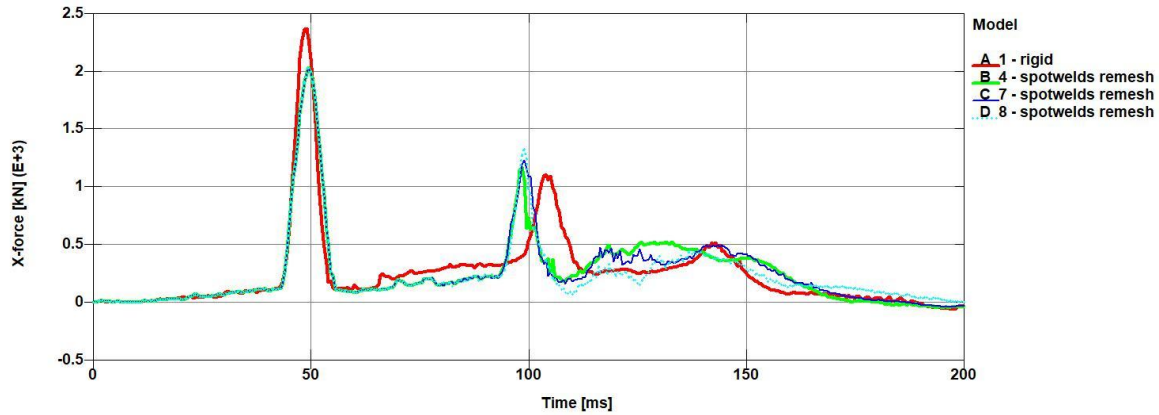


Figure 94: X-force, remeshed model, shear force sensitivity analysis.

With reference to Figure 95, Figure 96 and Figure 97 the impact evolution of the limited shear force models as previously stated, follows the same evolution of model 4. However, as opposed to the normal force induced spotwelds failures, that happen in close proximity of force peaks and thus very close among them in time, Being the shear force more homogeneous in time, the spot welds failures are progressive, and the welds can efficiently share the force burden, keeping the structure relatively intact even with few welds remaining.

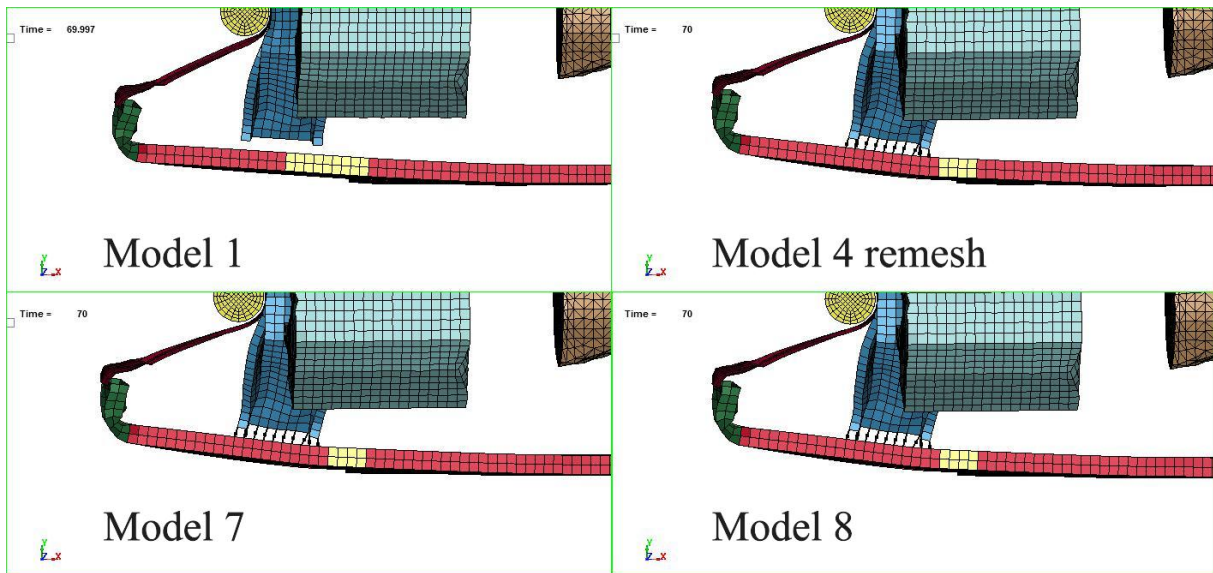


Figure 95: Spotweld shear resistance sensitivity analysis, 70 ms simulation time, remeshed model

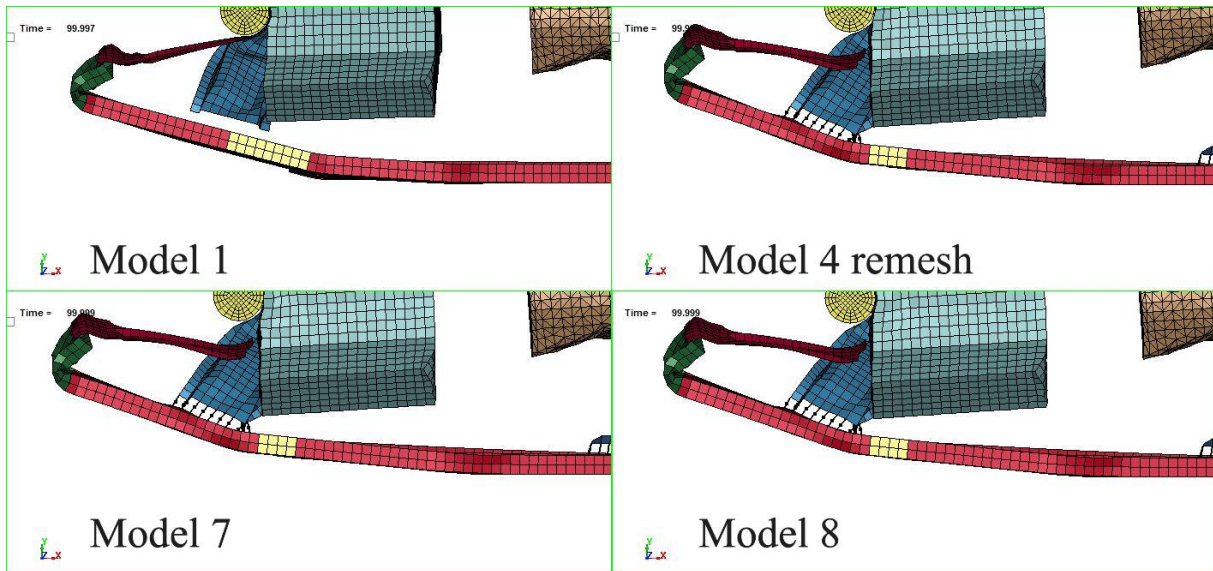


Figure 96: Spotweld shear resistance sensitivity analysis, 100 ms simulation time, remeshed model

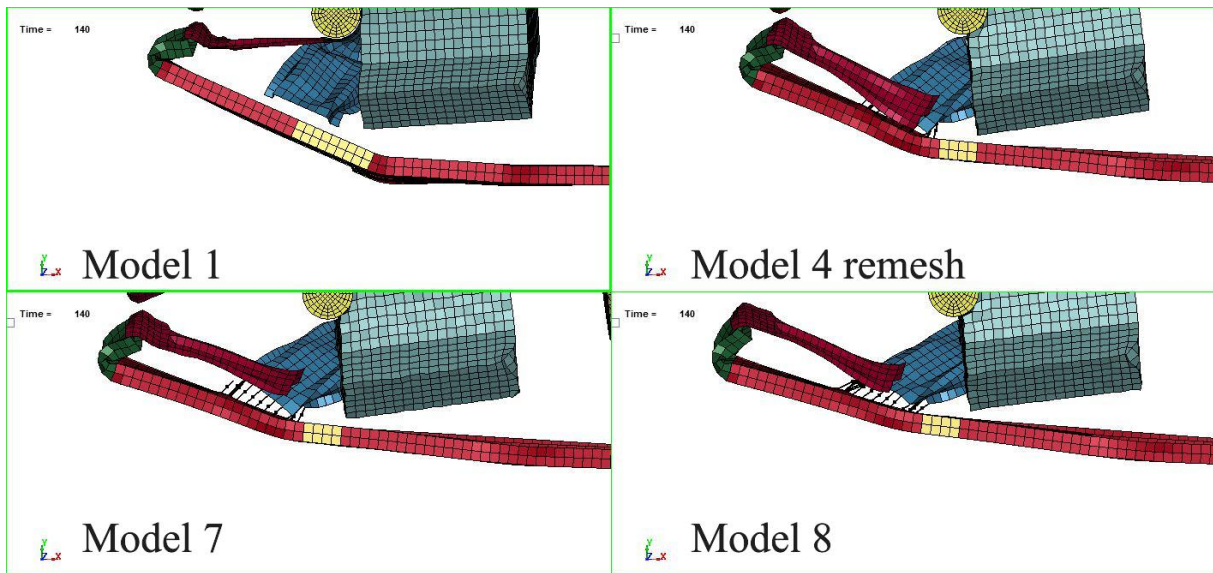


Figure 97: Spotweld shear resistance sensitivity analysis, 140 ms simulation time, remeshed model

Looking at Figure 98, there are no appreciable differences between model 4 remesh and model 7. Model 8 is slightly less warped, but this is confirmation that the significant deformation of this part cannot be reduced only acting on the connection with the frame, to ensure a bollard penetration comparable to the experimental results.

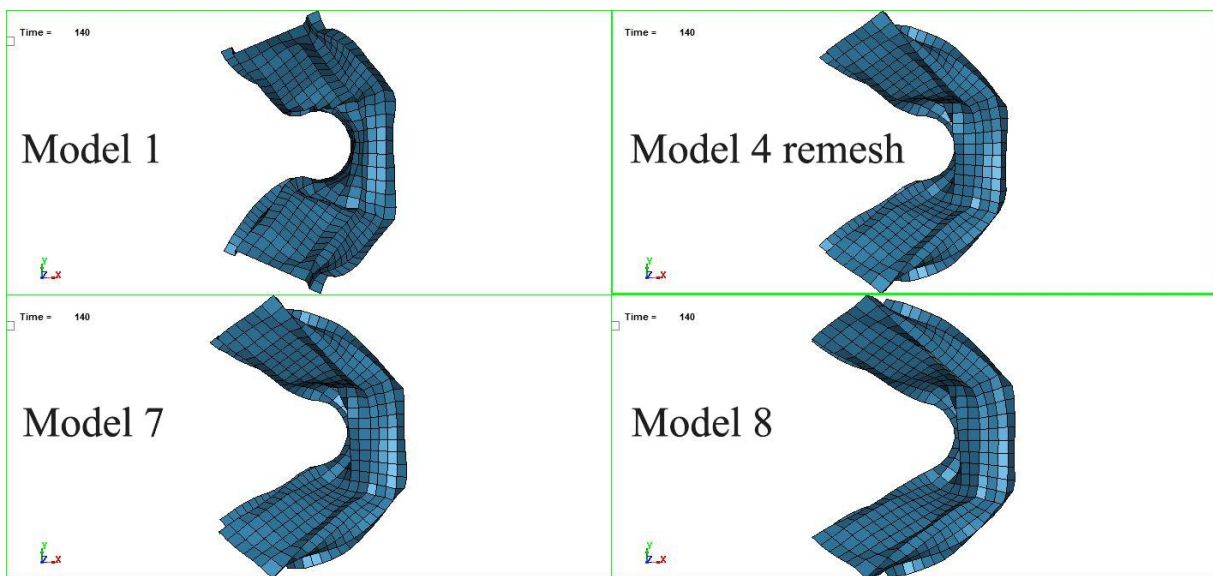


Figure 98: Cross member deformation, shear force limit contribution.

Spotwelds forces – Shear force limit

Models 7 and 8 are derived from model 4 remesh, and thus the SWIDs under close observation are the same for the remeshed models. Figure 99 shows how the change of shear force limit changes substantially the failing order of the welds. Now that the shear force is so limiting, as long as the shear load is low, the axial force can be transmitted, but if there are shear load acting on the weld simultaneously, the resistance to axial peaks is severely hindered. In Figure 100, model 7 behaves similarly to the previous ones, with the welds failing in rapid succession as the forces is accumulated on the leading working node. Instead, in model 8, it is possible to see that the difference in failure mode gives time to the mesh to adapt and limits the sudden axial peaks occurrence. Figure 101 shows how the spot welds of model 8 hold almost all the way through the simulation. Welds on the trailing vertical cross beam edge do not incur failure at all. In model 7 instead, the load inversion from compressive to tensile is observed as in the previous non-failing model cases.

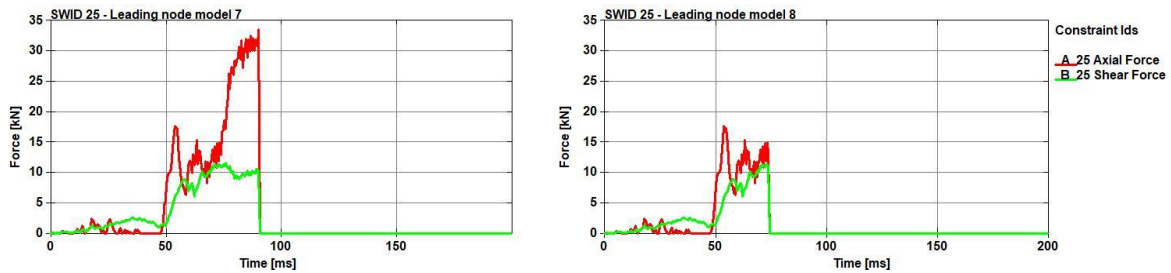


Figure 99: Leading node force exchange, remeshed models 7 and 8.

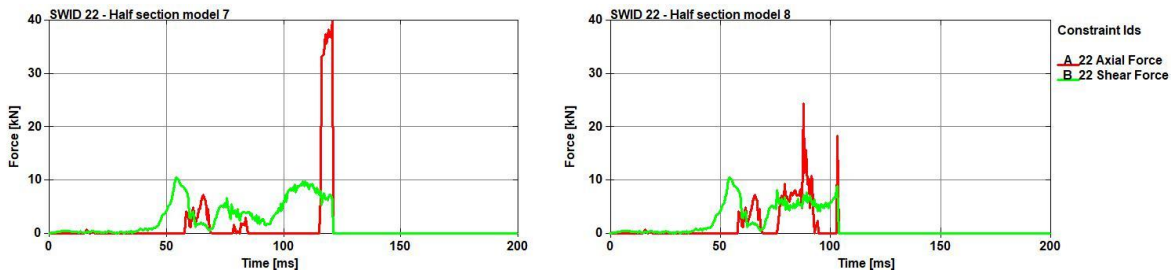


Figure 100: half section force exchange, remeshed models 7 and 8.

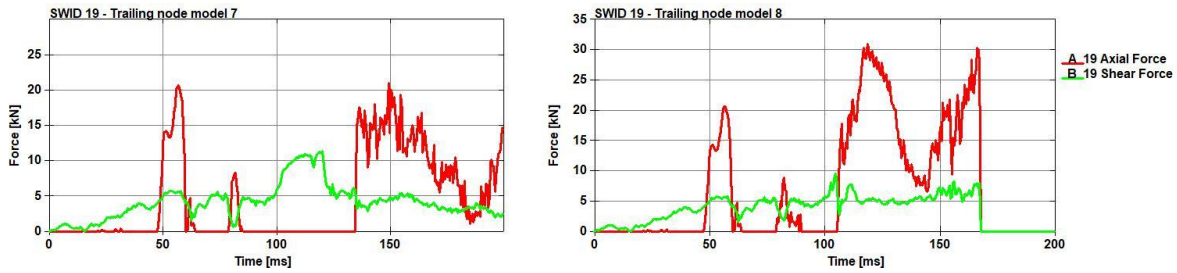


Figure 101: Trailing node force exchange, remeshed models 7 and 8.

Spot weld models validation

The previously made observations hold for the limited shear force resistance model. The gradual loss of frame integrity caused by the connection failures increase the bollard penetration in the engine bay.

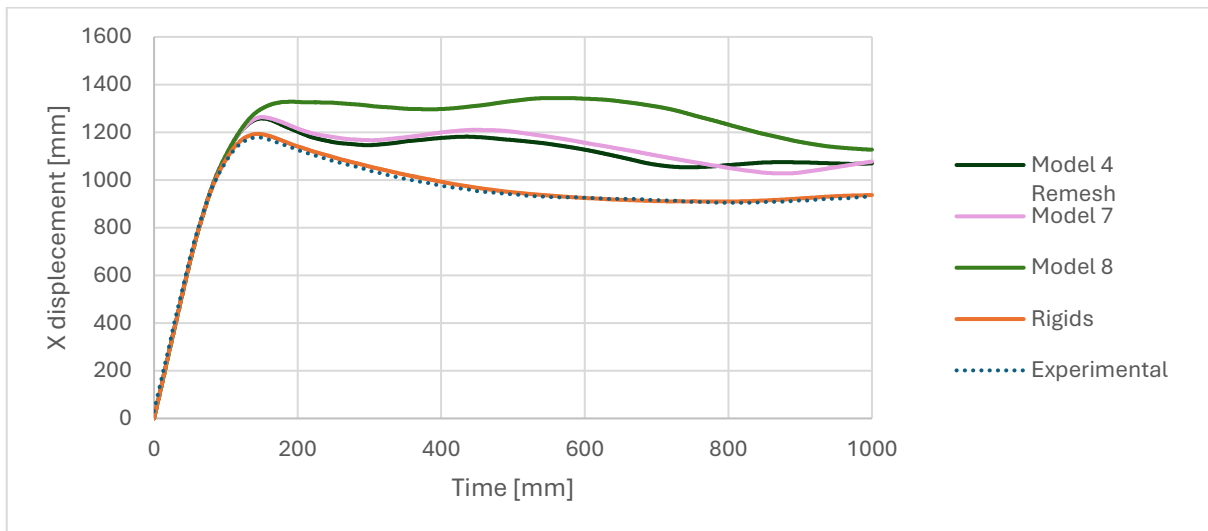


Figure 102: Bollard penetration, shear effect.

As opposed to the bollard penetration, decelerations of the reference points in the body are extremely consistent with the experimental results and between each other, as it is possible to see in Figure 103, Figure 104 and Figure 105.

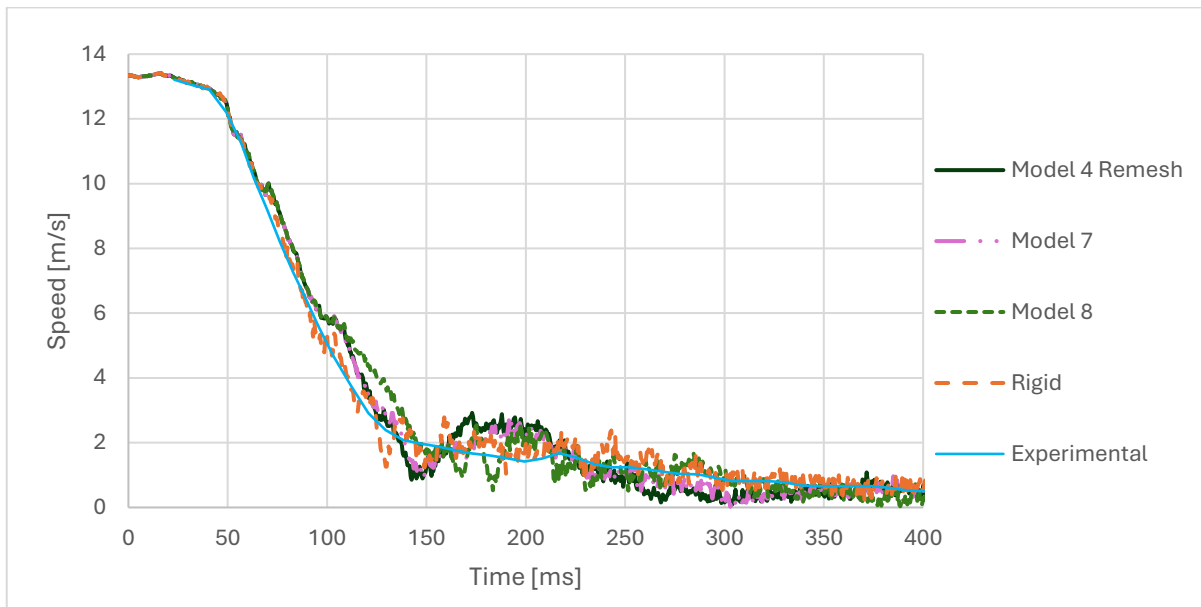


Figure 103: Flatbed deceleration, shear effect.

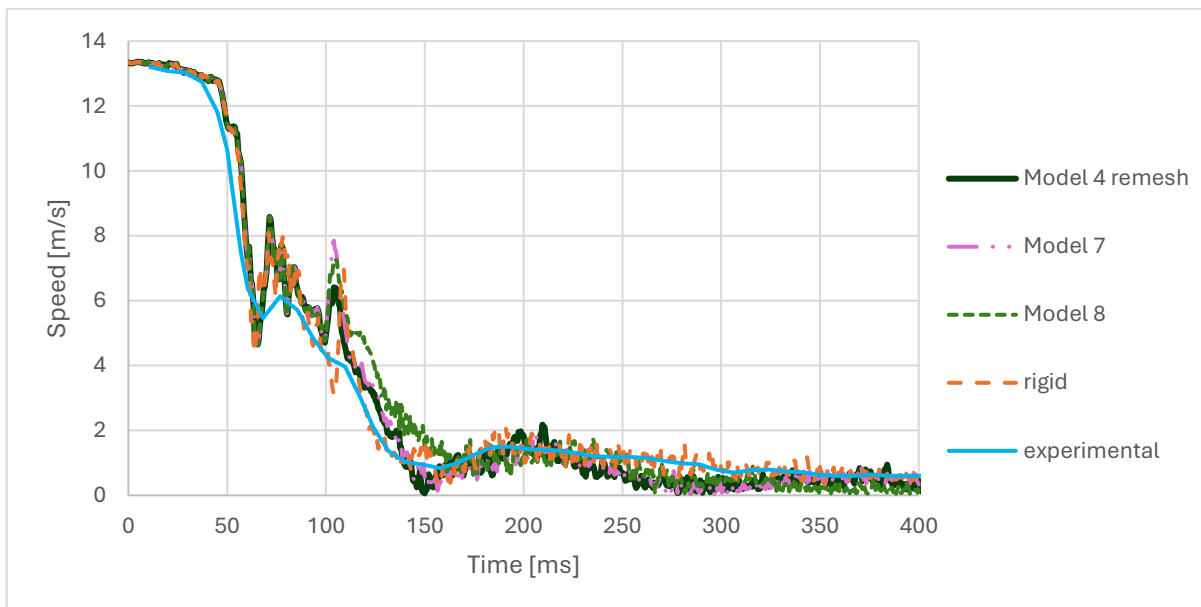


Figure 104: Cabin deceleration, shear effect

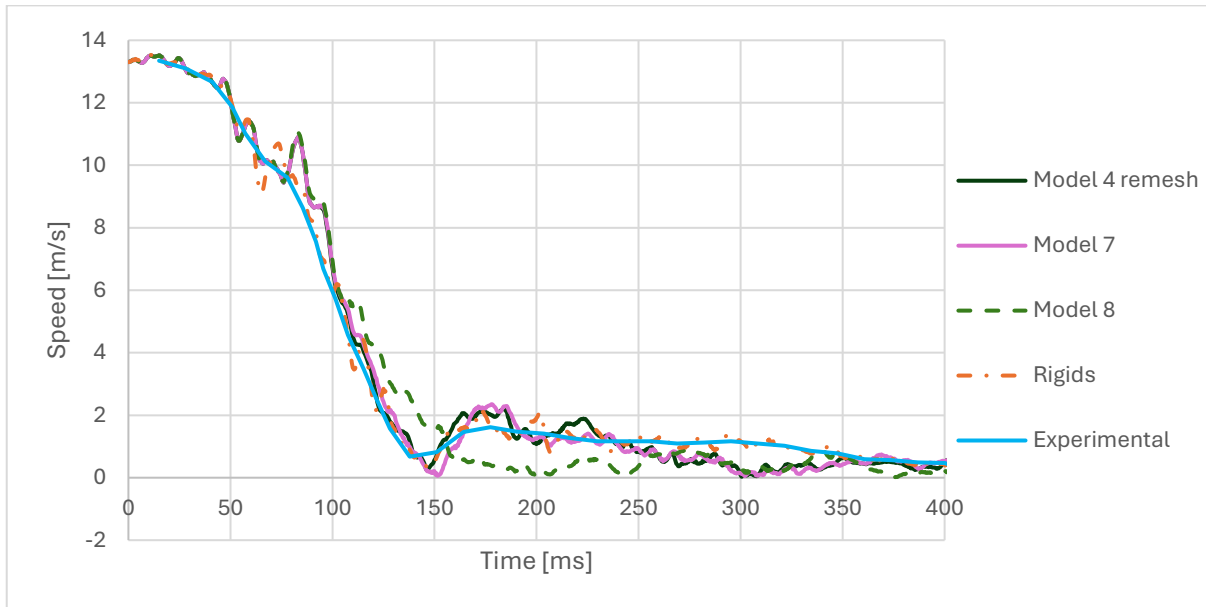


Figure 105: front wheel deceleration, shear effect.

The vertical motion of the flatbed is also consistent with the experimental results (Figure 106). However, the pitch is always more intense (Figure 107). This means that in the simulated model, the front of the vehicle is at a lower z with respect to the experimental results, increasing the pitching motion (Figure 108). This could also be attributed to the more compliant suspensions that make the front of the flatbed move downwards in the first part of the impact events.

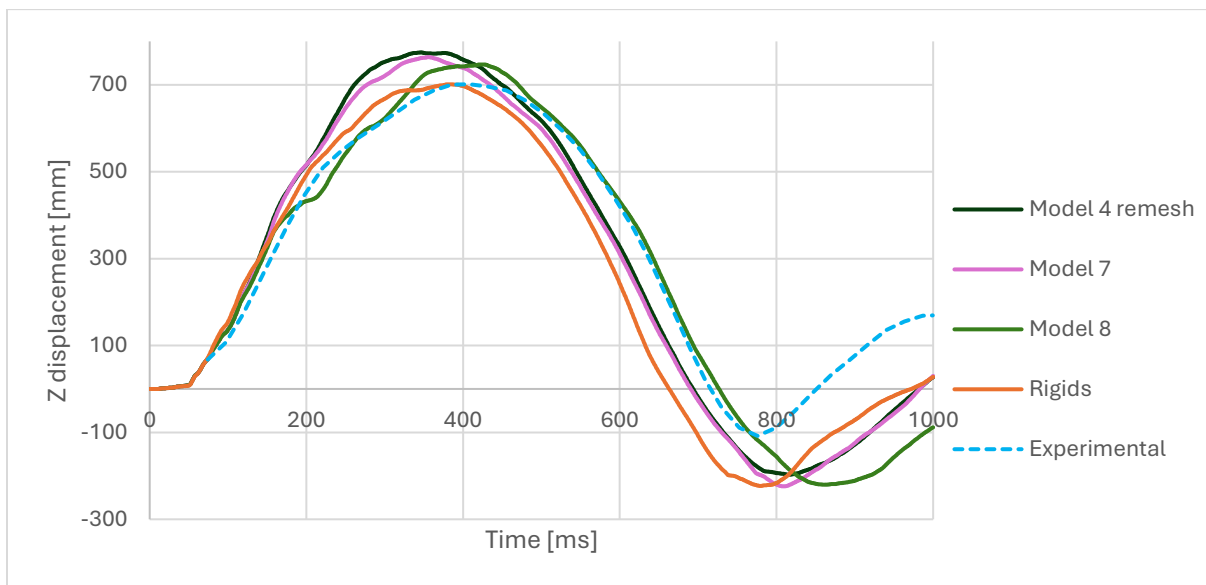


Figure 106 Flatbed z displacement, remeshed models.

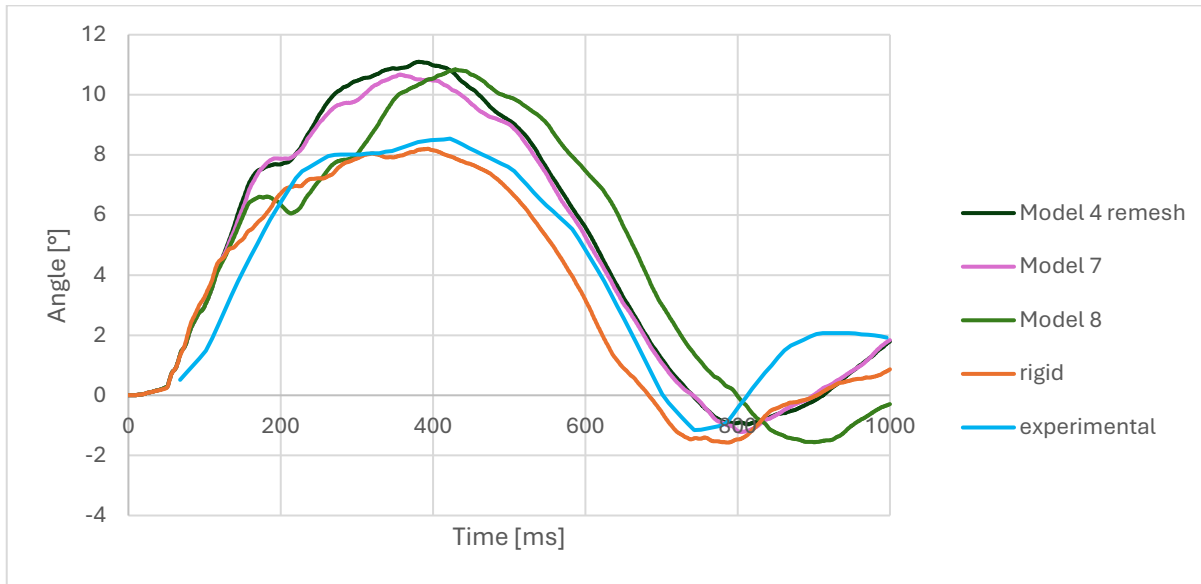


Figure 107: flatbed pitch, remeshed models.

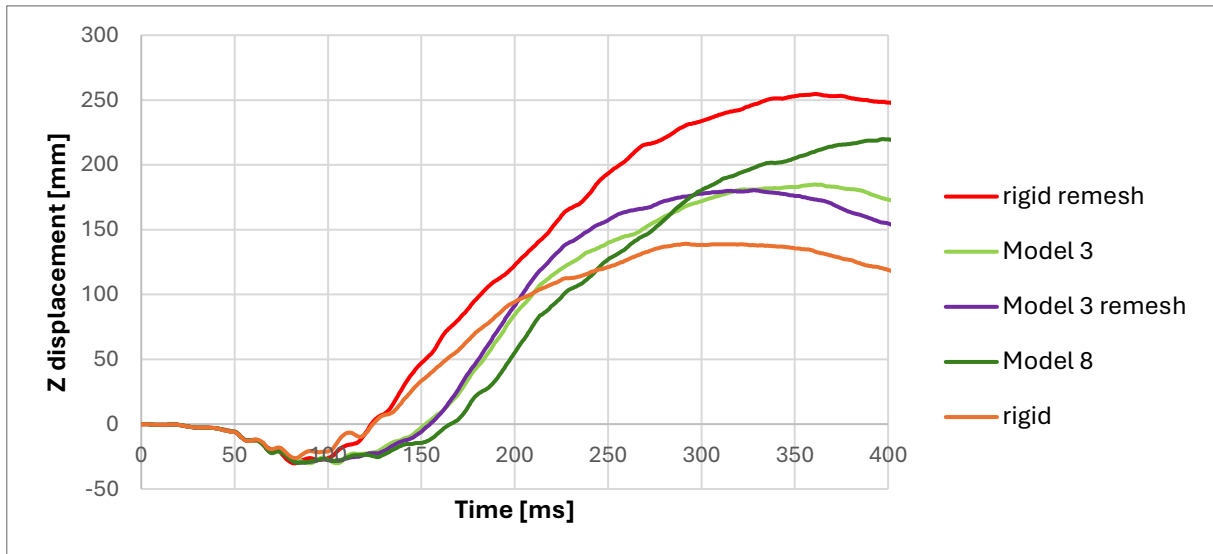


Figure 108: Front flatbed vertical motion.

Conclusions

This study leads to the conclusion that to obtain less cross member deformations during the simulation, altering the resistance of the connections do not significantly alter the deformation of the cross member unless the structural integrity of the whole frame is compromised, due to the separation of the cross member. In this case however, the results are diverging from what experimentally observed.

The experimental data show higher stiffness of the vehicle because for the duration of 100 milliseconds of main impact events (between 40 and 140 milliseconds) the lower value among the presented curves is the experimental curve. In future studies, this could be obtained by increasing the cross section of the engine mounts, longitudinal beams or cross member. Or increasing the material properties of the steel varieties modelled in this vehicle.

In all flatbed motion plots, the compression of the simulated suspensions, always exceeds the experimentally measured one. If it is considered that the vertical displacement and the pitch of the flatbed is similar in all non – failing connection simulated models and given that the vehicle mass is the same between the N1 model and the experimental test vehicle mass, this suggests that the suspensions are set as more compliant than the experimental vehicle ones. A stiffer suspension system could also result in a stiffer impact response, a reduced pitching motion and thus more accurate results

Chapter 4: Impulse conservation analysis

During the previous tests with the N1 and N2 generic vehicle models, a discrepancy in the momentum calculation has been noticed: the x momentum curve does not correspond between the output from LS-Dyna and the integral of the force exchanged between the bollard and the vehicle (impulse), which usually generates significantly lower result values. This phenomenon is addressed in this study as impulse loss.

The vehicle momentum is obtained by adding the momentum histories of all the moving parts, since the momentum is found in the matsum database. The force instead is obtained directly in the rforc database.

Vehicle X momentum: $P(t) = \sum_1^n P_i(t)$ with n being the vehicle part number.

$$\text{Impulse from force exchange: } P(t) = P_0 + \int_0^{t_{end}} F_x dt$$

$$\text{N1 model} \quad P_0 = -4.77 * 10^4 \text{ kg} * \text{m/s}$$

$$\text{N2 model} \quad P_0 = -9,56 * 10^4 \text{ kg} * \text{m/s}$$

The force signal moreover has been filtered with a SAE class 60 filter and integrated in time to evaluate the impulse, which corresponds to the change of momentum between colliding objects. This problem is observed with various degrees of severity in both models N1 and N2. The goal of this section is to understand the reason behind such discrepancies with data analysis and investigation of the various simulations.

The analysis is carried out starting from the N1 vehicle, looking at the momentum loss in different scenarios where the bollard hits the vehicle in a different position: $y = 0$ (centred bollard) and $y = 500$ mm (longitudinal beam centred bollard) from the centre of the vehicle, as showed in Figure 109. Subsequently, also the N2 vehicle impact case with centred bollard is taken into consideration.

Although the N1 centred bollard model does not display momentum loss, observing its force and momentum histories help to understand how they differ from the beam centred bollard case.

N1 model

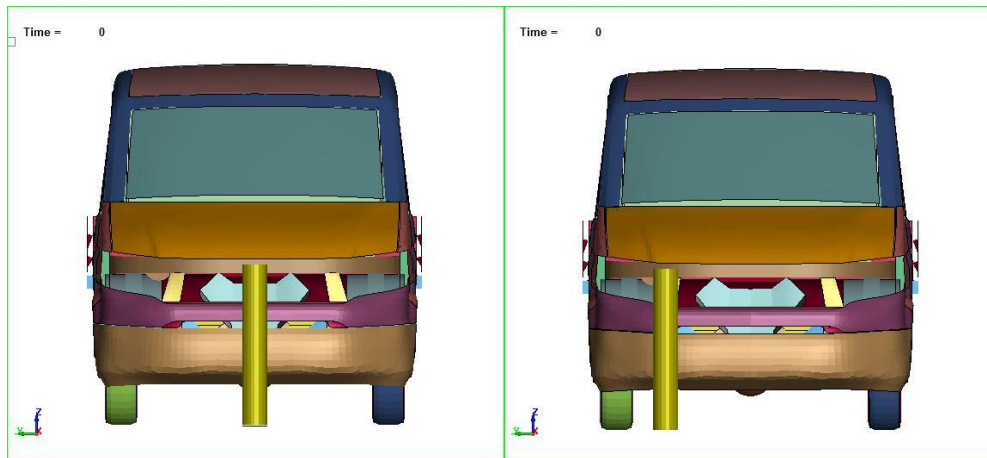


Figure 109: N1 vehicle models, different impact locations.

In Figure 110 it is possible to notice that the filtering chips away portions of the force peaks. It has been theorized how this phenomenon could be the reason behind the lower value of the integrated force in some of the models. However, this is not the case as will be illustrated in Figure 112.

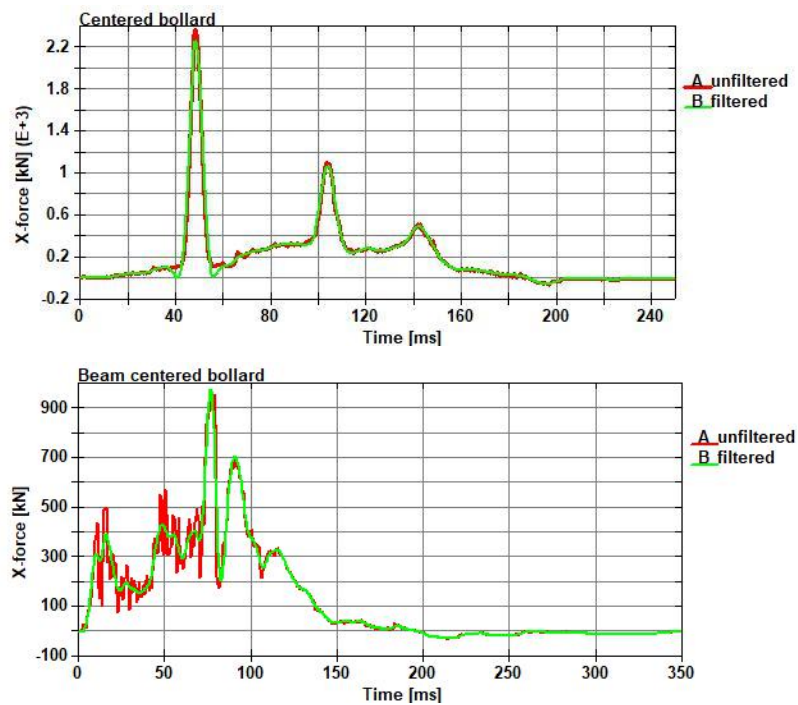


Figure 110: Force history, filtered and unfiltered curves.

To quantify the filtering effect on the momentum loss, the two curves have been integrated and then the filtered curve is subtracted from the unfiltered one. This new parameter has been defined as integrated difference, and it is shown in Figure 111. It is possible to observe that at the difference's average is close to zero, but during the impact events peaks are generated, due to the filter effect on the rapid force oscillations. The value of the integrated difference during the rest of the simulation fluctuates always within an amplitude of less than 10 kN*ms. This amount is negligible with respect to the observable phenomenon of impulse loss, and thus it cannot be the leading cause of impulse loss.

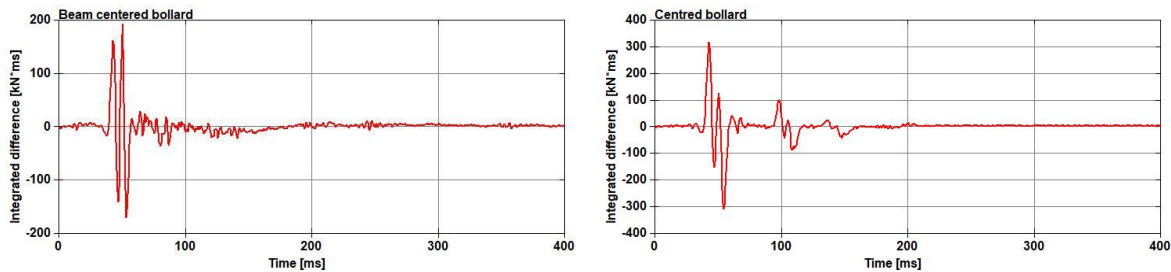


Figure 111: Integrated difference, centred bollard and beam centred bollard.

For what the momentum diagrams are concerned, in Figure 112 it is possible to see that there are no appreciable differences between all the curves for the centred bollard, while for the beam centred model, there is a noticeable divergence from 400 ms onwards. It is important to notice that in that time span, the momentum curve changes while the impulse from the force exchange with the bollard remains constant. This behaviour is due to the motion of the rear vehicle that pivots around the bollard z axis. When the wheels touch the ground after the air phase, the tires friction with the ground stops the vehicle from spinning and thus, the difference in forward momentum is provided by a different contact surface: the tires-ground contact. Through this surface, the momentum of the vehicle is impacted without the need for touching the bollard. It is more correct to observe the z moment rather than the x force because the vehicle rotation is also dependent on y direction forces. Figure 113 shows how from 400 ms a torque is applied to the vehicle, which corresponds to the rear tires landing on the ground and further slowing the vehicle spin. The applied torque, however, keeps pushing the vehicle back, causing the momentum to be slightly positive. This happens because the elastic energy stored in the tires and suspension is released when the vehicle has lost all its negative x direction inertia. At the end of the simulation, the same contact cancels the movement in the positive x direction after the vehicle springs back. The sequence of events is showed in Figure 114

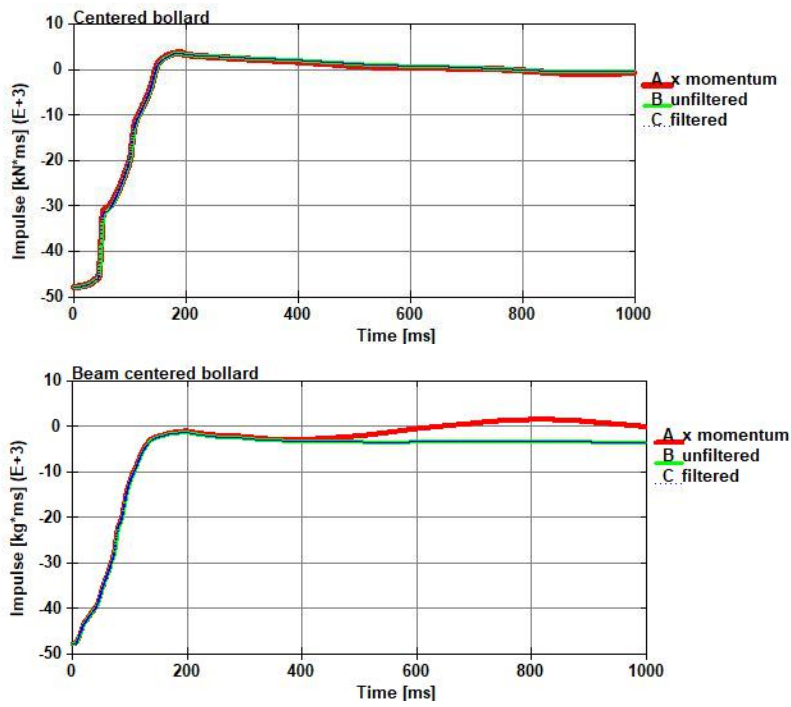


Figure 112: Decentred bollard N1 impact, X force and momentum.

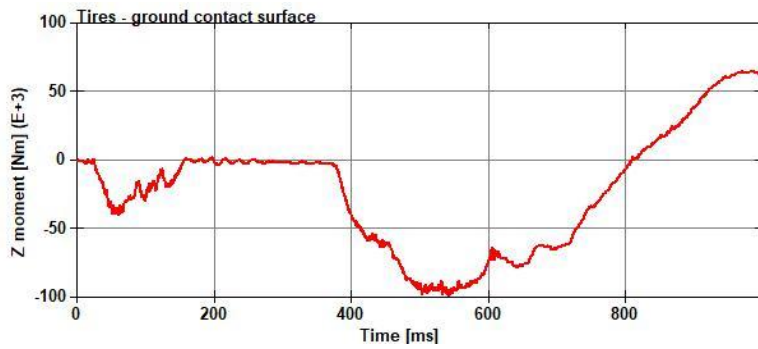


Figure 113: Moment transmitted from the ground to stop the vehicle movement.

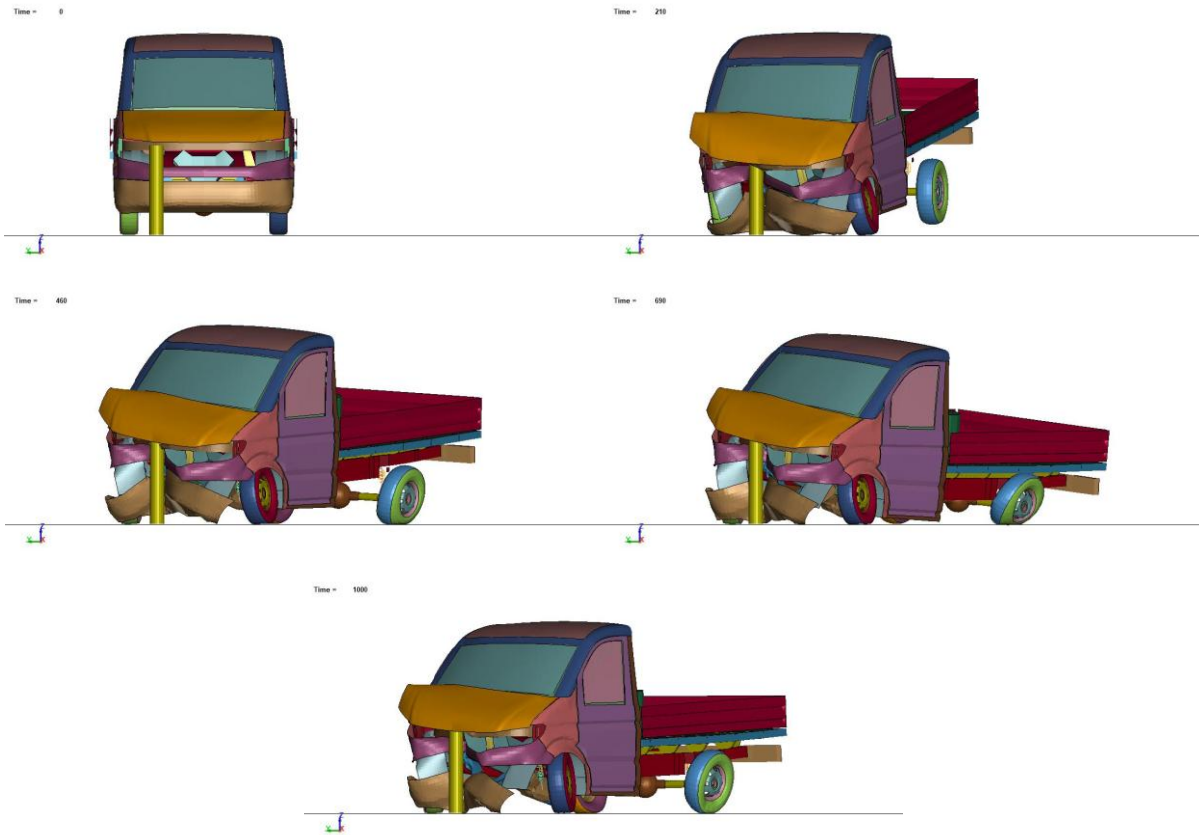


Figure 114: N1 vehicle beam centered bollard, interaction with the ground.

N2 model

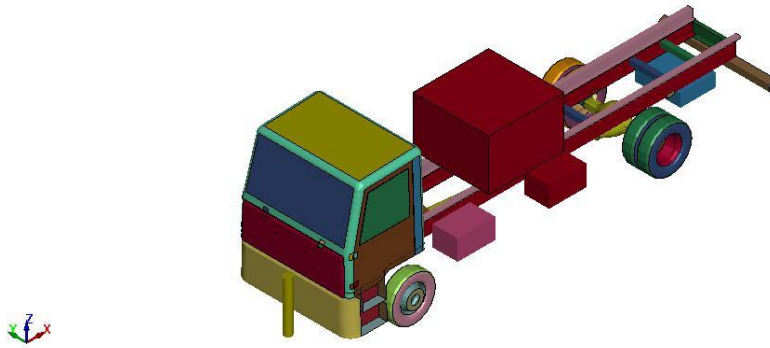


Figure 115: N2 generic vehicle model, centred bollard

The same approach has been used in the N2 model vehicle case. As opposed to the N1 vehicle, the N2 models displays significantly less impulse than the momentum recorded by LS-Dyna even in the centred bollard impact case. As previously done, Figure 116 displays the force exchange used in the calculation of the impulse. Also in this case, the difference between the filtered and unfiltered signals is modest.

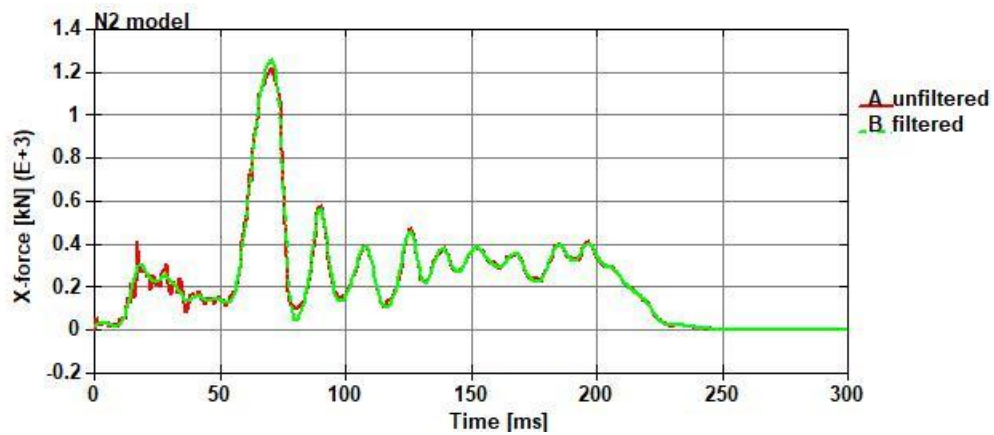


Figure 116: N2 model x force exchange with the bollard.

However, in this case, The Surface to surface contact is not sufficient to describe the whole interaction between the vehicle and the bollard: the N2 generic vehicle models contains structural beam elements that interact with the bollard, namely the stabilizer and the steering rod. These mono dimensional parts cannot generate contact segments, as needed for the contact formulation SOFT2, which is used for shell and solid elements [8]. Hence, an additional contact algorithm is used to account for the beams, which is AUTOMATIC_NODES_TO_SURFACE. The force exchange stored in the rforce database is shown in Figure 117. The mentioned beams are displayed in Figure 118.

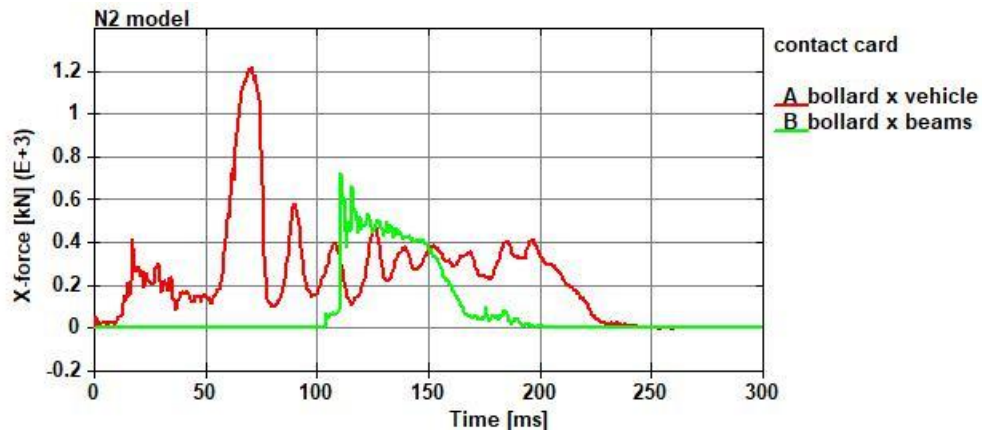


Figure 117: Force exchange in the Surface to surface and nodes to surface cards.

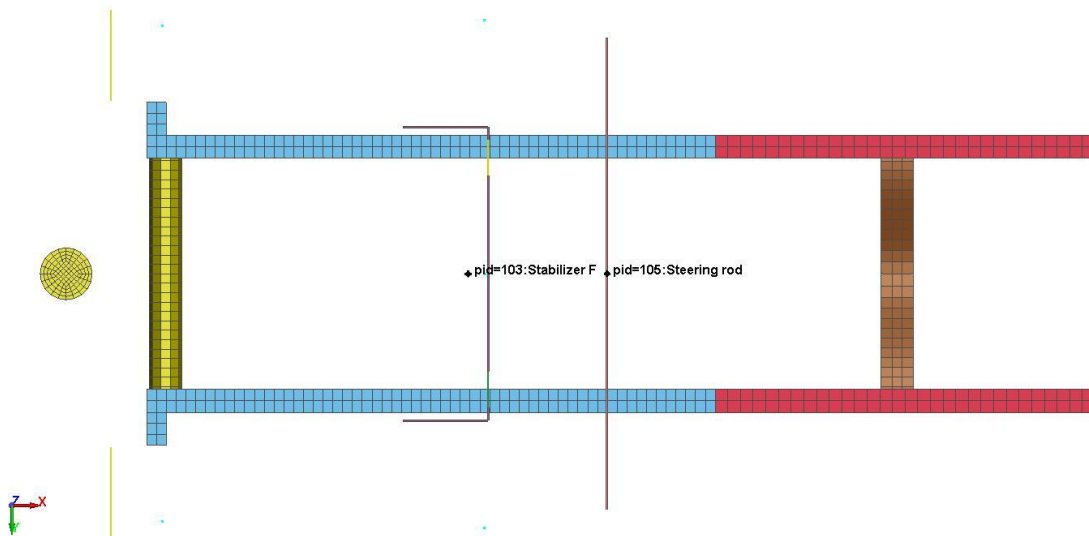


Figure 118: Beam element in contact with the bollard.

The results of the abovementioned forces and the resultant x momentum are displayed in Figure 119.

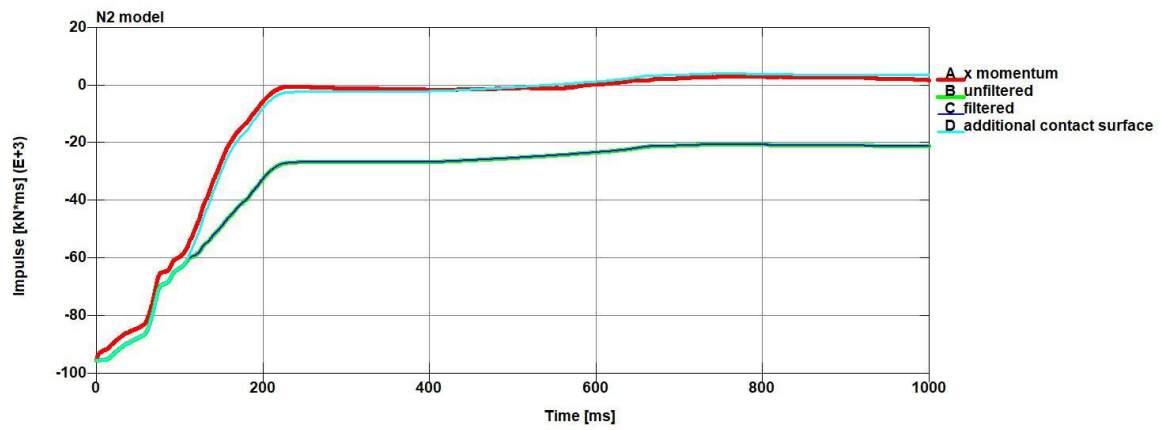


Figure 119: N2 model impulse and momentum results.

It is possible to notice that also in this case the effect of the filtering on the force history has negligible effect on the impulse. The addition of the beams contact card contribution makes the final impulse value match with the final x momentum.

Conclusions

In chapter 1 the new Q4γ formulation has been compared to the element formulations 2 (Belytschko-Tsay) and 16 (fully integrated) used in LS-Dyna. The two element formulations have been tested on simplified models with different mesh sizes with max element size of 40 mm and 20 mm. The comparison of these simulation results with the ones obtained in EPX show that, for representing shell elements in high deformation scenarios, EPX formulations converge faster than LS-Dyna ones. While the previous Q4γ formulation was comparable with LS-Dyna's EL16, the new version outperforms the alternatives, showing fast convergence in these simple tests.

The model setup is made in such a way that the frame can absorb little energy, but its inertia is used to deform the cross member around the deformable bollard. This allows to observe the shell elements in the cross member to reach satisfactory deformation even if the model is not realistic.

In chapter 2 the reference model impacts against the bollard at increasing initial speeds. The different scenarios have been investigated, and it has been noted that the complexity of the model makes difficult to predict at any given velocity, how the energy will be distributed among the engine bay parts. In general, the engine surface, the cross member under engine, the longitudinal beams and the cabin floor are the most involved parts in the energy exchange.

The first peak is due to the engine inertia, that after the first collision completely dissipated and the engine usually springs back from the bollard in the positive x direction. Then, the interactions between the cross member, bollard, engine and the cabin floor shape the subsequent peaks. Increasing the initial velocity, and thus the kinetic energy to dissipate, more parts fail, as is the case of the driveshaft for $V_i = 70$ km/h and the cabin floor at $V_i = 80$ km/h.

It emerged in this chapter how the model has limitations in dealing with higher energy impacts because the automatic contact algorithm is not equipped to deal with the erosion of contact segments, and in the studied cases many elements from engine surface, frame front bumper and bumper fail, thus causing interpenetration between the involved parts. This in turns deteriorates the simulation accuracy because the engine mesh gets stuck in the bollard and cannot bounce back from it as could otherwise. Moreover, the interpenetration causes negative contact energy which is an alarming indicator of simulation instability.

In chapter 3, the hypothesis that the extensive cross member deformation could be mitigated by using connections with the frame that allow for failure has been discussed. This theory has been tested with a sensitivity analysis on the force limits of spotwelds elements. At first, the connection has been applied without any modification to the mesh, but this led to an unrealistic backwards orientation of the spotwelds. Although not realistic, this gave the opportunity to test the axial resistance limits on the spotwelds. This, in turn revealed that when using links having breaking criteria, three cases can be obtained: 1-no spotweld is broken, 2-only a portion of the spotwelds break, or 3-all of them cease to function eventually. The first case generates always identical results in all simulations with the same boundary conditions, the third case generated unsatisfactory results because the bollard was able to penetrate with limited obstruction into the engine bay and thus the cabin, in opposition to what has been measured in an experiment crashing a real N1 vehicle.

The second case instead is dependent on the amount of spotweld failures, and gave the opportunity to observe how the forces that link the cross member and the frame are influenced by the spotwelds failure. The axial force peaks cause the foremost spotwelds to fail, and this concentrated the forces on the subsequent spotweld, generating many peaks in rapid succession that break the welds.

Then, an adjustment of the mesh has been proposed to accommodate better positioned spot welds. In this case, also a model with adjusted mesh but without spotwelds has been tested to understand the effects of each factor. The following considerations can be done:

- Rigid connections via external node set are stiffer than the spotwelds connection, meaning that the force raises faster in the main impact.
- The smaller is the force peak, the lesser will be the engine spring back and thus the second impact will happen earlier.
- The experimental results are more aligned with the reference rigid connection model with respect to the spotweld models.
- The kinetic energy at the end of the main impact remains at 100kJ or more in the remeshed model. This is not a realistic behaviour, and it is dependent on the kinetic energy of nodes that are removed from the simulation (eroded kinetic energy). Moreover, high hourglass is observed in the energy balance. Hourglass energy is dangerous because it pulls energy away from the system, potentially altering the simulation outcome. This problem can be easily solved switching the element formulation to EL2 to EL16, at least for the most hourglass – susceptible parts.

-
- The spotwelds are loaded alternatively with tensile and compressive forces

A last batch of simulations has been studied to understand the effect of a reduced shear force limit. The shear force is more homogeneous during the impacts event, as opposed to the normal force high peaks. This leads to the fact that spotwelds do not fail due to normal force peaks unless the weld was already under shear load. This mechanism causes the welds to fail gradually as opposed as the non-mesh-adjusted models.

In any case, only acting on the connection resistance, either the cross member will be extremely deformed or completely detached, causing severe bollard penetration. This does not mean that the connection with failure criteria is not applicable at all, but to obtain simultaneously no cross member detachment and limited cross member deformation, some other complementary solution to increase vehicle stiffness must be implemented. Some solutions could be increasing the section of the cross beam, longitudinal beam and / or the engine mounts, or improve the material properties of the steel used in the model.

In chapter 4, the theory of the filter reducing the impulse of the force exchange with the bollard was proven to be incorrect, directly comparing the filtered and unfiltered force integrals. The result was a negligible difference between the two. The phenomenon was observable in models with non-obvious active contact surfaces, such as the wheel-ground friction in model 1 – beam centred bollard, or the beams-bollard surface in model N2.

Acknowledgements

This work closes the part of my life as a student, and what a part it has been. All the people I met, the group projects we have done, the lectures we followed, and the coffee breaks we took, the challenges we encountered and the solutions we found shaped me as a person and, inevitably, set a trajectory for my future. I will cherish those moments, including the hardships, when there will be other people, other brakes, other challenges, later in my life.

But before then I want to thank all of the people that have been near me, either physically or figuratively, during all these years of study. First and foremost, I want to thank my family, for the unconditional and unrelenting love and support, for believing in me and for encouraging me when I needed it most.

I want to thank my closest friends. Companions of adventures, the people that make the days bright and the nights long. To Andrea, Beatrice, Francesca, Francesco, Oscar and William, thanks for being with me in this journey.

Thank you to my girlfriend and her family, whom I feel now as mine as well, for your hospitality and your friendliness.

Thank you to the friends I found along the way, the colourful souls that made me enjoy my time here in Turin. To the university colleagues, to the formidable teammates of Squadra Corse, to the kind devils from the Sala d'Arme del Folle, to the uncountable TTG groups that became good friends, thank you.

I want to thank especially Prof. Scattina for the endless patience, his support and the opportunities that he offered me.

Thank you to Dr. Damijan Markovich for the kindness and the enthusiasm he showed me and for giving me the possibility to be a part of this project.

Bibliography

- [1] <https://counterterrorism.ec.europa.eu/hvm/generic-vehicle-models.php>
- [2] https://counterterrorism.ec.europa.eu/assets/docfiles/europlexus_manual.pdf
- [3] LIVERMORE SOFTWARE TECHNOLOGY (LST), LS-Dyna manual theory R12, Ansys, 2020
- [4] <https://www.dynasupport.com/howtos/element/shell-formulations>
- [5] Simone Saraceno, Development of simplified vehicle models for impact to barrier, MSc in automotive engineering, April 2023, Politecnico di Torino, Alessandro Scattina
- [6] <https://counterterrorism.ec.europa.eu/hvm/generic-vehicle-models>
- [7] Grigorios Theodoridis, Development of simplified vehicle models for barrier impact, MSc in automotive engineering, December 2022, Politecnico di Torino, Alessandro Scattina
- [8] LIVERMORE SOFTWARE TECHNOLOGY (LST), LS-Dyna keyword manual R12, Ansys, 2022
- [9] <https://www.dynasupport.com/howtos/general/contact-energy>
- [10] Avalle, Massimiliano; Belingardi, Giovanni, Resistenza statica e dinamica di punti di saldatura in differenti condizioni di sollecitazione, Intervento presentato al convegno XXXII Convegno Nazionale AIAS tenutosi a Fisciano, Salerno nel 3-6 settembre 2003.54

